Mapping and modelling of landslide and flood hazards on St. Eustatius with openLISEM

Master thesis

by Lotte Ciska de Vugt

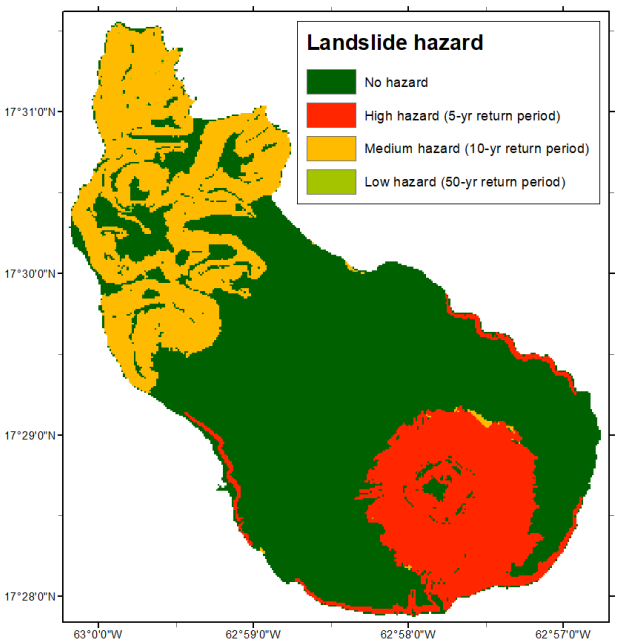

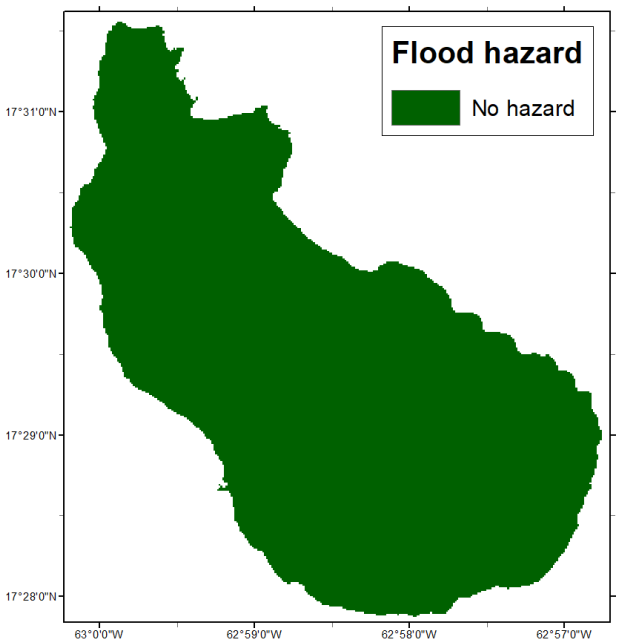

UTRECHT UNIVERSITY

MASTER'S DEGREE THESIS

Mapping and modelling of landslide and flood hazards on St. Eustatius with openLISEM

Author:

Lotte Ciska de Vugt

Student ID: 4021177

Supervisors:

Prof. dr. Steven de Jong

dr. Menno Straatsma

Thesis submitted in partial fulfilment

of the requirements for the degree of

Master of Science in Earth Surface and Water

09 November 2018

Abstract

Between 1900-2016 there have globally been more than 14,000 major events of natural hazards, like landslides and floods. The Caribbean is, partly due to the high abundance of islands, one of the most vulnerable areas of the world to natural hazards. The area experiences many different types of hazards with a high frequency of occurrence. When dealing with multiple hazards, it is important to notice that they are connected to each other. The research in the multi-hazard subfield is, however, still scarce and there are only a few real multi-hazard models.

St. Eustatius is an island in the Caribbean that experiences many different hazards. The information on the occurrences of these hazards is, however, very little, especially regarding landslides and floods. This study, therefore, investigated the historical occurrences of the landslide and flood hazards on St. Eustatius and their magnitudes for different return periods. This was achieved by constructing a hazard inventory and modelling the hazards with the deterministic model openLISEM. A new version of openLISEM has added the capability of modelling slope stability and debris flow simultaneously with the already available hydrological model.

The hazard inventory was constructed using field observations of historic landslide deposits. The flood hazard was not included in the inventory since it was too difficult to recognize historical flood events in the field. The data needed for the model input was constructed from available datasets and with the analysis of both field measurements and taken soil samples. After all the model input was constructed a sensitivity analysis was performed. This sensitivity analysis showed that the new openLISEM model is most sensitive to changes in the cohesion, internal friction angle, soil depth and initial soil moisture content.

After a qualitative calibration of the model with the constructed landslide inventory, the model was used with four model scenarios of design storms with a return period of 1-year, 5-years, 10-years and 50-years. The results of these model runs show that the slopes of the Quill volcano and the coasts of the island have the highest landslide hazard. The model results also indicate that there is no flood hazard on the island.

The model results were validated qualitatively with the constructed hazard inventory. A quantitative assessment could not be made since the landslide database was not detailed enough to perform this assessment. The assessment showed that it is highly likely that the slope failure and debris flow components of the model overestimate the intensity of the landslide hazard. However, the spatial occurrence of the slope failure events does coincide with the location of previous landslide events.

The predicted flood hazard could not be validated since there was no flood hazard inventory. The discrepancy between reality and the model results is partly due to problems within the model itself and partly due to the input data (meteorological data, DEM, geotechnical soil data and hydrological soil data) that was given to the model.

The results of this study should thus be interpreted with care. The new component of the openLISEM model still has some issues and is not suited, at the moment, to provide a detailed or accurate prediction of the hazards that occur on the island. For future research, it is important that a better hazard inventory of all the occurring hazards is constructed first. After this, a better DEM, more detailed data on soil characteristics of the island and a more suited model will also contribute to a better prediction of the hazards occurring on the island.

Acknowledgements

I would like to thank my first supervisor prof. dr. Steven de Jong who gave me the opportunity to do this MSc research project about hazard risk assessment. He provided me with insightful comments and suggestions for the research process and the structure of this thesis. I would also like to thank dr. Menno Straatsma who took time from his schedule to be my second supervisor. A special word of thanks goes to Bastian van den Bout. He helped me tremendously with understanding the used model and always had time to answer my questions.

This project would not have been possible without the people from TNO. I would like to thank them for giving me the opportunity to work within their research project of St. Eustatius and for funding my fieldwork on the island. I also thank the Department of Physical Geography at Utrecht University who funded my research as well.

My grateful thanks are extended to dr. Johan Stapel and the people from CNSI who provided me with a room in their research centre and helped me out during the sample analysis in their lab. I should also thank Clarisse Buma and the people from STENAPA for helping me around on the island and Walter Hellebrand from the Historical Foundation of St. Eustatius who provided me with insightful information about the history of the island.

My sincere gratitude goes to the staff of the sedimentary lab at the Vrije Universiteit in Amsterdam and Tim Winkels who helped me with the sample analysis in their lab and provided me with insightful knowledge on the used techniques.

Lastly, I would like to thank my family, Paul, Ellen and Adri, and my partner Mark van Dort, who took the time to proofread my earlier drafts and supported me during this research project and my entire study. Thank you.

Contents

List of figures

List of tables

Chapter 1 Introduction

Globally, there have been more than 14,000 major events of natural hazards between 1900-2016, according to the Emergency Events Database (EM-DAT) (CRED, 2017). In 2016 alone, there were 342 natural disasters reported, causing 8,733 deaths, affecting 569.4 million people and causing USD 154 billion in damages (Guha-Sapir et al., 2017). Developing countries are especially vulnerable to natural hazards and see the highest number of affected people (CRED, 2017). This is often due to the low budget that is available for mitigation and research (Alcántara-Ayala, 2002).

One of those areas is the Caribbean. According to Stoltman et al. (2007), this is one of the world's most disaster-prone areas. The area is prone to volcanic activity, earthquakes, landslides and tropical storms. The Caribbean is not only characterized by many different types of hazards, but also by a high frequency of these hazards. The area is on average struck by over 100 tropical storms in a year, of which 6 develop into a hurricane (Bender, 1991). Besides being a developing area, the abundance of (smaller) islands also makes the Caribbean very vulnerable to hazards. Due to their isolation, islands can have very limited possibilities of leaving or coming in. This means both evacuation of the population and incoming help after a disaster faces many difficulties. A good example is a recent disaster on Sint Maarten caused by hurricane Irma (2017). During the first couple of days, it was very difficult for help to arrive on the island, as the airport was cut off and the harbour was partly destroyed (Westerink, 2017). On smaller islands, this becomes even more difficult when the only harbour or airport has been destroyed during the disaster.

When dealing with multiple hazards, it is important to acknowledge that they are connected to each other. A good example is a landslide creating a dam in a river, causing upstream flooding and possibly downstream flooding when the dam failure occurs (Ruiz-Villanueva et al., 2017). Landslides in the Caribbean are often caused by hurricanes or tropical storms bringing high-intensity precipitation events (DeGraff et al., 1989). A less obvious example is the recorded cases of hurricanes triggering earthquakes (Bryant, 2005). When assessing risk or hazard in an area it is thus important to understand the relationships between all the occurring hazards in the area. If this is not acknowledged, the assessment would not be complete. The literature on multi-hazard or the relationship between different hazards is however still lacking (Kappes et al., 2012; Gill and Malamud, 2016). Besides being a newer subfield of geohazards, this is also due to the difficulty of making a multi-hazard assessment. As Kappes et al. (2012) said: "Multi-hazard risk analyses are not just the sum of single hazard risk examinations." Hazards influence each other, can have very different causing factors and can have

very different consequences for their environment (Kappes et al., 2012). There is thus a need from the scientific world for more studies within the multi-hazards field (Chen et al., 2010; Gill and Malamud, 2016; Marzocchi et al., 2012).

St. Eustatius is an example of a small island in the Caribbean that sees many different types of hazards. The island is only 21 km^2 in size and has only one airport and one harbour. St. Eustatius is prone to several hazards due to being a volcanic island in the Atlantic hurricane zone. The island has been struck by earthquakes, hurricanes, tropical storms and volcanic eruptions (Roobol and Smith, 2004; MacRae and Esteban, 2007). Less well-documented hazards on the island are the occurrence of landslides and floods. However, due to the steepness of the terrain and loose soil material, but also the frequent tropical storms, hurricanes and earthquakes, a high susceptibility to slope failure is expected. Besides this MacRae and Estaban (2007) also mention in their report that landslides and floods are occurring on the island. However, although there are several testimonies and mentions of landslides and floods occurring, there is currently no known database of historical landslides or flood hazards on the island. Therefore, this study tries to map the landslide and flood problems on St. Eustatius.

1.1 Research objective

The objective of this study is to create a multi-hazard map of the landslide and flood hazards on St. Eustatius. The study analyses the historical occurrences of the landslide and flood hazards and estimates the magnitude of these hazards for different return periods. To achieve this objective, a hazard inventory and a quantitative hazard assessment of the landslide and flood hazards using the deterministic model openLISEM are made.

The anticipated output of the study will be:

- Historical hazard inventory of St. Eustatius
- Modelled landslide hazard map of St. Eustatius for different return periods (1, 5, 10, 50 yr.)
- Modelled flood hazard map of St. Eustatius, using the same return periods

Chapter 2 Study area

The following chapter gives a background of the study area, St. Eustatius. It discusses the topography, geology, geomorphology, climate and the record of historic hazard occurrences on the island.

2.1 Introduction

St. Eustatius is a small volcanic island located in the northern part of the Lesser Antilles in the Caribbean (see fig. 2.1). St. Eustatius has been a special municipality of the Netherlands since 2010, a Dutch description used for public bodies ranking between a municipality and a province. The island is only 21 km^2 and has 3,250 inhabitants (CBS, 2017). The capital and only city on the island is called Oranjestad. This city lies at the foot of the Quill volcano.

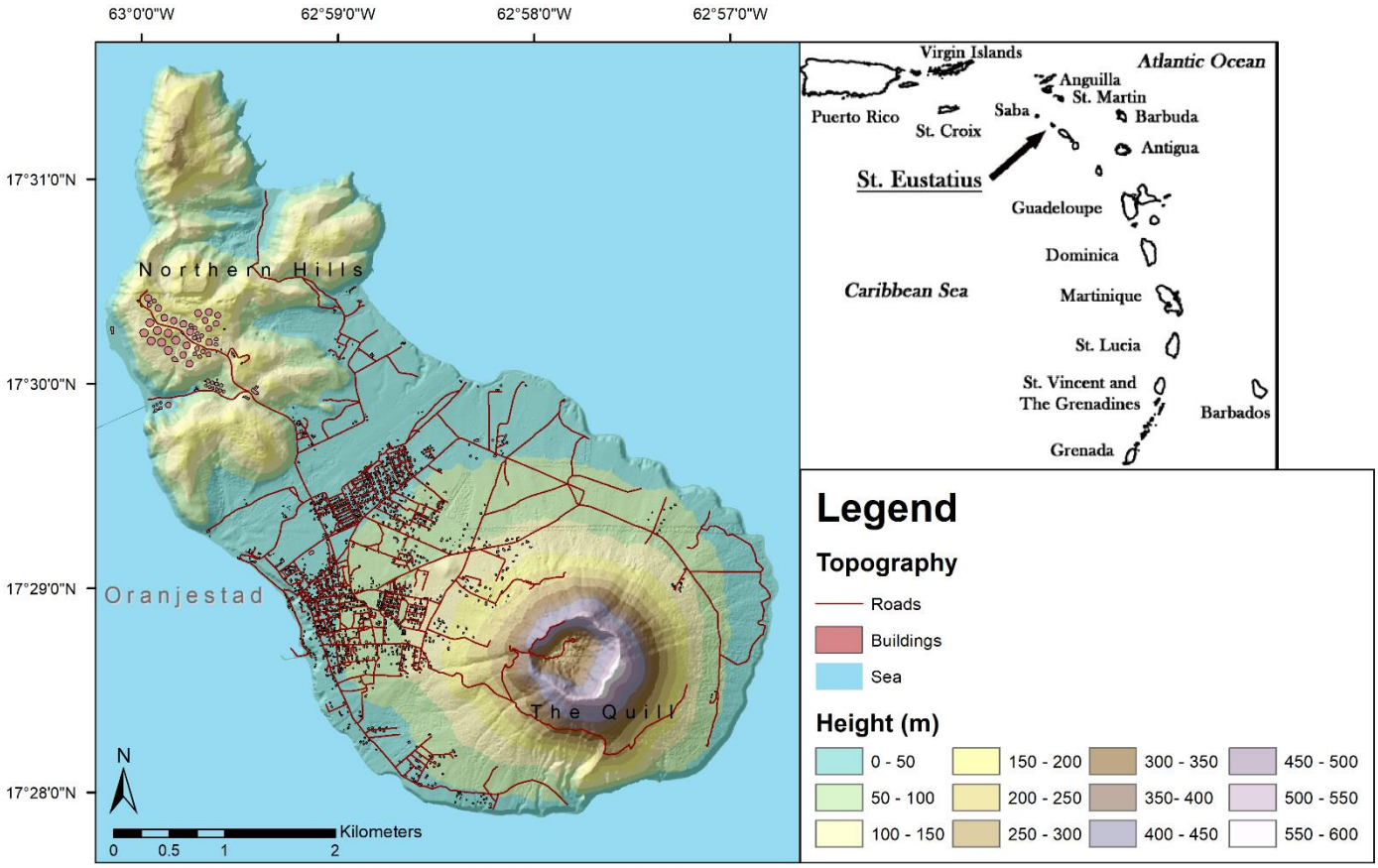

Figure 2.1: Map of St. Eustatius with inset (taken from De Freitas et al., 2012) showing the location in the Lesser Antilles.

2.2 Geology

Previous studies have not yet found an exact age for the island of St. Eustatius. Westermann (1956) dated the oldest formation on the island to end Pleistocene. However, Roobol and Smith (2004) estimated the age of the oldest geological unit at around 500,000 years. The island consists of three geological units: the Quill volcano, the northern hills and a limestone formation in the south (Westermann, 1956). These geological units are shown on the geological map of figure 2.2. The lithology of the island is mainly of volcanic origin. The northern section of the island consists of several older volcanic centres and is the oldest part of the island (Roobol and Smith, 2004). The lithology of this unit consists of andesite tuff, tuff breccia and andesite lava (Westermann, 1956). The unit contains several faults (fig. 2.2). The intermediate formation is the slab of limestone resting on the southern slopes of the Quill volcano, called the White Wall (fig. 2.2 and 2.3). When the Quill volcano formed, this slab of limestone was uplifted from the ocean floor with the volcano and formed White Wall (Roobol and Smith, 2004). The youngest formation of the island is the Quill volcano (Roobol and Smith, 2004). An exact date for the most recent eruption of the Quill volcano has not been found (Roobol and Smith, 2004).

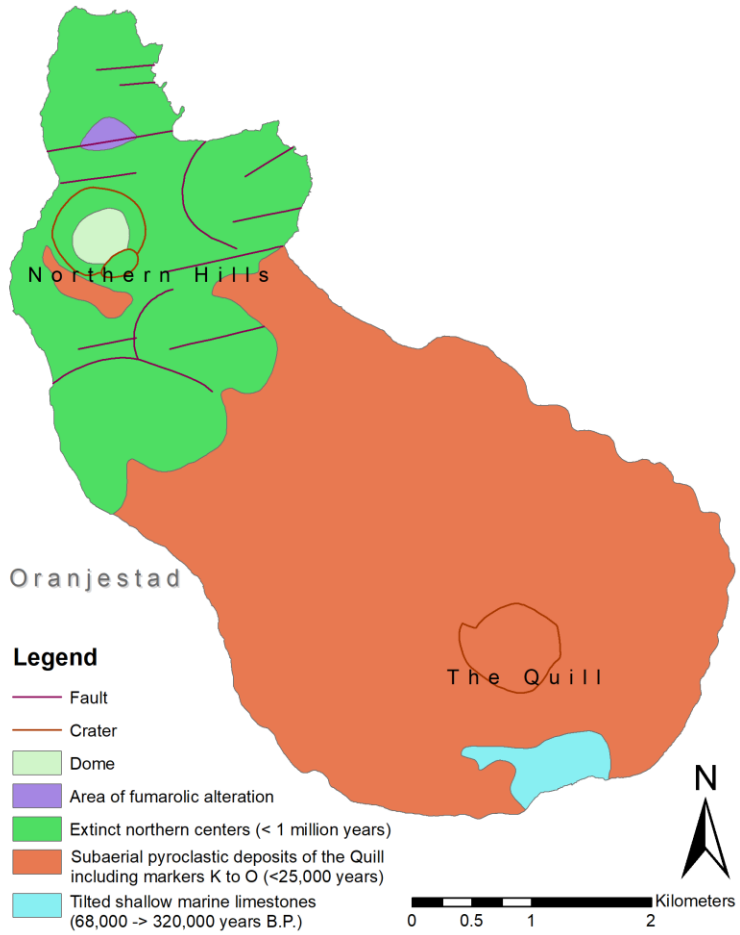

Figure 2.2: Geological map of St. Eustatius. Data from Roobol and Smith (2004).

Figure 2.3: White Wall (MacRae and Esteban, 2007).

2.3 Geomorphology

The geomorphology of the island can be divided into the northern part and the southern part (fig. 2.4). The southern part of the island is dominated by the Quill or the main stratovolcano. The morphology of this volcano is characterized by smooth, steep slopes, that are very active, as shown on the geomorphological map (fig.2.4). The slopes of the Quill are almost completely covered by volcanic ash, lapilli and tuffs originating from the Quill (MacRae and Esteban, 2007; Augustinus et al., 1985). The material grain size decreases downslope (MacRae and Esteban, 2007).

The northern part of the island is called the Northern Hills. These hills are much rougher than the Quill. The irregular relief is caused by the differences in the resistance of the geology (Augustinus et al., 1985). The valleys in the Northern Hills are filled with both alluvial and colluvial deposits, indicating a high activity as well. More details on the soil composition of St. Eustatius are given in the soil map in appendix A.

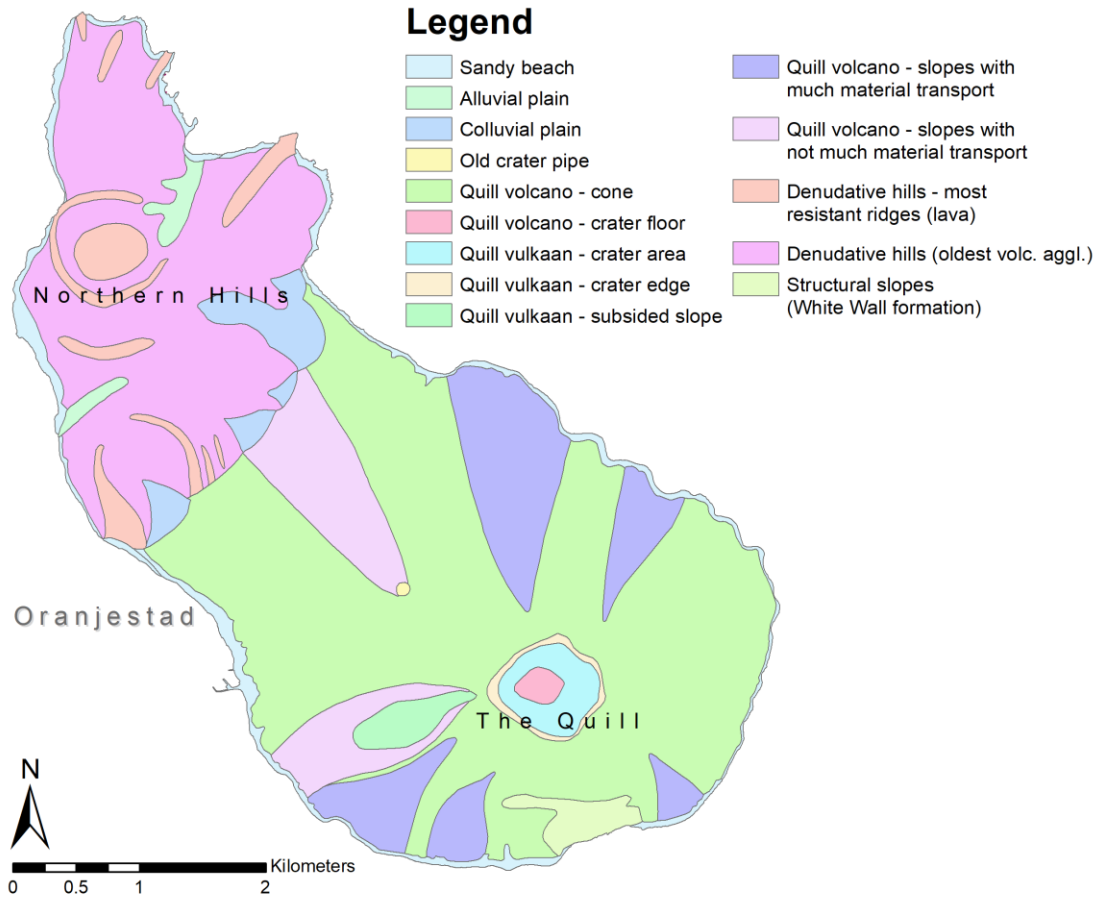

Figure 2.4: Geomorphological map of St. Eustatius. Data were taken from Karssen (1973).

2.4 Climate

The climate of the island is tropical (MacRae and Esteban, 2007). The average minimum temperature varies between 22.3 °C and 25.0 °C (De Freitas et al., 2012). The temperature does not change much throughout the year, as can be seen in figure 2.5.

The average yearly precipitation varies significantly. According to De Palm (1985), the average yearly precipitation was 1073 mm in the period 1881-1980, while De Freitas et al. (2012) mentions a yearly average precipitation of 986 mm in the period 1971 - 2000. The months August to November see on average more precipitation than the other months (fig. 2.5). This coincides with the Atlantic hurricane season which lasts from June 1st until November 30th. Due to the difference in height between the Quill and the rest of the island, there is a slight difference in average precipitation at these locations (MacRae and Esteban, 2007; Augustinus et al., 1985). The yearly average precipitation on the Quill is 1500-2000mm, while the lowlands tend to be very dry (MacRae and Esteban, 2007; De Freitas et al., 2012). This is also the reason why there is no substantial surface water on St. Eustatius.

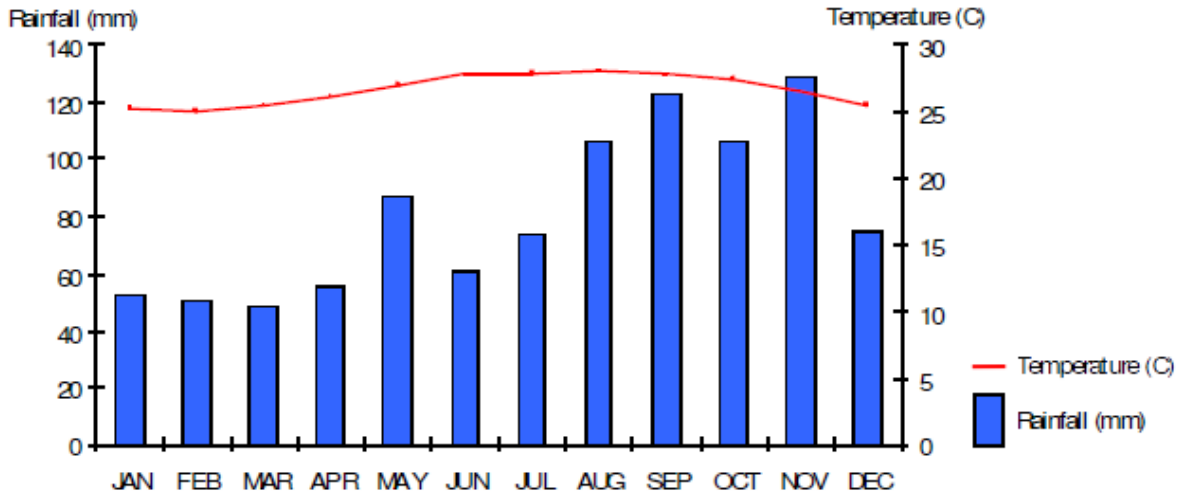

Figure 2.5: Average precipitation and temperature for 1971-2002 at the Franklin D. Roosevelt Airport, St. Eustatius (MacRae and Esteban, 2007).

2.5 Historic record of hazards

Since St. Eustatius is a volcanic island in the Atlantic hurricane zone, the island is exposed to many different hazards. The hazards that are known to have occurred are tropical storms, volcanic eruptions, earthquakes, landslides, floods and cliff erosion (MacRae and Esteban, 2007).

Tropical storms strike the island yearly and the island has experienced several hurricanes (see fig. 2.6 for the hurricane tracks). Every 4-5 years the island is hit by a major hurricane (MacRae and Esteban, 2007). Besides the direct damage, the storms and hurricanes have also led to an increase in erosion, debris flows and floods (MacRae and Esteban, 2007). The last major storms that hit the island were the hurricanes Irma and Jose in 2017. The damage on St. Eustatius was moderate. However, there were still 12 houses badly damaged and the communication networks were down for a couple of hours (The Daily Herald, 2017b; Rijksoverheid, n.d.).

The volcano on the island is dormant. The last eruption on the island is dated as less than 8,000 years ago and might even be about 1,600 years ago (Roobol and Smith, 2004). However, there is evidence that the groundwater on St. Eustatius is heated (Roobol and Smith, 2004), which would mean that there is still a possibility of an eruption.

As the island lies on the Caribbean plate, near the border with the North American Plate and the subducting South American Plate, it is also prone to earthquakes. Earthquakes are happening monthly, but most of them are only minor earthquakes. The last big earthquake near St. Eustatius had a

magnitude of 5.2 and struck the island on the 24th of December 2017, with the epicentre about 70km of the eastern coast.

A less well-documented hazard on the island is the occurrence of landslides. There are several testimonies of people on the occurrence of landslides, but there is no known information on the frequency, distribution, or magnitude of the occurrences. Due to the steepness of the terrain and loose soil material, but also the frequent tropical storms, hurricanes and earthquakes, it is however likely that there is a high susceptibility to slope failure.

Erosion, which is normally regarded as a slow hazard, causes a lot of problems on St. Eustatius. According to MacRae and Esteban (2007), the St. Eustatius National Parks (STENAPA) found a cliff erosion rate of up to 2.0 m/yr. when monitoring the eastern beach cliffs between 2004 and 2006. This is a very significant rate of erosion, which causes major problems for the population and can increase the landslide susceptibility at these sites.

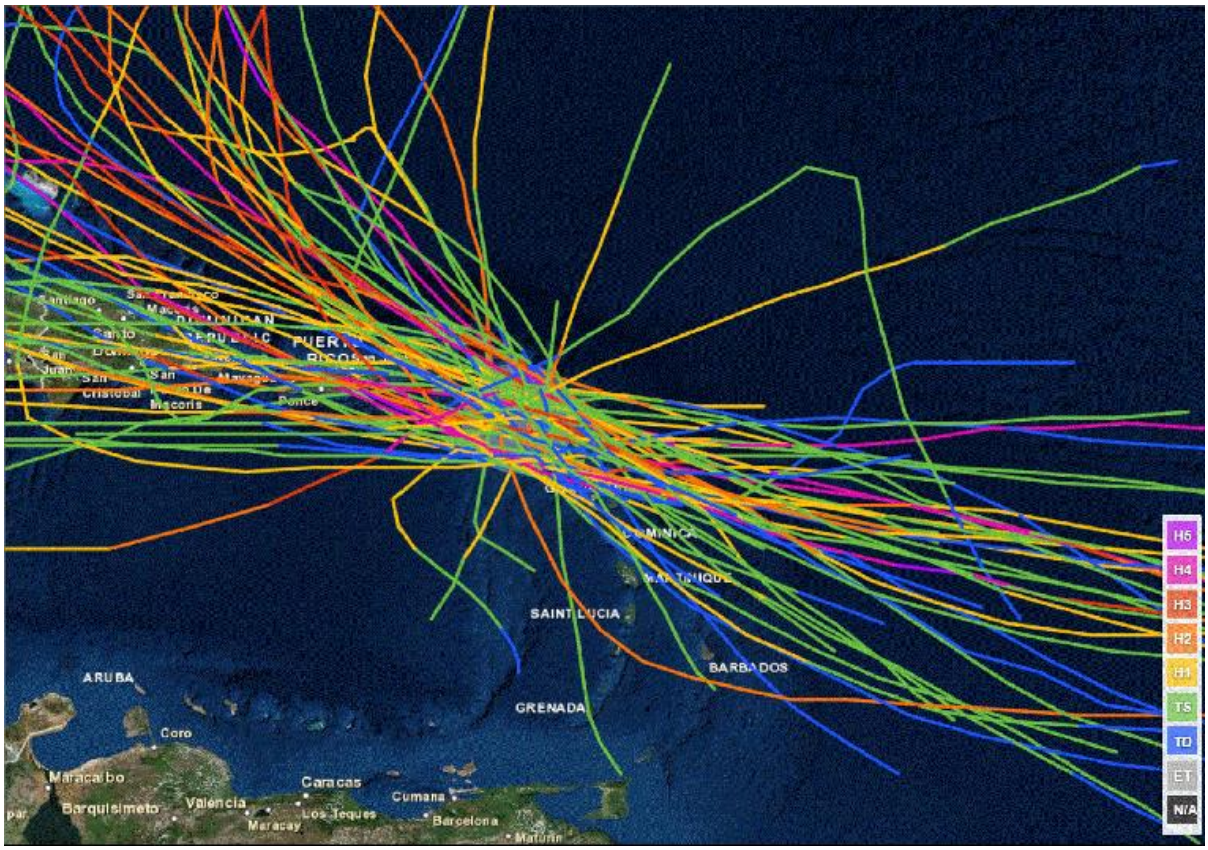

Figure 2.6: tropical cyclones passing within 110 km of Saba and St. Eustatius with their corresponding category (1851-2013) (MDC, 2014).

Chapter 3 Theoretical background

The following chapter discusses the theoretical background of hazard assessment and the processes of the different hazards considered in this study, i.e. landslides and floods.

3.1 Hazard assessment

A hazard assessment is an assessment of the features and probability of a potential hazard. This assessment does not include the (potential) damage or loss to the environment of said hazard since this is only included in a vulnerability or risk assessment (Van Westen et al., 2006).

There are many methods that can be used for making a hazard assessment (fig. 3.1). However, before discussing these methods, it is first important to discuss the definition of a hazard.

3.1.1 Definition hazard

A hazard can be expressed as the probability of the occurrence of an event with a certain magnitude and spatial extent (Van Westen et al., 2006). A hazard thus consists of a temporal component, a spatial component and a magnitude or an intensity component.

How the intensity or the magnitude of a hazard is defined, is dependent on the type of hazard that is considered. However, it is important that the expression of the magnitude can be linked to the potential damage the hazard can cause to its surroundings. With earthquakes, the energy release is often used to express the magnitude of the event (Guzzetti et al., 1999). In the case of floods, the magnitude is often expressed as the height of the floodwater above the surface or river discharge (Kappes et al., 2012). For landslides, there are several factors that can be linked to the damage potential. Examples of these factors are the depth of the failure plane, the volume of failed material (in case of a point-based event description) and debris flow depth or speed (when considering debris flows). The decision of the used factor describing the landslide hazard magnitude is often based on the limitations of the used model or mapping method.

The spatial component of a hazard expresses the spatial extent of the potential hazard that is considered. The spatial component of a flood hazard is equal to the maximum extent of dangerously high floodwaters. In the case of landslides, the most complete description would contain the area of slope failure and the area of deposition (i.e. where the failed material is deposited). However, due to

model and mapping limitations, the definition of the spatial extent of landslides is inconsistent between different studies, like the definition of the landslide hazard magnitude.

The temporal probability is based on either the return period of the hazards themselves or on the return period of the hazard triggers, which can be used as a proxy for the return period of the hazard.

3.1.2 Hazard assessment methods

A complete hazard assessment must evaluate each of the mentioned hazard components. The methods for a hazard assessment can be divided into two main categories: qualitative assessment methods and quantitative assessment methods. Figure 3.1 from a study by Aleotti and Chowdhury (1999) shows how these categories can be further subdivided into different methods for a landslide hazard assessment. A similar diagram like the one in figure 3.1 can also be applied to flood hazard assessment. However, qualitative methods are not used very often in flood hazard research. One study using a qualitative flood hazard assessment method that could be found was Weerasinghe et al. (2018).

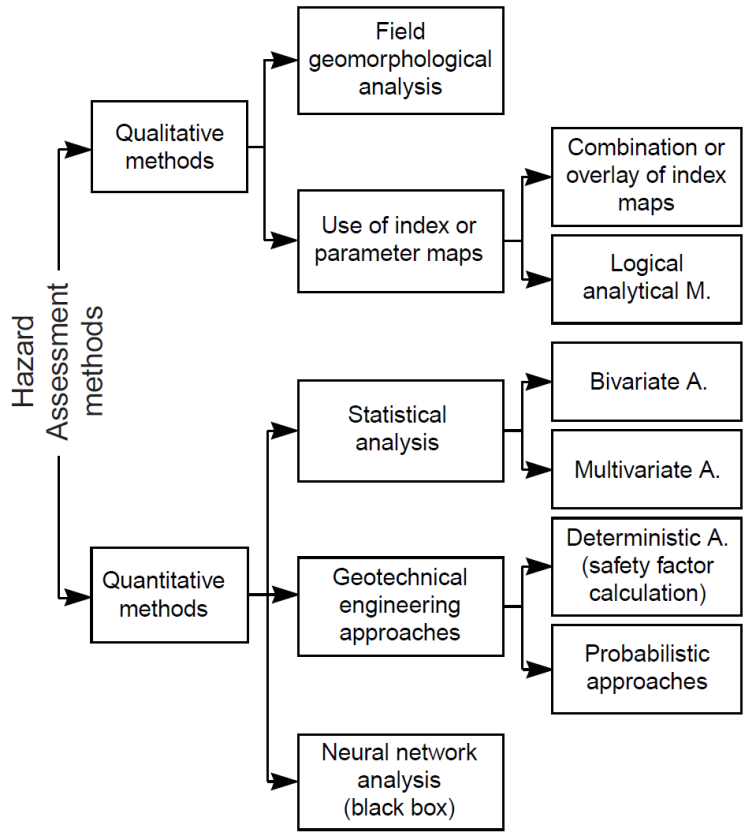

Figure 3.1: Overview of the different methods used in landslide hazard assessment research (Aleotti and Chowdhury, 1999).

Quantitative vs. qualitative methods

A qualitative method is a method that only uses descriptive qualitative terms in the resulting hazard classification (Guzzetti et al., 1999). They are solely based on the judgements of the researcher performing the assessment (Aleotti and Chowdhury, 1999). A qualitative method thus dependents mainly on expert knowledge.

One of the advantages of using a qualitative method is that the analysis is not restricted to known relationships between factors and hazard occurrences or their statistical relevance. Besides this, the data demand for the assessment is generally also lower than for quantitative assessments (Van Westen et al., 2006). On a downside, the assessments cannot be translated to other areas and are often difficult to update when changes occur in the study area (Aleotti and Chowdhury, 1999). The site-specificity and qualitative results also make it impossible to compare the resulting hazard maps of one area to another.

Quantitative methods use a more objective approach and quantify the features of the selected hazard(s) (Guzzetti et al., 1999). Quantitative analyses have the advantage that the methods are more objective and produce quantified results, which can be compared to results from similar methods. Due to the objectivity, the results are also repeatable and more easily updated when situations in the study area change. Dai et al. (2002) also pointed out that quantitative methods are more suited for large-scale studies, while qualitative methods are more suited for small-scale studies.

Neither of these methods is thus better than the other as they both have their advantages and disadvantages. The suitability of either a qualitative method or quantitative method is completely dependent on the study area, data availability and the requirements of the hazard assessment (Dai et al., 2002; Van Westen et al., 2008).

3.2 Floods

In this study, floods are defined as hazardously high overland flow depths that can cause damage to property or are a danger to people. Normally a flood would be considered a higher than normal discharge from a channel leading to water extending out of the normal banks of the channel. However, since this study only considers overland flow, the concept of pluvial flooding is used instead. Pluvial flooding is a definition used for a flood event caused by overland flow and ponding due to extreme rainfall events (Maksimović et al., 2009).

According to Teng et al. (2017) hydrodynamic or physically-based models are the most used models within flood hazard research. Currently, many different hydrodynamic methods are available, ranging from 1D to 3D models. The study by Teng et al. (2017) gives an overview of well-known hydrodynamic flood hazard models. A study by Van Dijk et al. (2014) showed that, for modelling pluvial flooding in urban areas that are situated in a transition zone from a hilly to flat morphology, a 1D-2D coupled simulation model is better suited than a surface model (2D). However, this study also stated that a surface model is sufficient enough for an initial flood hazard assessment.

3.3 Landslides

The most used definition of a landslide is: "the movement of a mass of rock, earth or debris down a slope" (Cruden, 1991). Bates and Jackson (1987) also state that this downslope movement should occur under the main influence of gravity. In 1978, Varnes developed a classification system for landslides that is still used in current studies (Hungr et al., 2014). This classification was based on the type of movement and type of material. Type of material was divided into rock, earth and debris and type of movement was divided into fall, topple, slide, spread and flow (fig. 3.2).

TYPE OF MOVEMENT		TYPE OF MATERIAL		
		BEDROCK	ENGINEERING SOILS	
			Predominantly coarse	Predominantly fine
FALLS		Rock fall	Debris fall	Earth fall
TOPPLES		Rock topple	Debris topple	Earth topple
SLIDES	ROTATIONAL	Rock slide	Debris slide	Earth slide
	TRANSLATIONAL			
LATERAL SPREADS		Rock spread	Debris spread	Earth spread
FLOWS		Rock flow (deep creep)	Debris flow (soil creep)	Earth flow
COMPLEX		Combination of two or more principal types of movement		

Figure 3.2 Landslide classification based on the type of movement and material (Varnes, 1978).

3.3.1 Terminology

The main topographical features of a landslide are shown in figure 3.3. Of these features, the failure plane and runout distance are the most important when discussing landslide hazards. The failure plane is the plane on which the conditions for failure are met, defining both the location and volume of slope failure. The runout distance is important when talking about the potential damage a landslide can cause, as this defines how far the material from the landslide reaches and if constructions are within the safe zone or not.

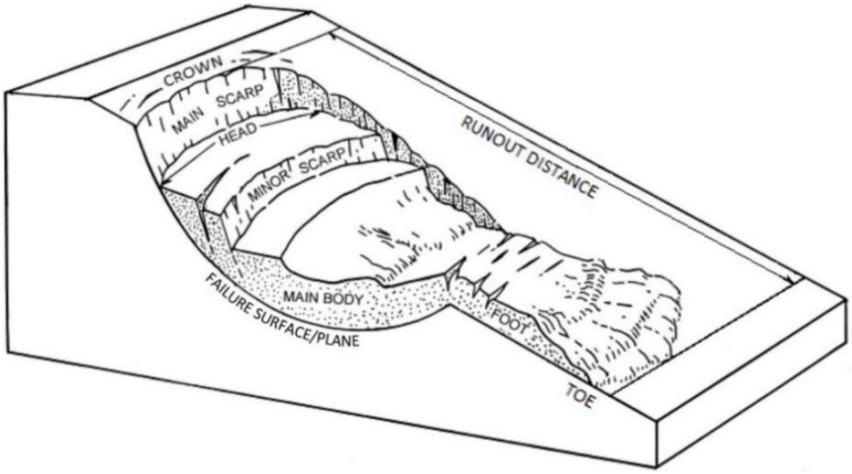

Figure 3.3: Schematisation of a landslide and its topography (modified after Cruden and Varnes, 1996).

3.3.2 Causes

All types of landslides are caused by an increase in the stresses acting on the slope or a decrease in the strength of the slope. When the stresses exceed the strength of the slope, failure occurs at a failure plane and a landslide forms. This is often described with the Factor of Safety (FoS), see also equation 3.1:

$$FoS = \frac{resisting\ stresses\ (shear\ strength)}{driving\ stresses\ (shear\ stresses)}. \quad (3.1)$$

When the FoS ≥ 1, the slope exists in a stable situation and when the FoS is < 1, the slope is unstable and failure occurs.

Resisting stresses

The resisting stresses or shear strength are the forces that prevent the slope from failing (fig. 3.4). They are controlled by the normal stress and the material properties of the soil or bedrock. The shear strength can also be expressed with the Mohr-Coulomb criterion:

$$\tau = c + \sigma tan\phi, \tag{3.2}$$

where τ is the shear strength (kPa), c is the cohesion (kPa), σ is the normal stress (kPa) and ϕ is the internal friction angle.

Thus, the shear strength of the soil consists of the cohesion of the soil and the internal friction of the soil grains grinding against each other (σ*tanϕ). The cohesion is the force that keeps the particles of the soil together, using the molecular bonds between them. It is independent of external factors, e.g. weight from the soil above (Smith, 2001). The internal friction of the soil is determined by the internal friction angle (tanϕ) and the normal stress(σ) acting on the soil. The internal friction angle is a fixed material property of the soil, while the normal stress is dependent on the weight of the soil above.

The soil moisture content of the soil has a big influence on the resisting stresses. It increases the pore pressure which decreases the effective normal stress acting on the soil (Bogaard and Greco, 2016). The effective normal stress is the part of the normal stress that acts on the solid part of the soil (grains) alone. As water is incompressible like the grains in the soil, it can bear part of the normal stress, reducing the effective normal stress acting on the soil particles. The higher the pore pressure, the more normal stress the soil moisture bears. This is also described by equation 3.3:

$$\sigma' = \sigma - u, \tag{3.3}$$

where σ' is the effective normal stress, σ the normal stress and u the pore pressure. Because of this, the soil moisture content has a negative effect on the internal friction of the soil.

An increase in soil moisture content can also decrease the apparent cohesion of the soil. The apparent cohesion consists of the cohesion defined by the soil properties and the extra cohesion provided by e.g. soil suction and plant roots. Soil suction is the force of the soil particles pulling on the water inside the soil and thus also on other particles that are surrounded by water. This force becomes stronger when there is less water available in the soil (Kutílek and Nielsen, 1994). A decrease in soil moisture content, leading to an increase in soil suction, thus also increases the strength of the soil by creating a stronger bond between the grains (Ho and Fredlund, 1982).

When all these components are added to the equation for the shear strength from the Mohr-Coulomb criterion, equation 3.3 becomes:

$$\tau = c' + \sigma' tan\phi, \tag{3.4}$$

where c' is the apparent cohesion and σ' the effective normal stress.

Driving stresses

The driving stresses are the stresses that force the slope downwards (fig. 3.4). These stresses are caused by the gravitational force acting on the slope, which depends on the weight of the soil. The weight of the soil is affected by the density of the soil particles, the weight of the water inside the soil, and the additional weight from vegetation and human structures. The slope angle also affects the driving stresses, as a higher slope angle increases the gravitational forces working along the slope (fig. 3.4).

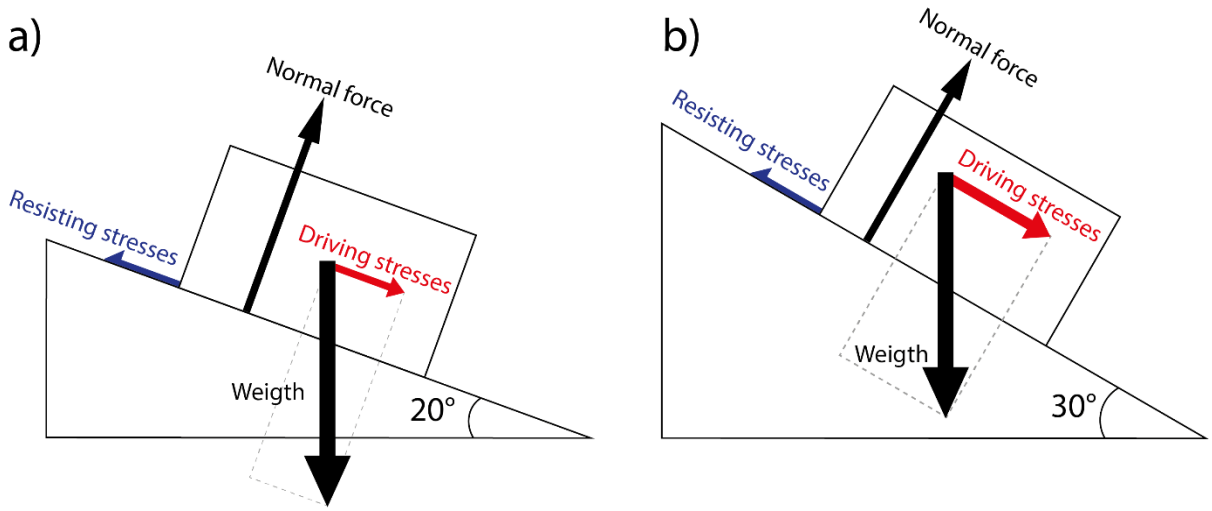

Figure 3.4: Effects of change in slope angle on the slope stability conditions. a) shows a stable situation where the driving stresses (red) are equal to the resisting stresses (blue) and the slope angle is 20°. b) shows an unstable situation where only the slope angle is increased to 30°, resulting in higher driving stresses (red).

Causes and triggers

The slope stability is thus mainly influenced by the weight of the soil, the soil moisture content and the slope angle. There are generally three ways in which these factors are changed and landslides are induced: seismically, by long- or short-term rainfall and by human influence.

Earthquakes can induce landslides by causing (quick) variation in the stresses acting on the slope (Duncan et al., 2014). Due to this variation, the effective driving stresses (the forces working downslope) can become bigger than the effective resisting stresses (the forces working upslope).

Rainfall induces landslides by changing the soil moisture content (on short-term) or the groundwater level (on long-term). This changes the pore pressure, affecting the resisting stresses, and increases or decreases the chance of failure. Furthermore, rainfall can also lead to an increase in erosion when it causes overland flow. If this erosion is focussed on the toe of the slope, the slope angle increases, increasing the susceptibility to failure.

Human influence consists of several causes and triggers. Road and building construction increases the weight on the slope and can also increase the slope angle when part of the slope is excavated. Construction on the slope can also affect the hydrological environment and increase the soil moisture content and erosion. The removal of vegetation can also lead to an increase in erosion.

3.3.3 Debris flows

Debris flows, and other types of flows, are different from other landslides as they consist of particles that travel independently of each other within the flow mass (Dikau et al., 1997). This contrasts with other landslides where the failure forms a coherent block. Due to the higher water content inside debris flows, they are also more mobile than other types of landslides (Takahashi, 2014). Their velocities and runout distances are therefore often much higher and longer, which makes them more dangerous as the affected area can be much larger and the warning time much shorter.

The causes for debris flows are the same as the causes for landslides, although the sediment needs to be more saturated than a normal landslide (Jakob and Hungr, 2005 and Dikau et al., 1997). Debris flows often also form out of translational or rotational slides that liquefy during their run down the slope (Jakob and Hungr, 2005).

3.3.4 Modelling landslides and debris flows

Within quantitative hazard assessment, there are several modelling approaches that can be used. A choice can be made between statistical, probabilistic and deterministic models. Several studies compared the applicability of different quantitative methods for landslide hazard assessment at different mapping scales (Soesters and Van Westen, 1996; Aleotti and Chowdhury, 1999). These review studies showed that statistical and probabilistic analyses are better suited for regional study areas and that deterministic methods are better suited for large-scale study areas. This can be explained by the demand for more detailed data for the physically-based methods, which is difficult to achieve on smaller scales. Besides this, statistical analyses are more difficult to perform on a large-scale, where often only one or a few landslides are registered in the landslide inventory of the study areas.

Another difference between the statistical or probabilistic methods and the physically-based methods is the importance of the landslide inventory. Generally, statistical and probabilistic models that are used for landslide hazard assessments rely heavily on historical landslide databases to determine frequency-magnitude relationships or causal relationships used in the models (Pardeshi et al., 2013). For validation purposes, deterministic methods also need a large landslide inventory. However, although it would be better for these validation purposes to have an extensive landslide record, a smaller or less detailed inventory could also be acceptable.

Deterministic methods

Most deterministic landslide models use the Factor of Safety (eq. 3.1) as a principle to calculate the slope stability. There are generally two methods used to calculate the factor of safety: the method of slices and the infinite slope method.

The method of slices divides the potential failing mass into several vertical slices. This makes it easier to deal with circular failure planes when calculating the slope stability. The forces working on the mass can be calculated for each individual slice on a planar surface, instead of a curved surface. The forces can then be summed for all slices and used to calculate the safety factor. This capability of modelling curved surfaces makes it possible to model deep-seated landslides, which often have circular failure planes.

The infinite slope method is a much simpler method, used for shallow translational landslides. The method assumes that the failure plane has an infinite length and lies parallel to the surface, which makes it possible to treat the entire landslide as one rectangular slice. Since the depth of the failure

plane of a shallow translational landslide is negligible compared to the length of the failure surface, this assumption can be made when dealing with translational shallow landslides.

Probabilistic and statistical methods

Both probabilistic and statistical models use past landslide events to model the probabilities of future landslide occurrences. For probabilistic landslide hazard modelling, there are three commonly applied methods: First Order Second Moment method (FOSM), Point Estimate method and Monte Carlo Simulation method (Aleotti and Chowdhury, 1999). A more detailed description of these methods is given in Chowdhury (1984) and Nguyen and Chowdhury (1985).

For statistical landslide hazard modelling, there are two main methods: bivariate statistical analysis and multivariate statistical analysis (Aleotti and Chowdhury, 1999). The bivariate analysis looks at the individual impact of the different input parameters and later combines these impacts into a single weighted layer for the construction of the hazard map (Van Westen, 2000). The multivariate statistical methods analyse the parameters together and define the weights for unique combinations of the parameters (Van Westen, 2000).

Chapter 4 Methods

The following chapter will describe and discuss the methods used in this study for the assessment of the landslide and flood hazards on St. Eustatius. The chapter will first give an overview of the used methods for the hazard assessment. After this, the chapter will describe the methods used for the construction of the hazard inventory. Lastly, the chapter will discuss the used model (openLISEM) and give a description of how the data for the model input was collected and created.

4.1 Hazard assessment

Since there was no inventory available of both the landslide and flood hazards on St. Eustatius, it was decided to use a quantitative deterministic hazard assessment. A deterministic approach has the lowest requirements for the inventories of the hazards, as shown by (Pardeshi et al., 2013). Besides this, a deterministic model is also more suited for a large-scale study (Soesters and Van Westen, 1996; Aleotti and Chowdhury, 1999).

Figure 4.1 gives an overview of the general approach that is used in quantitative hazard assessment. This general approach uses the following steps: data collection, modelling, validation and hazard classification (Beguería, 2006).

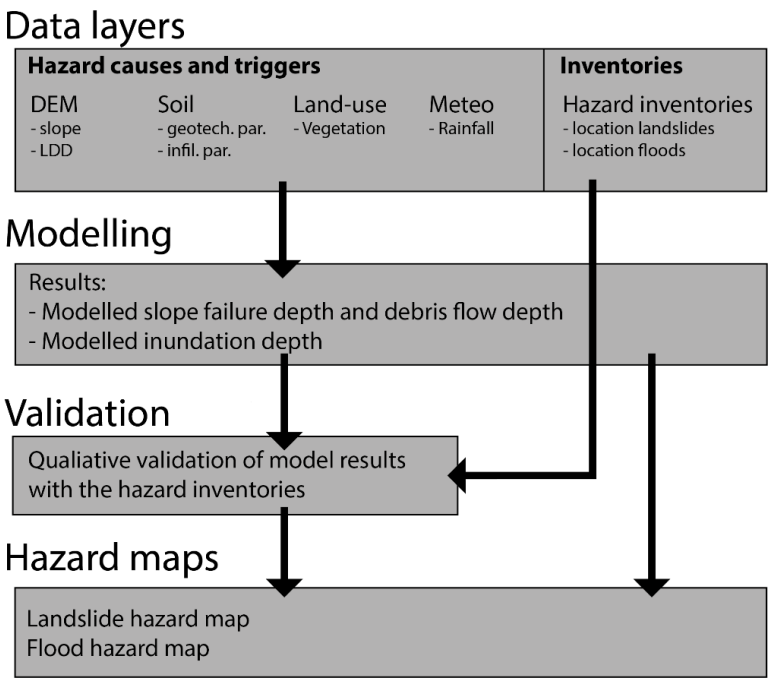

Figure 4.1: Block-diagram of the general approach for deterministic hazard assessment.

The first step of the hazard assessment is the collection and preparation of the data that is needed to model the studied hazards and for the validation of model results. The requirements of the data are based on the requirements of the chosen model, the scale of the assessment, the studied triggers and the validation method.

After the data has been collected and prepared, the chosen model can be used to model the probability, spatial extent and magnitude of the studied hazards. It is important that the used model can quantify each of these parameters, as they are all critical in the hazard assessment procedure.

The model results should also be validated, to assess the accuracy of the model results. This can be achieved by using hazard inventories encompassing the features of historical hazards that occurred in the study area. In this study, the validation procedure is performed qualitatively since this limits the requirements of the needed hazard inventories.

Lastly, to construct the final hazard maps, the model results should be classified. This classification can be performed using several methods. In this study, the classification is performed using the temporal probability of a hazard. A threshold on the magnitude of the modelled events is then used to determine if the modelled events are hazardous or not.

4.1.1 Landslide hazard assessment

Within deterministic landslide modelling, there are several methods that can be used, as explained in Chapter 3. For the assessment on St. Eustatius the infinite slope method is the most suited of these methods since the geological map is lacking in its geotechnical information, which makes it difficult to model deep-seated landslides. The knowledge on occurring landslides on St. Eustatius also showed that only shallow landslides were occurring regularly on the island. This study therefore only considers the occurrence of shallow translational landslides.

The chosen landslide model should preferably model the location of landslide events, the depth of the failure plane and the runout extent through debris flow modelling. These parameters can then be used to determine the magnitude of the modelled landslide. A hazard map can then be constructed based on the magnitudes and locations of the modelled landslides.

Regarding the landslide triggers, only the impact of rainfall was considered in this study, since there was no information on the ground acceleration values for the earthquakes that occurred near St. Eustatius.

4.1.2 Flood hazard assessment

As stated in Chapter 3, a deterministic model would be the best option for modelling pluvial flooding on St. Eustatius. Since the flood hazard assessment is performed on a large-scale, the chosen model should provide information on the inundation depth of the occurring flood events. This inundation depth can then be used in the classification of the flood hazard map.

4.2 Hazard inventory mapping

Since there was no database on historical landslide and flood hazards that occurred on St. Eustatius, this study also constructed a hazard inventory. Besides functioning as an initial hazard map, this inventory was also used as validation for the model results. However, since it is very difficult to find indications of historical floods, only a landslide inventory map was constructed during this study.

The hazard inventory map was constructed using field observations during a fieldwork on St. Eustatius. Due to a high vegetation cover and often dense cloud cover, earth observation techniques could not be used to construct this inventory. Besides this, it was also expected that the coastal cliffs would show a high landslide activity, which would not show up on the earth observational data.

The fieldwork on St. Eustatius lasted 3 weeks (from 13-06-2017 to 05-07-2017). During the fieldwork, the occurrences and indications of historic landslides (e.g. high erosion rate, instability) were noted at each visited location.

4.3 Description openLISEM

openLISEM or LISEM (the Limburg Soil Erosion Model) is a physically-based numerical model developed to simulate runoff, sediment dynamics and shallow floods for a single storm event. It was first published by De Roo et al. (1994). The model has since then been developed further and tested in many studies and reports on flooding risk and erosion (Jetten and Van den Bout, 2018). The main components of LISEM are:

- Soil water balance
- Overland flow
- Channel flow
- Channel flooding
- Erosion
- Sediment transport in all flows
- Multiclass sediment

Recently, a new hazard component was added to the model, which added the capability of simulating slope failure and debris flows. This makes openLISEM one of the few multi-hazard models that model debris flows, shallow landslides and flooding in one model (Van den Bout et al., 2017). A study by Van den Bout et al. (2017) is so far, the only study that has used openLISEM with this extension. The study by Van den Bout et al. (2017) tested the new version of openLISEM on a catchment on the island of Sicily, Italy. The study showed a model accuracy of 95.9 per cent when comparing the model results with a landslide inventory of the catchment.

The new version of openLISEM (v3.3) is the only available deterministic model that fills all the set requirements of the needed model. There are many other models that can model both landslides, debris flows and floods when combined with each other. However, this approach would require much longer computational run-times. Besides this, the models would also not be able to simulate the coupled processes of the modelled hazards, as only one-way relationships could be simulated due to the asynchronous approach.

A flow diagram of the new openLISEM model is shown in figure 4.2. This flow diagram shows that the model can be divided into three main classes: the hydrological processes, the sediment processes and the slope processes. In this study, only the simulations of the hydrological processes and slope processes are used.

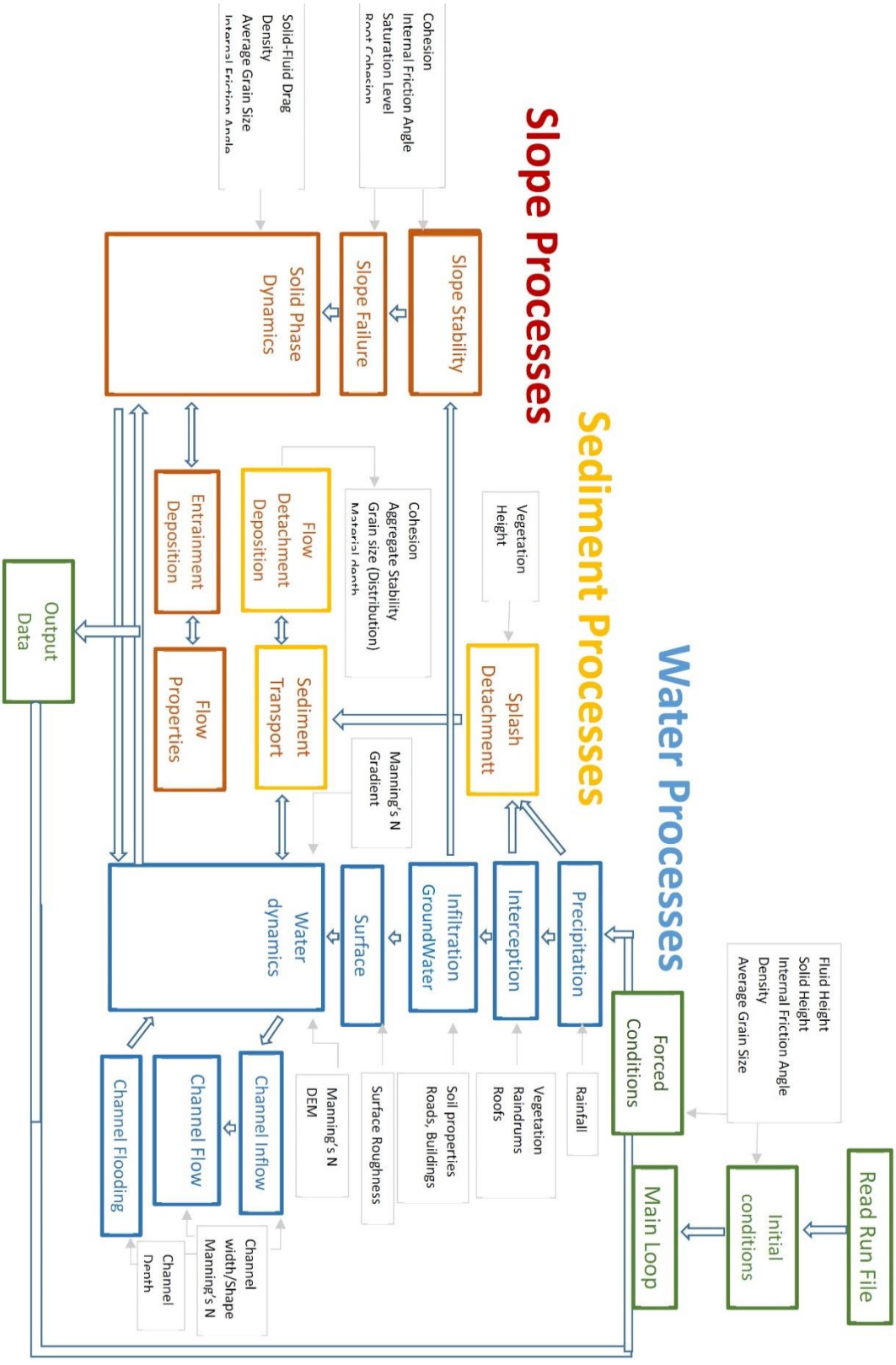

Figure 4.2: Flow diagram of openLISEM, modified after Jetten and Van den Bout (2018).

4.3.1 Hydrology

The hydrological part of the model consists of the following main processes (see also fig. 4.2):

- Precipitation
- Interception
- Storage
- Infiltration
- Overland flow

The equations (eq. 4.1 – 4.13) were all taken from the openLISEM manual (Jetten and Van den Bout, 2018). A more detailed description of the model can also be found in this manual.

Precipitation

OpenLISEM models rainfall from rainfall intensity data (mm h^{-1}), which can be given as temporal or spatio-temporal data. To correct for the fact that steeper slopes receive less rainfall per area, the width and length of each cell that receives rainfall are changed based on the slope of their local topography. The surface area of the cells with a steeper slope is in this way enlarged.

Interception

Interception is modelled for vegetation, buildings and rain drums. It is modelled as a fixed storage, as no evaporation is modelled, and rainfall that is not intercepted (throughfall) reaches the soil with the same intensity as the rainfall. The canopy interception is calculated with equations 4.1 (Aston, 1979) and 4.2 (Jetten and Van den Bout, 2018):

$$I_c = S_{max}\left(1 - e^{-k\frac{P_{cum}}{S_{max}}}\right) \tag{4.1}$$

$$k = 1 - e^{-(co*LAI)}\,, \tag{4.2}$$

where I_c is the total intercepted storage at a given time (mm), S_{max} is the maximum canopy storage, P_{cum} is the total precipitation (mm), co is the canopy openness (-) and LAI is the leaf area index (-). The S_{max} can be defined by the user in a map or calculated based on the LAI with empirical equations from Von Hoyningen-Huene (1981) and De Jong and Jetten (2007).

Storage

Storage is calculated at the surface as the storage of water in micro depressions (MDS). LISEM uses the surface roughness to calculate the fraction of water that is stored in these depressions and the water that is released as runoff. The equation that is used to calculate this was taken from Kamphorst et al. (2000):

$$MDS = 0.243\ RR + 0.010\ RR^2 + 0.012\ RR * S\ , \tag{4.3}$$

where MDS is the micro-depression storage (mm), RR is the standard deviation of the surface heights (mm) and S is the slope (m m^{-1}).

Infiltration

When water is inside the MDS it is available for infiltration into the soil. LISEM gives three different model options for calculating the amount of infiltration in a cell. These are:

- The Green & Ampt infiltration model
- Smith & Parlange model
- SWATRE multi-layered soil water model

The Green & Ampt infiltration model is an empirical infiltration model, that uses the hydraulic conductivity, porosity, initial soil moisture content and matric pressure to determine the infiltration rate. The Smith & Parlange model is an empirical infiltration model that uses the same input, but a slightly different equation for the infiltration rate. Lastly, the SWATRE model is the most detailed model of the three. It is a deterministic infiltration model that uses a detailed water-retention curve of the soil as input.

Since there was not much information about the hydraulic properties of the soil types on the island, the SWATRE model was not used. A test run with both the Green and Ampt method and the Smith and Parlange method showed that the impact of the different infiltration models on the results was minimal (see also appendix B). The only difference between the two methods was a failure at the western coast in the Green and Ampt method model run, whereas the run with the Smith and Parlange method did not show any failure at this location. Since failure at this location was expected, the Green and Ampt method was chosen to be used in this study.

The Green & Ampt (1911) method assumes that a wetting front parallel to the surface is moving downwards into the soil during infiltration. This reduces the needed modelled dimensions of the infiltration to only the vertical direction. The Darcy equation for vertical water flow can then be used,

which simplifies even further when the ponding height is assumed negligible. This gives the following equation:

$$f = -K_S\left(\frac{h_f - h_0}{Z_f}\right) = K_S\left(\frac{\psi}{Z_f} + 1\right), \tag{4.4}$$

where f is the infiltration rate (m s^{-1}), K_S is the saturated hydraulic conductivity, h_f the hydraulic head at the wetting front, h_0 the hydraulic head at the soil surface (=0, no ponding), Z_f is the depth of the wetting front (m) and ψ the matric pressure at the wetting front (h = ψ + Z) (m).

The depth of the wetting front can be calculated with the difference in theta and cumulative infiltrated water:

$$Z_f = \frac{F}{\theta_s - \theta_i}, \tag{4.5}$$

where F is the cumulative rainfall (mm), θ_s saturated moisture content (-) and θ_i is the initial moisture content of the soil (-).

Overland flow

OpenLISEM starts modelling overland flow only after the MDS has exceeded the threshold of 0.1*MDS or when the MDS has been filled up. Before this, the released water from the ponds is very little. The water available for overland flow can thus be calculated from the MDS (depth in m). The equation used in openLISEM is:

$$h_{runoff} = \max\left(0.0, (h - SDS) * \left(1 - e^{-h\frac{h-SDS}{MDS-SDS}}\right)\right), \tag{4.6}$$

where h_{runoff} is the height of the water available for runoff in the cell (mm), h is the water depth in the MDS (mm), SDS is 0.1*MDS (mm) and MDS is the storage capacity of the cell.

LISEM uses the full 2-D Saint-Venant equations or dynamic wave to describe both channel and overland flow. The Saint-Venant equations can be derived from the Navier-Stokes equations:

$$\frac{\partial u_x}{\partial t} + u\frac{\partial u_x}{\partial x} + v\frac{\partial u_x}{\partial y} = -\frac{\partial p}{\partial x}\frac{1}{\rho_f} + \upsilon\frac{\partial^2 u_x}{\partial x^2} + \upsilon\frac{\partial^2 u_x}{\partial y^2} \tag{4.7}$$

$$\frac{\partial u_y}{\partial t} + u\frac{\partial u_y}{\partial x} + v\frac{\partial u_y}{\partial y} = -\frac{\partial p}{\partial x}\frac{1}{\rho_f} + \upsilon\frac{\partial^2 u_y}{\partial x^2} + \upsilon\frac{\partial^2 u_y}{\partial y^2}, \tag{4.8}$$

where u is the flow velocity, *v* is the kinematic viscosity ($m^2 s^{-1}$), *p* the pressure (kPa) and ρ_f the density of the fluid (kg m^{-3}).

The friction terms in the Navier-Stokes equations can be neglected since kinematic viscosity can be assumed to be zero (eq. 4.9).

$$\upsilon \frac{\partial^2 u_x}{\partial x^2} + \upsilon \frac{\partial^2 u_x}{\partial y^2} = 0 \tag{4.9}$$

Furthermore, the pressure can be assumed to be hydrostatic (eq. 4.10).

$$p = \rho_f g h\,, \tag{4.10}$$

where g is the gravitational acceleration and h is the water depth.

Combining these simplifications (eq. 4.9 and 4.10) with the continuity equation (eq. 4.7 - 4.8) leads to the 2-D Saint-Venant equations:

$$\frac{\partial h}{\partial t} + \frac{\partial (h u_x)}{\partial x} + \frac{\partial (h u_y)}{\partial y} = q - I \tag{4.11}$$

$$\frac{\partial h u_x}{\partial t} + \frac{\partial \left(h u_x^2 + \frac{1}{2} g h^2\right)}{\partial x} + \frac{\partial (h u_y u_x)}{\partial y} = g h (S_x - S_{f,x}) \tag{4.12}$$

$$\frac{\partial h u_y}{\partial t} + \frac{\partial (h u_y u_x)}{\partial x} + \frac{\partial \left(h u_x^2 + \frac{1}{2} g h^2\right)}{\partial y} = g h \left(S_y - S_{f,y}\right)\,, \tag{4.13}$$

where q is the lateral inflow, I is the outflow, S_x and S_y are the slopes in the x- and y-directions (m m^{-1}) and $S_{f,x}$ and $S_{f,y}$ are the friction slope terms in the x- and y-direction (m m^{-1}).

LISEM solves these equations numerically using the equations behind FullSWOF2D. More information about this can be found in the LISEM user manual (Jetten and Van den Bout, 2018) and the source of this numerical solution, Delestre et al. (2014).

4.3.2 Slope processes

The slope processes are modelled in two parts in openLISEM. First, the slope stability and failure are calculated and then the failure volume is transported downslope as a debris flow. Equations 4.14 – 4.16 were all taken from Van den Bout et al. (2017).

Slope stability

LISEM uses the infinite-slope method to model the slope stability. With this method the safety factor is calculated using the following equation:

$$FoS = \frac{c' + ((\gamma - m\gamma_w)z)\cos(\beta)^2 \tan(\phi')}{\gamma z sin(\beta)\cos(\beta)}, \quad (4.14)$$

where *FoS* is the safety factor (-), *c'* is the apparent cohesion (kPa), *γ* the specific weight of the moist soil (N m^{-3}), γ_w the specific weight of water (N m^{-3}), *m* the ratio between the depth of the saturated zone and the soil depth (-), *z* is the soil depth (m), β is the slope of the soil section (m m^{-1}) and ϕ' the internal friction angle of the soil (-).

Since there is no known information about the subsurface, the failure plane needs to be calculated by the model as well. LISEM does this by determining if the cell is unstable using the FoS and the entire soil depth. When failure is discovered, LISEM uses an iterative process to determine the actual failure plane and failure volume. Besides this openLISEM also models the influence of the slope failure in one cell on the slope of the neighbouring cells using equation 4.15.

$$\beta = \operatorname{atan}\left(\frac{\max(h_x - h_{x-1}, h_x + h_{x+1})}{dx}\right), \quad (4.15)$$

where β is the slope of the cell (m m^{-1}), h_x is the elevation of the current cell (m), h_{x-1} is the elevation of the previous cell (m), h_{x+1} is the elevation of the next cell (m) and dx is the cell size (m).

The maximum slope is then used as input in eq. 4.14 and the FoS is set to 1 since failure occurs. eq. 4.14 then becomes:

$$FoS = 1 = \frac{c' + (\gamma - m\gamma_w)z \cdot cos\left(atan\left(\frac{h-h_0}{dx}\right)\right)^2 \cdot tan(\phi')}{\gamma z \cdot sin\left(atan\left(\frac{h-h_0}{dx}\right)\right) \cdot cos\left(atan\left(\frac{h-h_0}{dx}\right)\right)}. \quad (4.16)$$

Equation 4.16 can then be used to determine the depth of the failure plane. LISEM uses a 2nd order polynomial solver to solve this equation. When the failure plane is found the process is repeated for the other cells which might have become unstable due to the slope failure in the current cell. This is repeated until there are no more unstable cells left. In the last step, all the modelled failure material is combined.

Debris flow equations

To model the debris flows and the interaction with floods, openLISEM uses a set of two-phase equations. The used equations are taken from Pudasaini (2012). The equations expand on the previously described dynamic wave equation (eq. 4.11 – 4.13) by adding viscous forces, non-Newtonian viscosity, two-phase drag and a Mohr-Coulomb type friction. Additional information about these equations, a more detailed description of the variables and the derivation can be found in Van den Bout et al. (2017) and Pudasaini (2012).

4.3.3 Model suitability

As stated before openLISEM was the only available model that met all the set requirements of this study. The new version of openLISEM is very promising, but it should be noted that this version has only been tested on one other location and is still in development.

There are several limitations of the model that should also be noted. OpenLISEM does not include evaporation. However, since the model is storm-based the amount of evaporation would be negligible. Regarding infiltration, the Green & Ampt model is a simplistic infiltration model, which disregards horizontal subsurface flow. Besides this, the infiltration model also treats the infiltration processes as linear. That said, a more complex infiltration model could not be used in this study due to insufficient data. Lastly, the storm-based approach of the model also makes it impossible to model long-term precipitation effects. Assuming the input rainfall events occur during the wet season, this could be solved by using higher initial soil moisture content values.

Altogether, the model seems suitable for modelling landslide and flood occurrences on St. Eustatius. The needed data input is feasible, even with the limited knowledge of the island, and the model does not make any assumptions that might have a large impact on the model results.

4.4 Model input

The following section describes how the data for the model input was collected and created. It first describes the used model scenarios and how the available data was processed to be used as model input. After this, the section gives a description of how new data was collected with the analysis of soil samples and in-situ measurements.

4.4.1 Model scenarios

To calculate the return period of the landslide and flood hazards on the island, the model was run with several scenarios. These scenarios consisted of design storms with different return periods, which could be used as a proxy for the return periods of the hazards. Since longer return periods seemed to underestimate the actual rainfall intensities (table 4.1), the scenarios were limited to a 10-year return period. A 50-year design storm was chosen to represent an extreme weather event, like a hurricane. The used return periods were:

- 1-year return period
- 5-year return period
- 10-year return period
- 50-year return period

4.4.2 Processing available data

OpenLISEM needs meteorological data, morphological data, land-use data, surface (soil) data, slope stability parameters, infiltration parameters and topographic data as input. The collection of this data from available data is described in the following section.

Meteorological data

OpenLISEM needs rainfall intensity (mm/h) data from a design storm as input. Meteorological data from St. Eustatius only contained daily precipitation values. It is possible to downscale this data to rainfall intensity data. However, reliable methods tend to be very complex and require large, historical, precipitation datasets (Marani and Zanetti, 2007). For this reason, an intensity duration frequency (IDF) curve from the US Virgin Island (Bonnin et al., 2008) was used to derive the hourly precipitation data. This IDF curve is shown in figure 4.3. Several design storms were constructed from this curve using the alternating block method. This was done for four different frequencies: 1 year, 5 years, 10 years, and 50 years (see also appendix C for the constructed design storms).

A comparison of the IDF data with the daily precipitation data maxima showed that the IDF data generally underestimates the yearly extremes on St. Eustatius (table 4.1). The higher daily precipitation data from St. Eustatius was probably caused by extreme precipitation events during hurricanes. The statistics used in the construction of the IDF curve might have subdued these extremities. It is however also important to note that the return periods of the daily precipitation data from Sint Maarten and St. Eustatius were constructed from a 30-year meteorological record (30 years, 1984-2015). The longer return periods based on this record are therefore not reliable.

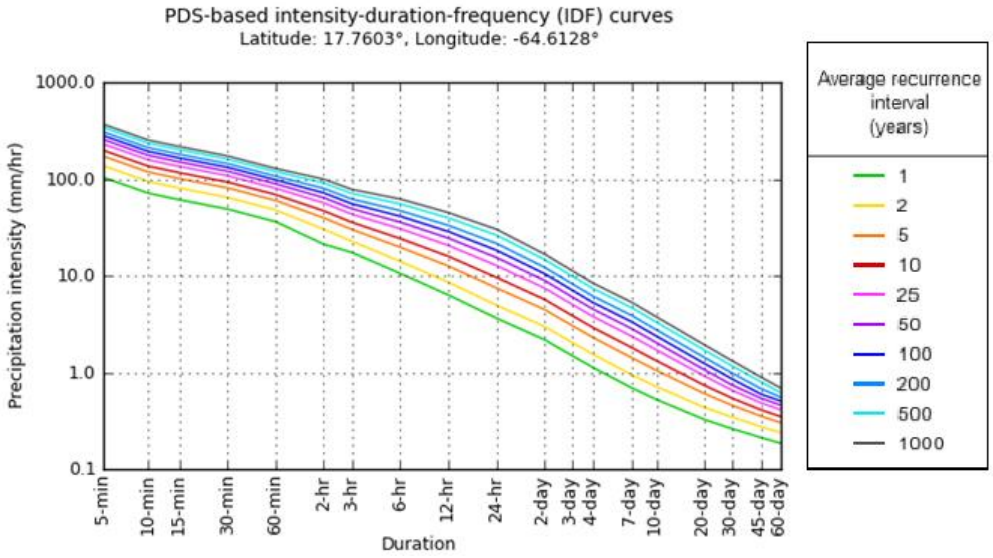

Figure 4.3: Precipitation Intensity Frequency curve of the Cotton Valley 2 station in the US Virgin Islands (Bonnin et al., 2008).

Table 4.1: Table of the comparison between the maximum cumulative daily precipitation values from the IDF dataset and a combined meteorological dataset (1984-2015) of Sint Eustatius (Statia) (MDC, 2017) and Sint Maarten (Menne et al., 2015).

Return period (yr)	IDF (mm)	Statia/Sint Maarten (mm)
1	87.7824	-13.71
2	119.4816	70.64601187
5	179.832	182.1585939
10	231.0384	266.5146058
25	307.2384	378.0271879
50	371.2464	462.3831998
100	441.96	546.7392116
200	519.3792	631.0952235
500	633.984	742.6078056
1000	725.424	826.9638175

Morphology Maps

The digital elevation model (DEM) was taken from (Mücher et al., 2014). This DEM was constructed from aerial photographs taken in 1991. A hillshade of the resulting DEM is shown in figure 4.4. The DEM has an x,y-resolution of 5m and the accuracy of the resolution in the z-direction is 60cm. However, due to insufficient ground control points and correlation difficulties caused by the vegetation density, the DEM shows some significant noise problems (Mücher et al., 2014). Especially on the eastern side at the foot of the Quill volcano (fig. 4.4). A solution to this problem was not found.

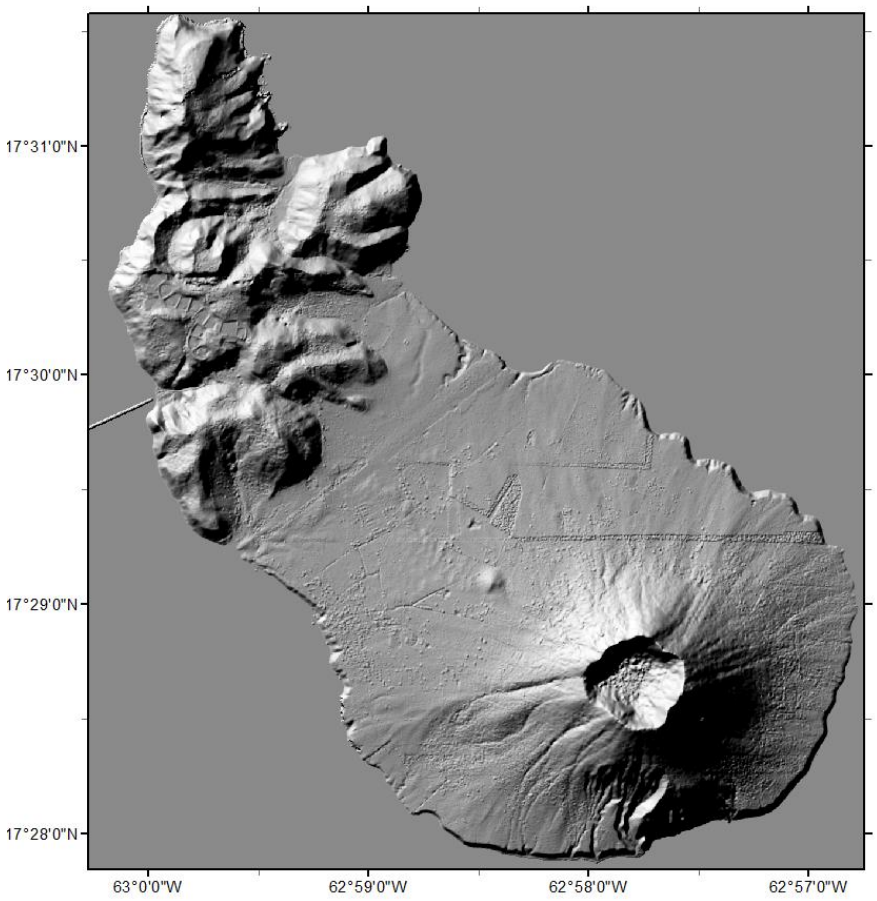

Figure 4.4: Hillshade of the DEM by Mücher et al. (2014).

The DEM was used to create several other maps that were needed as input for the model: a slope map, a local drain direction (LDD) map, an outlet map, a main outlet map and a watershed map. All these maps, except the slope map, were based on the LDD function from the PCRaster environment.

The local drainage direction gives for each cell the direction in which a substance would drain to another cell. A very important part of the LDD function in PCRaster is the pit removal. A pit is defined as a cell surrounded by neighbouring cells of higher elevation. However, sometimes these pits are created artificially by errors in the DEM and these have to be removed. As artificial pits are often much smaller than real pits, the artificial pits can easily be removed by setting pit size thresholds. This is incorporated in the PCRaster LDDcreate function, where the parameter values are commonly set to 1e8. In PCRaster you can also define if pits at the edges of the map will be included in the pit removal process (--lddout) or not (--lddin). For the LDD map used in this study, the LDD function was set to not include the pits at the edges in the removal process, as this would avoid accumulation of water at the coast of the island.

The outlet map and watershed map were both based on the LDD map that resulted from this. The main outlet point was assigned as the outlet of the largest catchment of the watershed map. The other outlet points were assigned as the pits in the LDD map.

Land-use data

The land-use map was based on an older land-use map created by Smith et al. (2013), shown in figure 4.5. This map was made using both satellite data from 18/02/2011 (Worldview-2, 2014) and ground control points. However, this map is missing a large portion of the island (fig. 4.5). For this study, these areas were filled up with the Worldview-2 satellite image from 2014 that was provided by TNO. The image was classified using a supervised classification based on human recognition. This was done for 11 classes (given in fig. 4.6). As the accuracy of this classification is expected to be lower, this new land-use classification was only used to fill in the gaps of the earlier land-use map from 2013. The result is shown in figure 4.6.

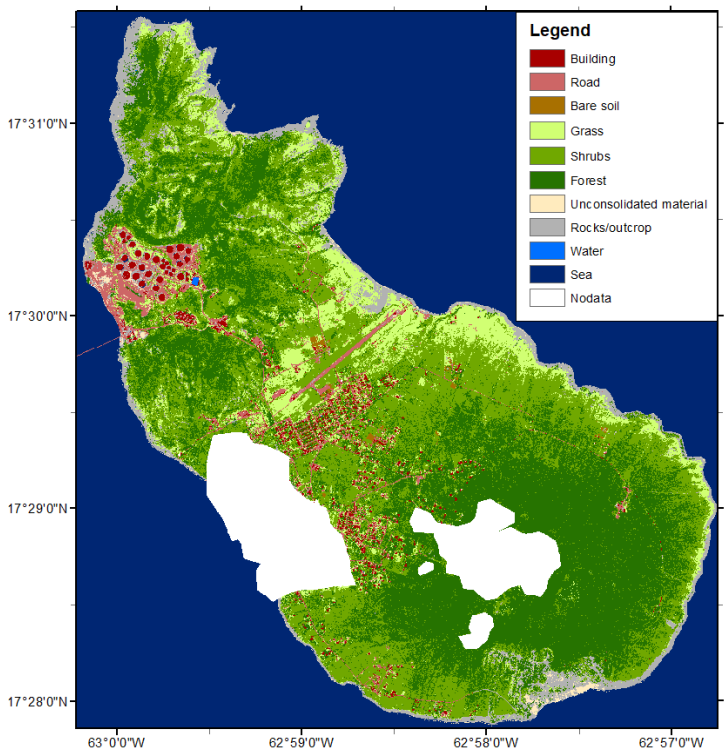

Figure 4.5: Old land-use map Smith et al. (2013).

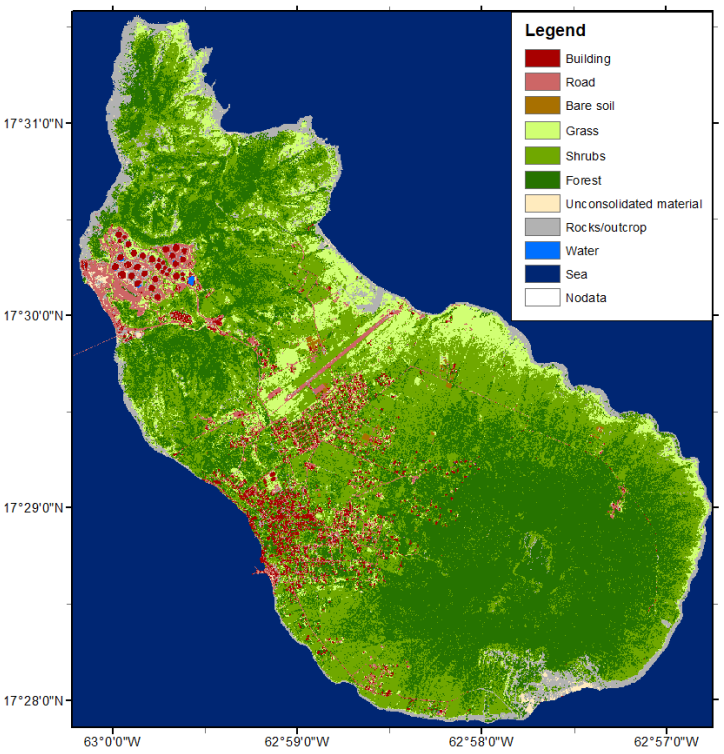

Figure 4.6: New land-use map based on the land-use map from Smith et al. (2013). Only the NoData values were changed.

Besides a land-use map, the needed land-use data also consisted of vegetation-related maps. The model needed a map of the leaf area index (LAI), vegetation cover and the vegetation height. The litter map (amount of organic litter underneath the canopy) and grass strips map, that could also be defined, were both set to a value of zero. The LAI was calculated from the enhanced vegetation index (EVI). Since Sint Eustatius has a very dense vegetation over the Quill volcano (fig. 4.8), the EVI was chosen over the normalized vegetation index (NDVI), because the NDVI tends to saturate at high biomass conditions and is very sensitive to soil background conditions (Huete et al., 2002 and Huete, 1988). The EVI was developed to optimize the signal over high biomass conditions by incorporating the blue band in the equation. Equation 4.17 by Huete et al. (2002) was used to calculate the EVI.

$$EVI = 2.5 * \frac{NIR2 - Red}{NIR2 + 6Red - 7.5Coastal + 1}, \tag{4.17}$$

where NIR2 is the intensity of the second near infrared band, Red the red band and Coastal the coastal blue band. The NIR2 was chosen over the NIR1 band, as it showed a better distinction between different vegetation densities. The coastal band was chosen over the blue band, as the window of this band lies closer to the blue band of the MODIS satellite with which the EVI formula was developed.

After the EVI was calculated the LAI was derived with equation 4.18 by Boegh et al. (2002).

$$LAI = 3.618 * EVI - 0.118 \quad (4.18)$$

The vegetation cover map was also based on the EVI. It was assumed that the maximum EVI value was representative for a vegetation cover of 100% and that an EVI of zero was equal to no vegetation cover. The values of the EVI map were linearly stretched from 0 to 1 to get the vegetation cover map.

Lastly, the vegetation height was taken from a study by De Freitas et al. (2012). This study provided a vegetation map for the island. The vegetation height map was created by assigning every vegetation class the average vegetation height of its class, taken from the data in the report by De Freitas et al. (2012).

Surface data

The surface data input needed several maps: surface roughness, mannings' n, stoniness, crustedness, compactness and hard surfaces. However, crustedness, compactness and hard surfaces were all ignored, and the values set to zero. The surface roughness and mannings' n were both derived from the land-use map, using tables with standard values for land-use classes (Chow, 1959; Jetten and Van den Bout, 2018).

The stoniness was defined as the ratio of the surface covered by stones or sediment larger than pebbles. This was noted at each location during the fieldwork (see section 4.4.3). In the model, the average value of these locations was used for the entire island.

Slope stability and debris flow data

For the slope stability and debris flow simulation, the model needed the following parameters as input: soil density, apparent soil cohesion, soil internal friction angle, rock fraction, rock size, soil depth and amount of debris material. The soil density, soil cohesion, soil internal friction angle, rock fraction and rock size were all determined during the fieldwork (see section 4.4.3).

The soil depth map was determined from the DEM (fig. 4.7). Several studies (Tesfa et al., 2009; Saulnier et al., 1997; Schilirò et al., 2015) have shown that this is possible and can give reliable results. One of the most commonly used models for estimating soil depth from topographic characteristics was proposed by Saulnier et al. (1997). The model uses equation 4.19.

$$h_i = h_{max}\left\{1 - \left[\frac{tan\ \alpha_i - tan\ \alpha_{min}}{tan\ \alpha_{max} - tan\ \alpha_{min}}\left(1 - \frac{h_{min}}{h_{max}}\right)\right]\right\}, \quad (4.19)$$

where h_i is the soil depth at the current pixel, h_{max} and h_{min} are respectively the maximum and minimum soil depth of the area, α_i is the slope angle of the current cell and α_{max} and α_{min} are respectively the maximum and minimum slope angle of the area.

This model is very basic, based solely on the slope angle and maximum and minimum depth of the area, but it is commonly used when soil depth needs to be estimated (Schilirò et al., 2015 and Salciarini et al., 2006). However, as Tesfa et al. (2009) showed, slope curvature is an even more determining factor for the soil depth than slope angle. In this study, the curvature of the slope was therefore also incorporated in the soil depth prediction model (eq. 4.20).

$$h_i = h_{max} + \frac{h_{max} - h_{min}}{\tan \alpha_{min} - tan\ \alpha_{max}} * \tan \alpha_i + b * curv_i\ , \quad (4.20)$$

where b is a parameter and $curv_i$ is the slope curvature in the current cell.

The minimum soil depth was set to a value of 0.01, because openLISEM cannot deal with a soil depth of 0.0. The values of parameters b and h_{max} were determined by solving the equation for several locations where the soil depth was determined in the field. The resulting values were 6.5 for the maximum soil depth and a value of 3 for parameter b. The amount of potential debris material was set to the soil depth.

Infiltration properties

Since the Green and Ampt method was chosen for modelling the infiltration, openLISEM needed the saturated hydraulic conductivity (K_{sat}), suction at the wetting front (ψ), the initial moisture content (θ_{ini}), the porosity (ϕ) and the depth of the soil layer as input for the infiltration model. Only the θ_{ini} was measured directly in the field. The depth of the soil layer was set to the soil depth. The other variables were estimated with pedotransfer functions from the grain-size distribution of the soils. This is explained in more detail in sections 4.4.3 and 4.4.4.

Topographic data

OpenLISEM also needed topographic data as input. The roads and buildings on the island were assumed to be impermeable surfaces in openLISEM. This data was derived from OpenStreetMap (OSM) data (fig. 4.7). The data was used to calculate the density of the buildings and the road width.

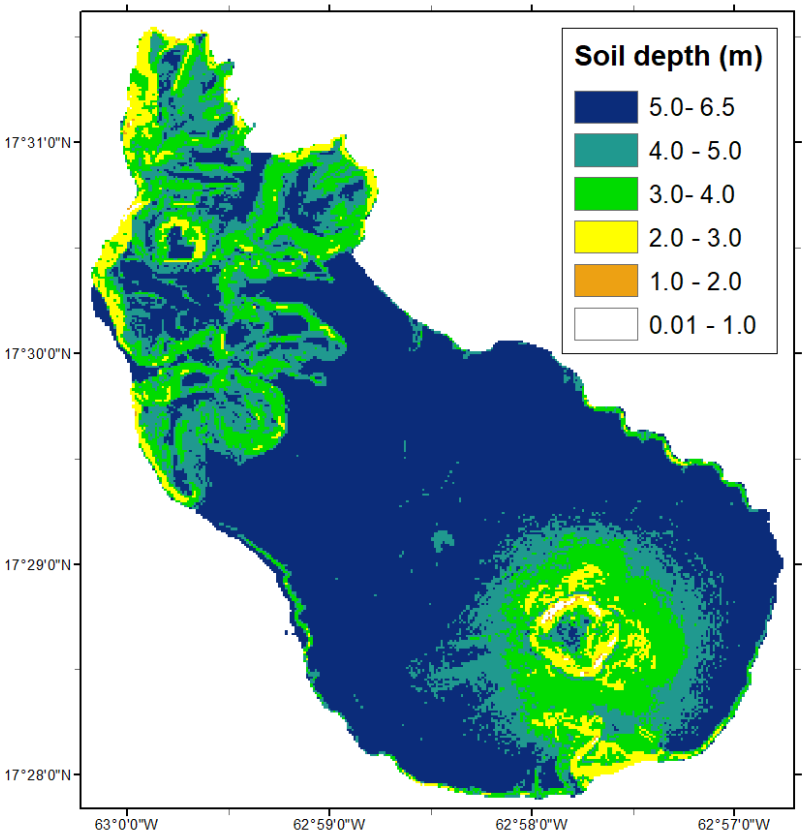

Figure 4.7: Map of the soil depth as calculated with the model in eq. 4.20.

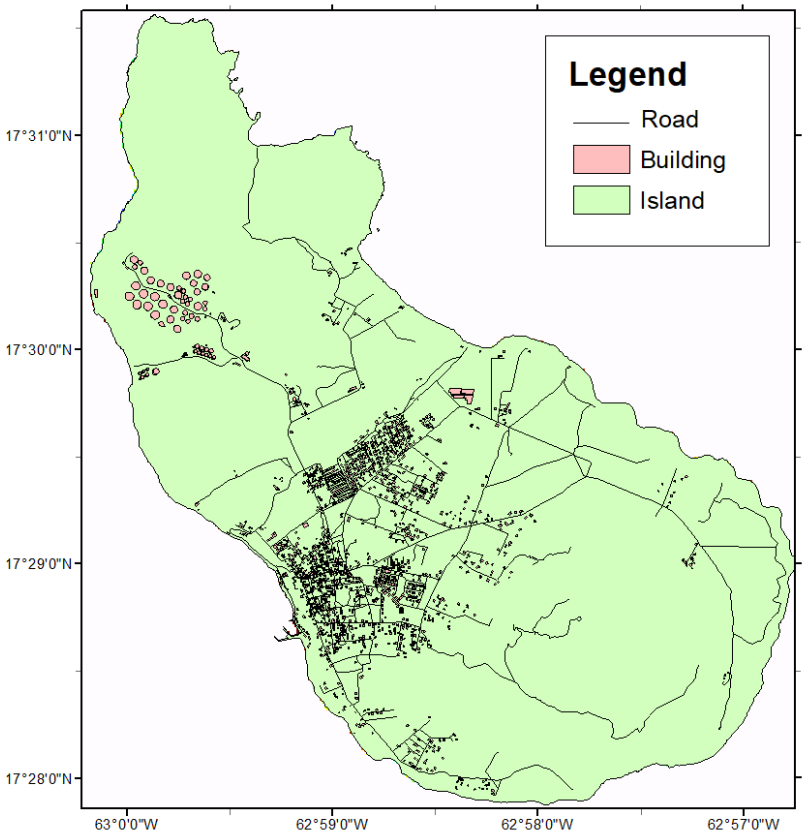

Figure 4.8: Map of the Elements at risk taken from the OSM contributors (2017).

4.4.3 Field measurements

Several parameters that were needed as input of the model had to be collected in the field. The reason for this was either lack of information or outdated information. The study by Augustinus et al. from 1985 was the only study providing soil data of St. Eustatius.

The needed data was therefore collected during the fieldwork on St. Eustatius in June 2017. During the fieldwork, the stoniness, rock size and grain-size of the soil were written down at every visited location and the cohesion and initial moisture content were measured at almost every location (see fig. 4.9 and appendix D for a detailed list). Due to time constraints, the Northern Hills of the island were not visited extensively.

The cohesion was measured using both a small torvane and a pocket-sized penetrometer. Both instruments were used, as they both have their limitations (Zimbone et al., 1996). Besides this, a combination of the results from both instruments was assumed to give a more accurate indication of the actual cohesion of the soil.

The in-situ soil moisture content was measured using a Theta-probe sensor. This sensor measures the soil moisture content by relating it to the dielectric permittivity of the soil. Since water has a higher dielectric permittivity than dry soil, a higher dielectric permittivity of the soil indicates a higher soil moisture content. To verify, the theta-probe results were compared with the soil moisture content determined by oven-drying soil samples.

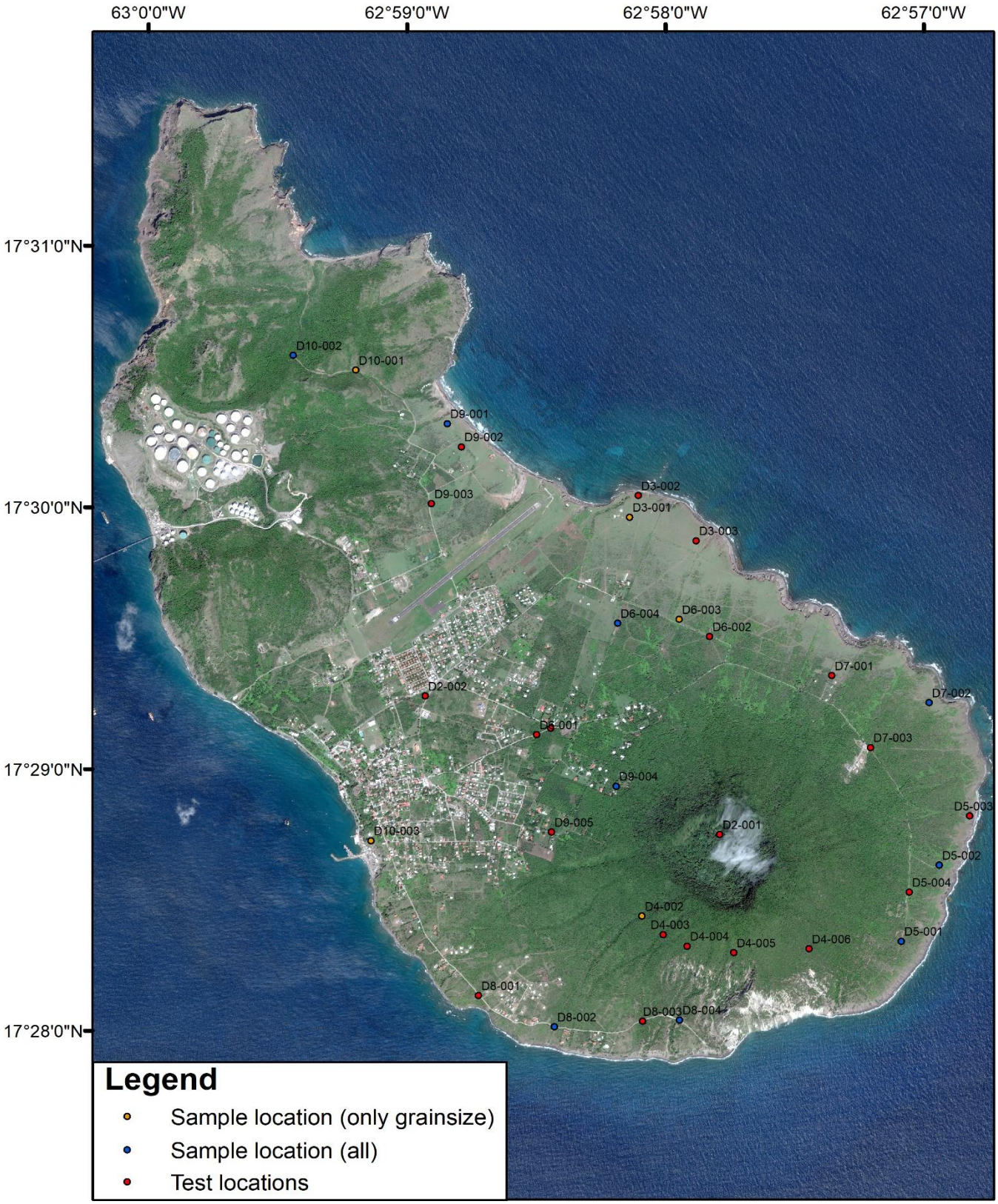

Figure 4.9: Map of the fieldwork locations. Orange indicates samples were taken, but they could not be used for the determination of the dry bulk density. Blue indicates that samples were taken that could be used for every sample analysis. Red indicates that only measurements or notes were taken at the locations. Background sat. image: Worldview-2 (2014).

4.4.4 Sample analysis

Besides in-situ measurements, the fieldwork also provided additional data for the model input by analysing taken soil samples. These soil samples were collected with a 5 cm Kopecky ring. Sampling locations are shown in figure 4.9. The soil samples were analysed in two steps, first in the small lab of the CNSI (Caribbean Netherlands Science Institute) research centre on St. Eustatius and later in the sediment laboratory of the VU (Vrije Universiteit).

The goal of the sample analysis in the lab on St. Eustatius was to get the grain-size distribution, the dry bulk density and soil moisture content of the soil. This was achieved by weighing the samples, drying them in an oven and sieving them.

The definition of the dry bulk density is the density of the dried soil when there is no more water in the soil (eq. 4.21).

$$\rho_b = \frac{M_{solid}}{V_{total}}, \tag{4.21}$$

where ρ_b is the dry bulk density (g/cm^3), M_{solid} the mass of the solid part of the soil (gr) and V_{total} is the total volume of the soil (cm^3). The total volume of the soil was a fixed value for every sample that was taken, i.e. the volume of the sampling ring. However, as some of the samples did not completely fill the sampling ring due to the loose soil on St. Eustatius, they could not be used to determine the dry bulk density of the soil. Appendix D gives a detailed list of which samples were used for determining the dry bulk density.

To get the mass of the solid part, the samples were put in the oven at 85°C for 24 hours, to evaporate the water out of the soil. After the samples were taken out of the oven and had cooled down, they were weighed with their sample ring and then only the sample rings were weighed. The mass of the solid part could then be derived from the mass of the dried soil inside the ring minus the mass of the used ring (eq. 4.22).

$$M_{solid} = M_{dry,with\,ring} - M_{ring}\ , \tag{4.22}$$

where $M_{dry,with\,ring}$ is the weight of the dried soil plus sample ring and M_{ring} the weight of the sample ring.

To get the soil moisture content of the samples, the weight of the samples before drying was subtracted by the weight of the soils after drying. The resulting weight then gives the amount of water in grams that was inside the soil. As soil moisture content is normally given as a ratio, this weight should be divided by the weight of the dried soil (see also the eq. 4.23).

$$\theta = \frac{M_{water}}{M_{soil,dry}} = \frac{M_{soil,wet} - M_{soil,dry}}{M_{soil,dry}}, \quad (4.23)$$

where θ is the soil moisture content (-), M_{water} the weight of the water content, $M_{soil,dry}$ the weight of the dried soil (with sample ring) and $M_{soil,wet}$ the weight of the soil before drying (with sample ring). Since the calculation of the soil moisture content does not assume any volume of the soil, all the taken samples could be used.

Not all the needed infiltration parameters for the model could be measured in the field. The saturated hydraulic conductivity, porosity and matric suction were estimated with pedotransfer functions. The pedotransfer functions used in this study were taken from Saxton and Rawls (2006) (see appendix E for the equations). A study by Gijsman et al. (2002) reviewed 8 methods for estimating soil water retention parameters and concluded that the method by Saxton et al. (1986) performed best for their control group. The method described in Saxton and Rawls (2006) builds upon the previous method from Saxton et al. (1986).

The pedotransfer functions in Saxton and Rawls (2006) need the organic matter content (OM), percentage of clay, percentage of silt and percentage of sand as input. The amount of OM in the soil of St. Eustatius was taken from the study by Augustinus et al. (1985), as the oven in the lab on St. Eustatius could not be used for measuring the organic matter content with loss on ignition. The percentage of sand in the soil was measured in the lab on St. Eustatius using sieves. The used sieves ranged from 63 µm to 710µm in mesh size.

Normally, the silt and clay content of soil samples are determined using sedimentation methods (Gee and Bauder, 1986). However, a major disadvantage of these methods is that they make an assumption about the density of the grains inside the soil (Di Stefano et al., 2010). Since the calibrations of these methods are mainly based on quartz sands, the assumed density is much lower than the density of the soils on St. Eustatius that are of volcanic origin. Use of this method would thus overestimate the grain sizes inside the soil samples.

Instead, a laser diffraction method was used to determine the silt and clay content of the soil. This method does not assume a density of the grains inside the soil and is, therefore, better suited for this study. The laser diffraction method has, however, not been standardized inside the field of sedimentology and several studies have shown that laser diffraction underestimates the clay content and overestimates the silt content when compared to sedimentation methods (Eshel et al., 2004; Di Stefano et al., 2010). For this reason, the grain-size distribution results from both the laser diffraction, sieving method and the study by Augustinus et al. (1985) were compared with each other to see how

well the laser diffraction method performed. This comparison is shown in the Results chapter of this report.

Before the samples could go into the laser diffraction machine, they had to go through several steps of preparation. This was done to remove the organic material from the soil and to detach the clay particles and grains from each other. The organic material was removed by adding a 5 ml solution of 30% H_2O_2 and waiting until the reaction has stopped. The grains were separated from each other by adding a 10ml solution of 10% HCl. This removed the $CaCO_3$ from the solution, which binds the grains. Lastly, the clay particles were separated from each other by adding $Na_4P_2O_7$.

A detailed overview of all the collected data during fieldwork and the results of the sample analysis can be found in appendix D.

Chapter 5 Results

This chapter presents the results of the hazard inventory mapping, the sample and measurement analysis, the model calibration, the landslide and flood modelling, and the hazard mapping. The hazard inventory will be presented first, then the field sample and measurement analysis, then the model calibration with a sensitivity analysis and lastly the results from the model runs.

5.1 Hazard inventory map

The information on the occurrence of previous landslides on the island was recorded during a fieldwork. This next section presents the observations and the final landslide inventory map. As discussed before, there was no data collected on the occurrence of flood hazards.

5.1.1 Field observations

During the fieldwork, it became clear that the landslide problem on the island was very limited and local. The occurrences of landslides seem to be focused around the cliffs at the coast and around the main volcano, the Quill. The coast of the island consists of cliffs that see a very high erosion rate. This can be concluded from the high occurrence of large gullies as shown in figures 5.2 and 5.3. Figure 5.3 also shows that these gullies are often very unstable and show many signs of landslide activity, like freshly exposed rocks and debris at the mouth of the gullies. On top of the cliffs, there are also many signs of erosions, as shown in figure 5.1.

Figure 5.1: Signs of erosion on top of the cliffs.

Figure 5.2: Gully erosion of coastal cliff, located at 17°30.011' N 062°58.310' W.

Figure 5.3: Signs of active erosion at the coastal cliffs. Debris has been deposited at the foot and the rocks of the cliff are freshly exposed.

The south-western part of the island, near White Wall, shows signs of several historic landslides originating from the slopes of the Quill. This was also confirmed by several inhabitants. See also fig. 5.4, 5.5, 5.6 and 5.7.

Figure 5.4: Possible toe of an old landslide, located at 17°28.040' N 062°57.945' W.

Figure 5.5: Signs of slope activity in the South-West.

The testimonies of the inhabitants also told that the road indicated in figure 5.7 has been covered by several historic landslides. However, the road does not form an important connection and only leads to a viewpoint at the southern end of the island.

Figure 5.6: Very active area for landsliding, many old landslides, located near White Wall.

Figure 5.7: Left-overs from a recent landslide that occurred in November 2016 and covered the entire road.

The visited location where the occurrence of landslides seemed to pose the highest risk to the community of St. Eustatius, was the bay area underneath the cliffs in the west. The erosion rate on this side of the island is much lower, but the entire harbour is built underneath these cliffs. Besides this, the water factory and electricity plant are also located here (fig. 5.8). A failure of the cliffs at this location could thus lead to both a power outage and loss of a connection to clean water for the island.

Figure 5.8: One of the buildings of the water factory (Merkman, n.d.).

There have already been several landslides from these cliffs in the past. A survey around the area showed mud marks on a wall of an old petrol station from a debris flow in November 2016 (fig. 5.9), the same day as the landslide in figure 5.7. The mud marks on the wall were about 1 meter high. The debris flow originated from the cliffs above the old petrol station (fig. 5.10) and blocked the main road of the harbour.

Figure 5.9: Mud marks on the wall of an old petrol station in the harbour area. Mud marks originate from a landslide that happened in November 2016. Marks reached up to a meter high.

Figure 5.10: Cliffside where debris flow from fig. 5.9 originated.

Further down the harbour near the location of the water factory and electrical plant, there were also signs of active rockfalls. The small wall in figure 5.11 shows a hole created by a large boulder that fell from the cliffs. Figure 5.12 shows how the boulder even bent the metal of the reinforced concrete.

Figure 5.11: Small wall in the harbour area with a hole created by a boulder that fell from the cliffs.

Figure 5.12: Metal of reinforced concrete bent by a boulder that fell from the cliffs in the harbour area.

5.1.2 Landslide inventory map

The resulting landslide inventory map of the field observations is shown in figure 5.13. The map shows that landslides mainly occur at the coastal cliffs, on the eastern side and western side of the island. A third cluster of historical landslides lies on the southern side of the Quill volcano. This cluster is located near the White Wall formation. Figure 5.6 also shows that this area experiences a high frequency of landslide occurrences. The landslides at the petrol station (Figure 5.9) and in Figure 5.7 were both triggered by heavy rainfall in November 2016. The triggers for the other landslides could not be determined since the timing of these landslides was not known.

It should be noted that this map is only an initial presentation of the historical landslides that occurred on St. Eustatius. Only a few landslide deposits were visited during the fieldwork (fig. 5.13).

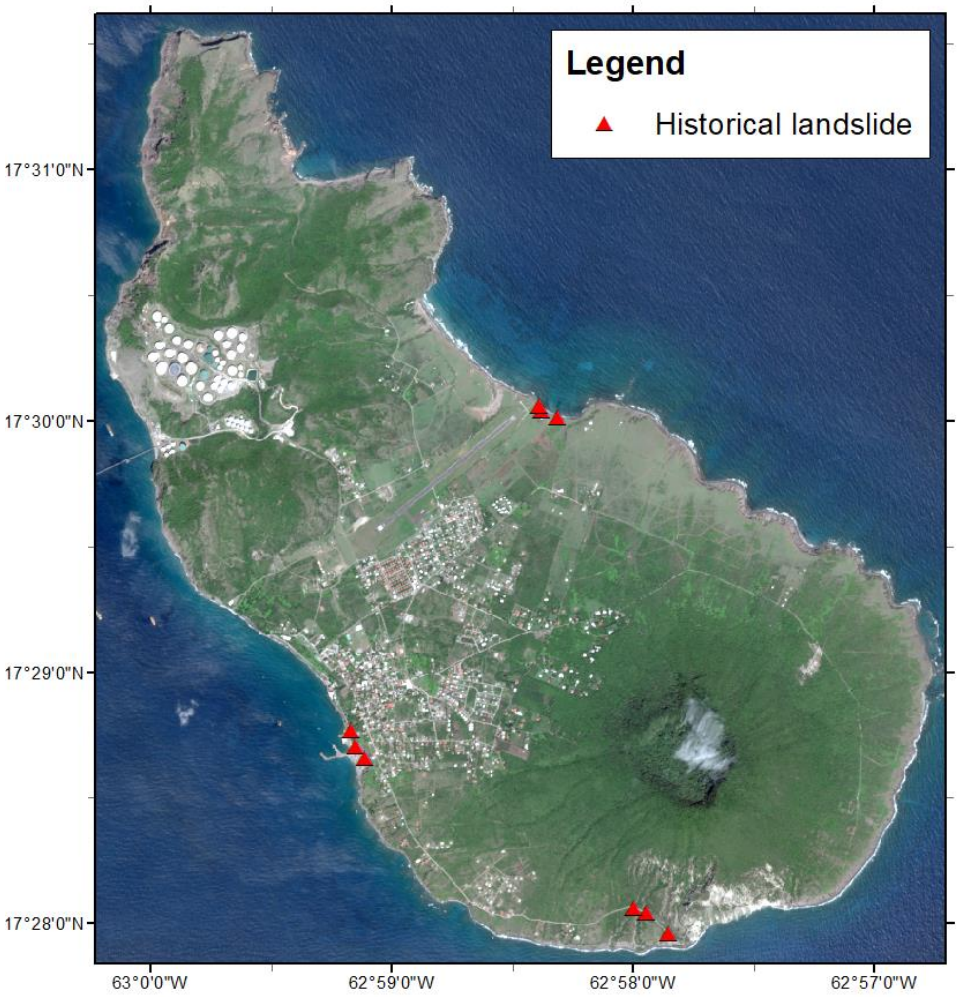

Figure 5.13: Landslide inventory map constructed from the field observations.

5.2 Sample and measurement analysis

The following section presents the results from the sample analysis and soil measurements. A detailed list of all the visited locations and results is given in appendix D.

The results of the torvane and penetrometer tests are shown in figure 5.14. Only the data measured with the torvane was used as input for the model. This decision was based on the fact, that the measurements from the penetrometer showed a much higher standard deviation (fig. 5.14). Besides this, the soil at the sample locations was often either too compacted or too loose to test for the cohesion with the penetrometer. The graph in figure 5.14 therefore only shows the results from the test locations where both methods could be used.

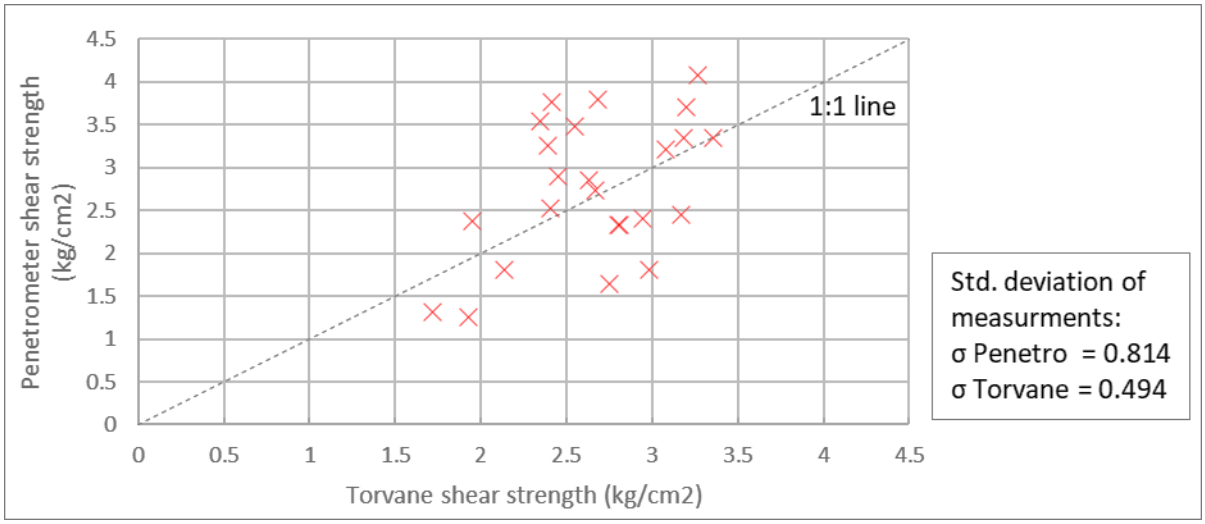

Figure 5.14: Comparison of the shear strength measured with the penetrometer and torvane. The standard deviations of the measurements are given in the textbox.

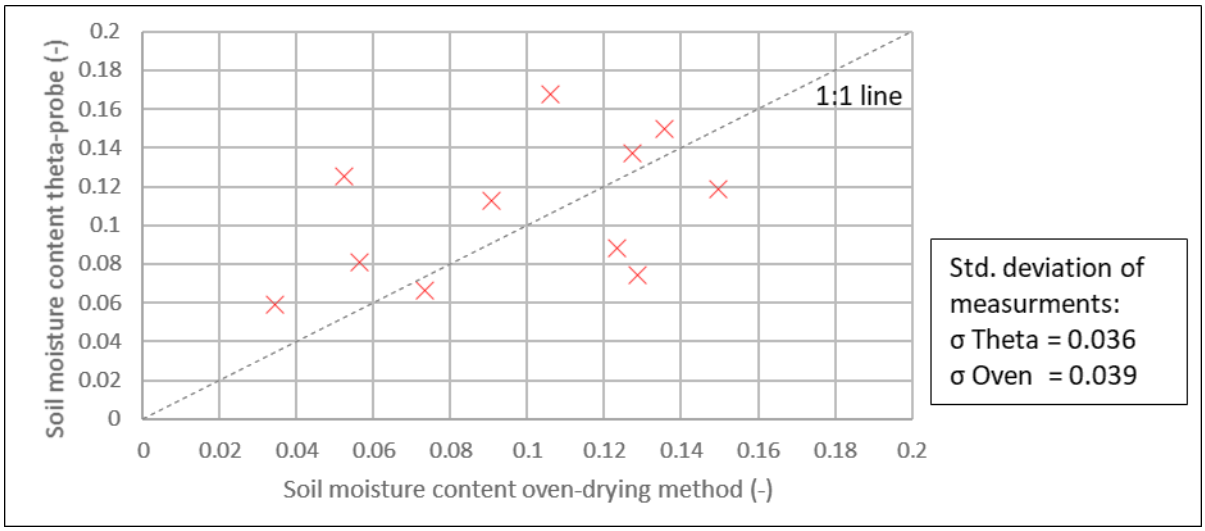

Figure 5.15: Comparison of the measured soil moisture content with the oven-drying method and the theta-probe. The standard deviation of both methods is also given.

A comparison of the results from the soil moisture content measurements is shown in figure 5.15. The figure shows that the values determined the theta-probe are generally higher than the soil moisture content measured using the oven-drying method. Besides this, the results also show that the fieldwork area was very dry during the field visit. Since the average measured soil moisture content of both methods lies around 0.1, the found standard deviations around 0.04 are reasonably high (fig. 5.15).

Figure 5.16 shows the results from the laser diffraction analysis of the taken soil samples. The results of the sieving method are shown in table 5.1. The grain-size distribution results from the sieving method, the laser diffraction method and the results from the study by Augustinus et al. (1985) were also compared to each other (table 5.1). This comparison shows that the grain-size distribution using

the sieving and laser diffraction methods are quite similar. The comparison with the results from the study by Augustinus et al. (1985) shows some large differences, especially below the 500µm grain-size. However, this could be attributed to the fact that Augustinus et al. (1985) took more samples from the Northern Hills were the soil is much finer, as can also be seen in figure 5.16 (sample d10-001).

Table 5.1: Comparison of the grain-size distribution results from the sieving analysis, the laser diffraction analysis and the study by Augustinus et al. (1985).

	Sieving	*Laser*	*Augustinus et al.*
> 710 µm	0.319407	0.398665	0.387933
710-500 µm	0.078163	0.097003	0.073558
500-125 µm	0.343984	0.293657	0.148826
125-63 µm	0.139554	0.06409	0.037645
< 63 µm	0.087868	0.146601	0.352039

The laser diffraction results were used as input for the silt, sand and clay fraction in the pedotransfer functions. They were deemed more reliable than the results from the other methods as they did not rely on interpolation between the data points due to the more detailed analysis. The results from the pedotransfer functions can be seen in table 5.2. The actual input of these variables was changed according to the model calibration.

Table 5.2: Results from the pedotransfer functions.

Porosity (-)*:	0.6266
Ksat (mm/h):	325.865
Matric pressure (cm):**	10.426

**Porosity was as assumed to be equal to the saturated moisture content*
*** At $\vartheta_{ini} = 0.95$*(porosity), since the measured ϑ_{ini} of 0.115 gave matric pressures that were too high.*

The number of taken samples and measurements was not large enough to create a spatial distribution of the needed model inputs. For this reason, the decision was made to assign one uniform value to the entire island for the input parameters that were measured in the field. This uniform value was created by taking the average of the measurements.

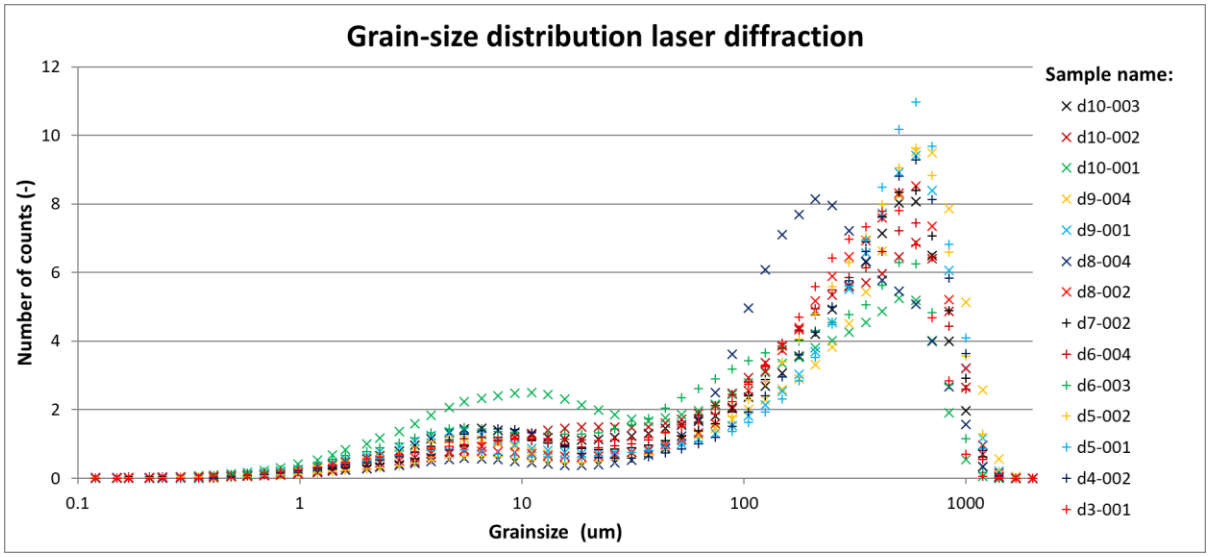

Figure 5.16: Grain-size distribution from the laser diffraction analysis.

5.3 Calibration and Model sensitivity

The calibration of the model was performed by first analysing the sensitivity of the model, to understand which variables had the biggest impact on the model. After the sensitivity was analysed, the model was calibrated based on the results of the sensitivity analysis and using the 5-year design storm.

5.3.1 Sensitivity analysis

The sensitivity analysis was performed by changing the multiplication factors and values of the variables affecting slope failure in the model (table 5.3). These variables were all changed independently. The results showed that the cohesion, internal friction angle, soil depth and initial soil moisture content were the variables with the largest impact on the model results. The hydrographs of these results are shown in figures 5.17 – 5.20 (see appendix F for results of the other variables). All model runs showed that the initiation and magnitude of slope failure coincided with the extreme peaks in the hydrographs. For this reason, the hydrographs were used to estimate the modelled initiation and magnitude of slope failure during this study.

Table 5.3: Settings for the sensitivity analysis.

Variable:	Used multiplication factors and values:
Saturated hydraulic conductivity	0.01, 0.10, 0.50, 1.00
Initial moisture content	0.50, 0.75, 1.00
Soil cohesion	1.00, 5.00, 10.00, 20.00
Internal friction angle	1.00, 1.10, 1.20, 1.30, 1.40
Soil depth	0.50, 0.75, 1.00, 1.50, 2.00
Maximum Safety factor (-) (0.90)*	0.70, 0.80, 0.90, 1.00
Resulting Safety factor (-) (1.30)*	1.10, 1.20, 1.30, 1.40
Minimum debris height (m) (0.10)*	0.00, 0.10, 0.50
* Instead of multiplying the original values, the values were changed directly. These were also the variables that had a different standard value than 1.00. Their standard values are given in brackets.	

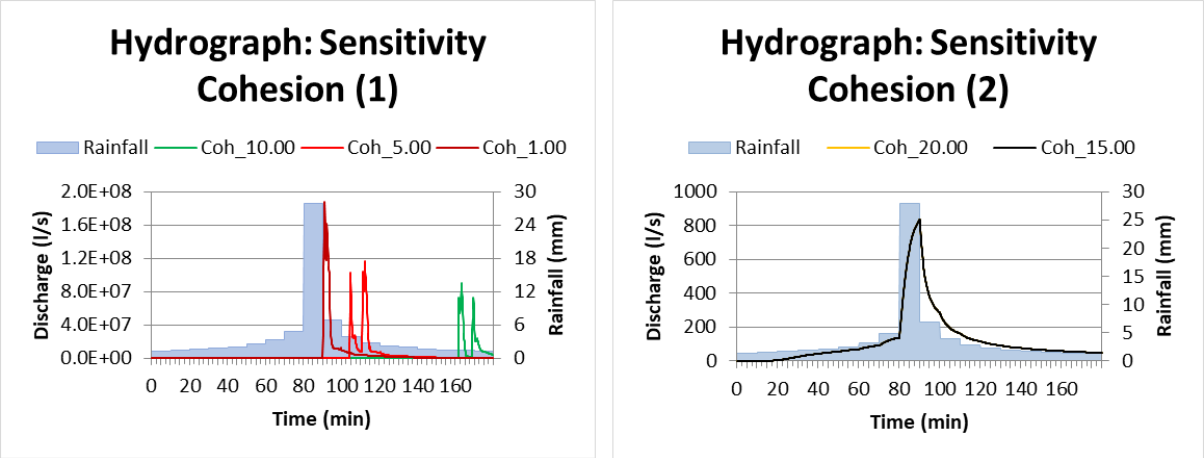

Figure 5.17: Hydrographs showing precipitation and overland flow discharge of the sensitivity analysis with cohesion. Left: cohesion times 1.00-10.00 and right: cohesion times 20.00 & 15.00.

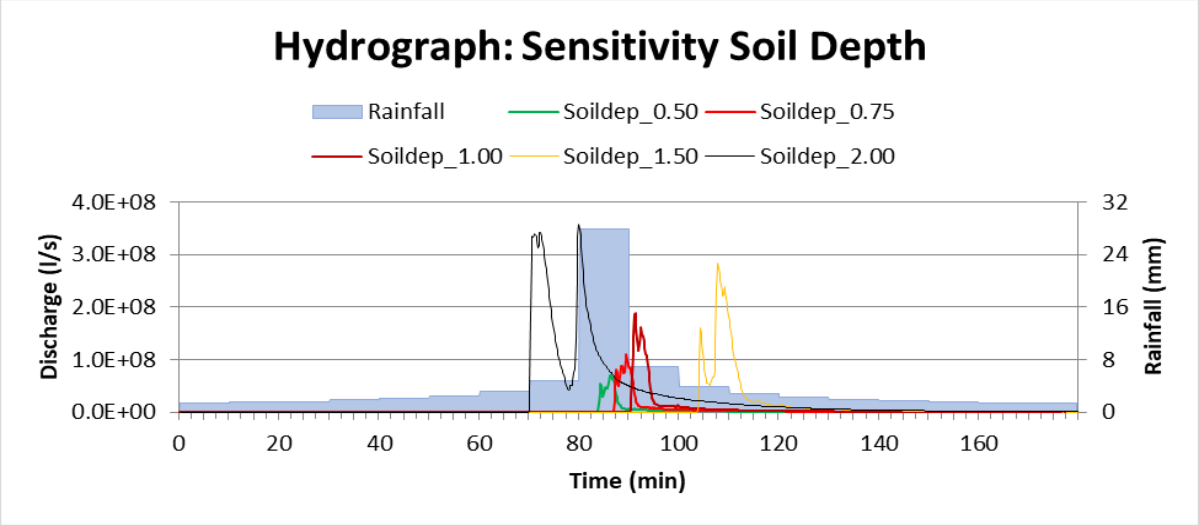

Figure 5.18: Hydrograph showing precipitation and overland flow discharge of the results of the sensitivity analysis with a soil depth times 0.50-2.00.

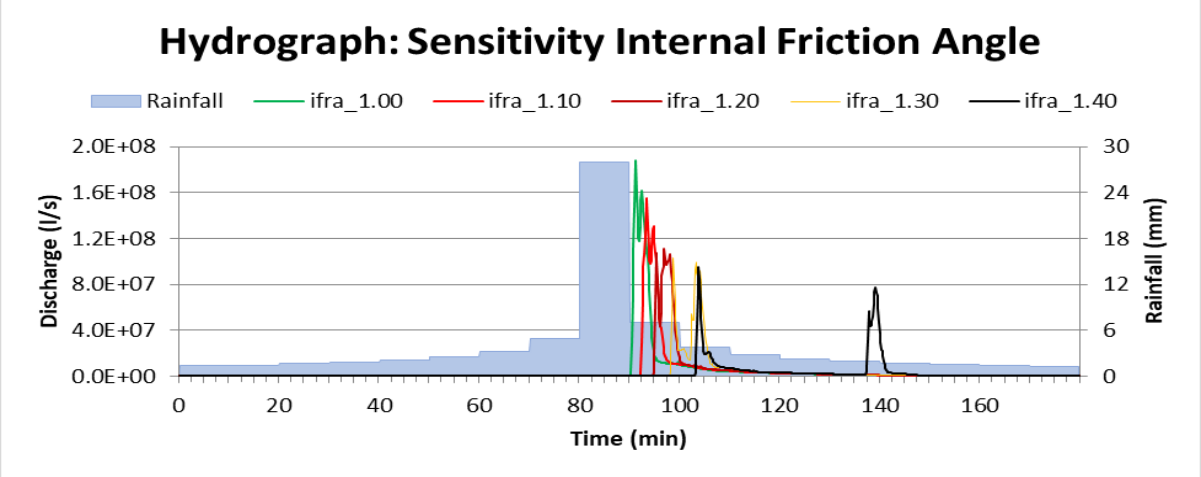

Figure 5.19: Hydrographs showing precipitation and overland flow discharge of the results of the sensitivity analysis with the internal friction angle times 1.00-1.40.

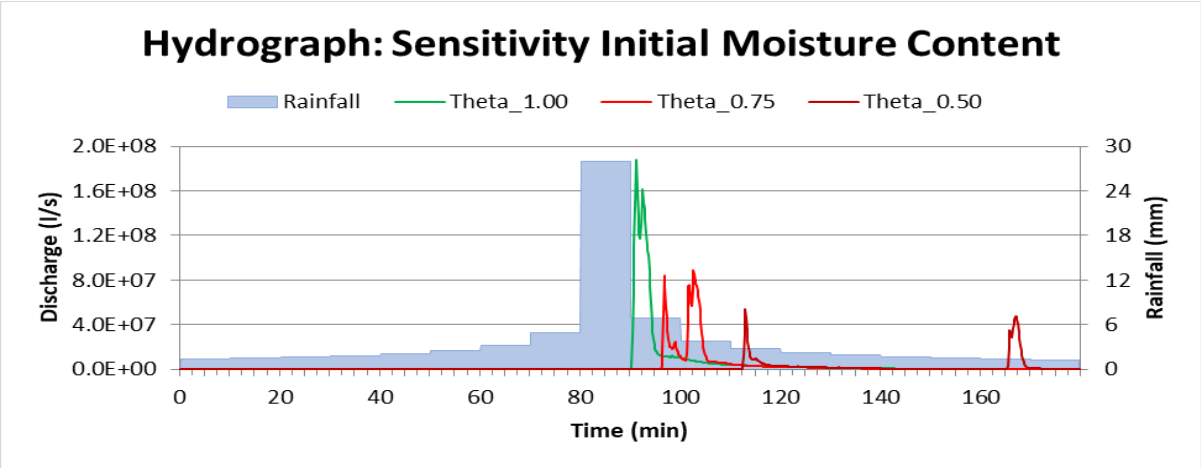

Figure 5.20: Hydrographs showing precipitation and overland flow discharge of the results of the sensitivity analysis with the initial moisture content times 0.50-1.00.

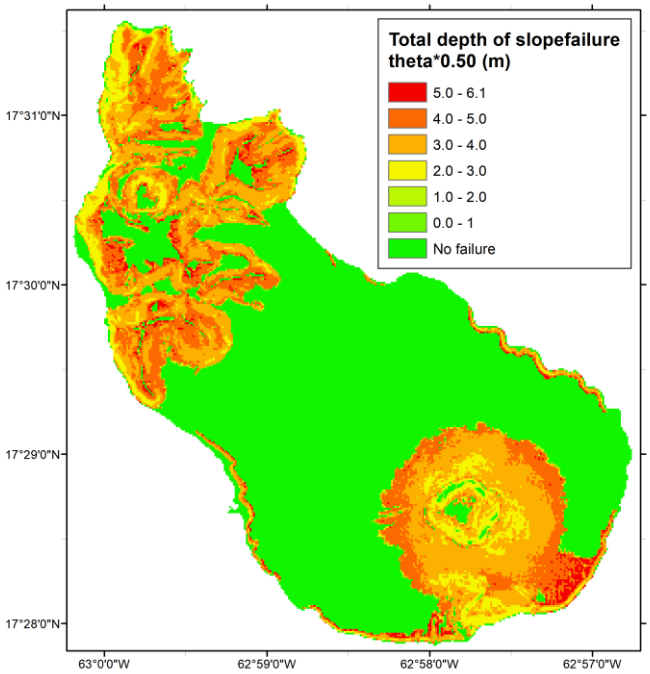

Figure 5.21: Map result of slope failure depth for the sensitivity analysis with initial soil moisture content times 0.50.

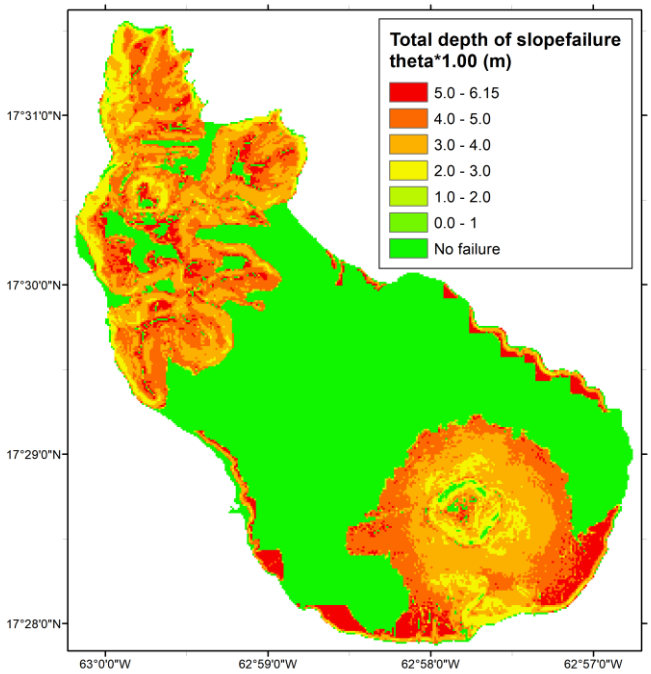

Figure 5.22: Map result of slope failure depth for the sensitivity analysis with initial soil moisture content times 1.00.

The areas of slope failure occurrence stay roughly the same with changes in the variables. The differences in spatial distribution are still very little when the results from the analysis with initial soil moisture content, the variable with the highest sensitivity, are compared (figures 5.21 and 5.22). The timing of slope failure is however very sensitive to changes in the variables, as can also be seen in hydrographs above (figures 5.17 – 5.20). For some variables, the delay between the two peaks in the hydrographs also changed. The two peaks represent a failure of the northern and southern part of the island. In other words, the delay represents the difference between the slope failure initiation in the northern part and the southern part. In most of the model runs, the northern part of the island failed before the southern part. However, the runs with a cohesion times 10.00 and a soil depth times 2.00 resulted in failure initiating in the south first.

When the effects of the different variables are studied, the soil depth and initial moisture content seem to have the largest effect on the model results. The soil depth influences the amount of slope failure positively, an increase in soil depth leads to an increase in slope failure. The timing of the slope failure is also changed with soil depth. However, this change is not purely consistent. It appears that a threshold is passed between 1.50 and 2.00 times the soil depth. After 1.50 times the soil depth, the timing is influenced negatively by an increase in soil depth. The initial soil moisture content influences the amount of slope failure positively as well, an increase of initial moisture content leads to an

increase in slope failure. Besides this, an increase also influences the timing of slope failure positively and the delay between the two peaks negatively.

The cohesion and internal friction angle of the soil also showed a high sensitivity. In general, an increase of the cohesion leads to a decrease in the amount of slope failure and a delay in the timing of slope failure. When changing the cohesion, the results also showed a threshold that was passed after multiplying the cohesion by 10.00, as the results do not show any failure with a multiplication of 15.00 and 20.00 (fig. 5.17). Increasing the internal friction angle results in less slope failure and a delay in the timing of the slope failure. Besides this, an increase also results in an increasing delay between the two peaks of the hydrograph.

5.3.2 Model calibration

After the sensitivity analysis was finished, the model was calibrated. This was done using a trial and error method. The most influential variables were changed first while changing them as little as possible. Since there was no historic landslide database, it was not possible to validate the results of the calibration. Therefore, the goal was set to minimize the amount of slope failure as best as possible for the 5-year storm. However, the aim was to have at least one landslide on the western side of the Quill volcano, since the landslide inventory showed that this was the location with the highest landslide occurrence. The result of the final calibration is shown in the section of the model scenario results with a 5-year return period (figures 5.26 – 5.30). The calibrated parameters are shown in table 5.4.

*Table 5.4: Used settings for the model scenario runs, *indicates the value of the variable was changed, not the multiplication.*

Variable:	***Used multiplication factors and values:***
Saturated hydraulic conductivity	1.00
Initial moisture content	0.90
Soil cohesion	10.25
Internal friction angle	1.10
Soil depth	0.75
Maximum Safety factor (-) (0.90)*	0.90
Resulting Safety factor (-) (1.30)*	1.30
Minimum debris height (m) (0.10)*	0.10
***** Instead of multiplying the original values, the values were changed directly. These were also the variables that had a different standard value than 1.00. Their standard values are given in brackets.	

5.4 Landslide and flood modelling

The model was run using four design storm scenarios, which represented the return periods of the modelled hazards: a 1-year return period, 5-year return period, 10-year return period and a 50-year return period. The results of these model scenarios are presented below.

5.4.1 1-year return period

The 1-year design storm did not result in any failures (fig. 5.23). The resulting hydrograph is shown in figure 5.24. This hydrograph represents the total runoff from the island, so the accumulative discharge of every outflow point from the island (this applies to every hydrograph that is shown in this chapter). The peak discharge of 445.138 l/s is reached at 90 minutes into the storm. This peak is not high enough for the development of significant runoff as can be seen in figure 5.25. This map of the maximum water height shows that water collects on the oil drums in the north, on the inside of the volcano rim and at the coast.

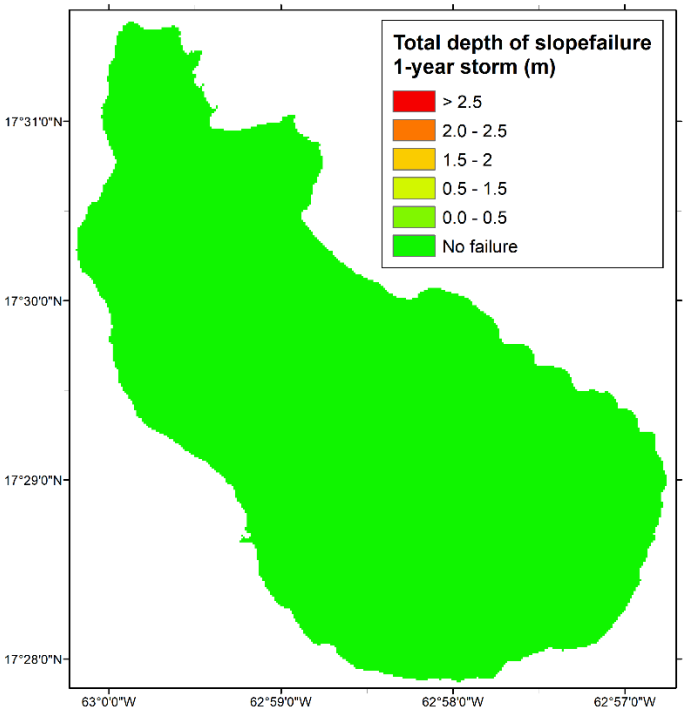

Figure 5.23: Total slope failure map result with the 1-year design storm scenario run.

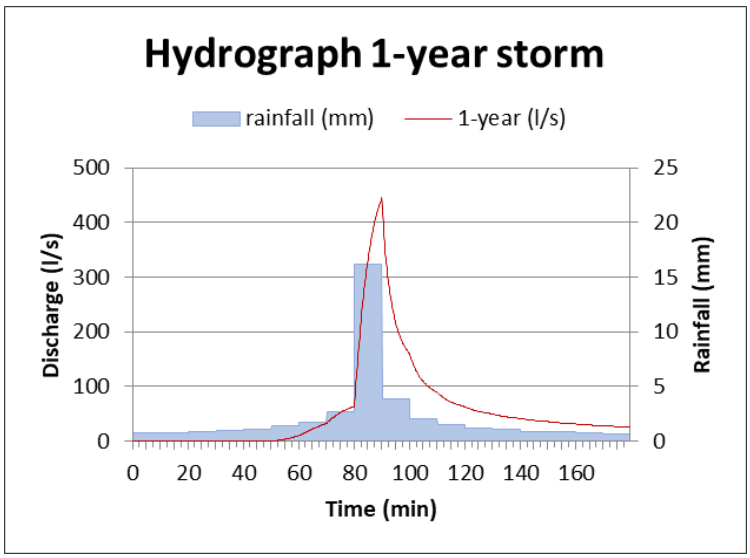

Figure 5.24: Hydrograph of the 1-year design storm scenario.

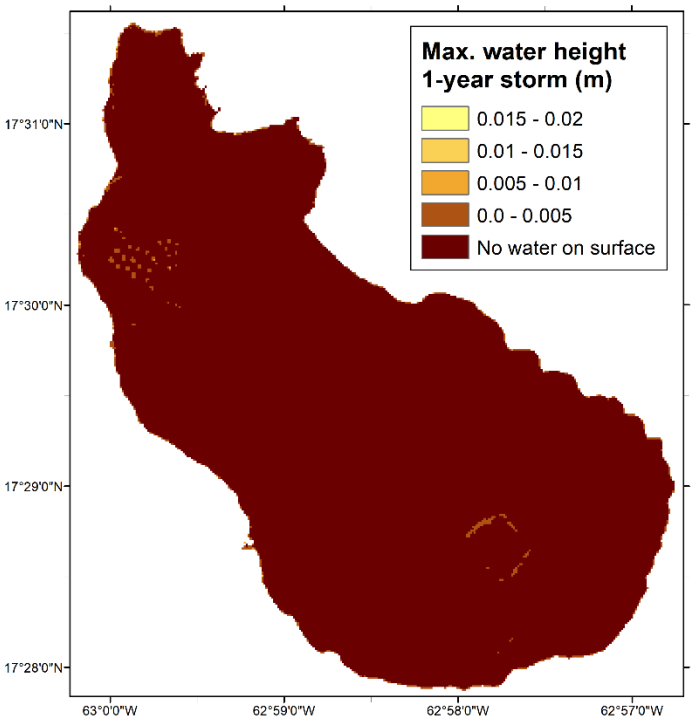

Figure 5.25: Map of the maximum water height during the 1-year design storm scenario run.

5.4.2 5-year return period

The 5-year design storm did result in slope failure, as can be seen in figure 5.26. The slope failure starts at t = 176 (min.) around the crater of the volcano in the south. In the next timesteps, the southern side of the volcano fails until the southern coast of the island has also failed. The last part to fail is the coastal cliffs. The timing of the slope failure can also be derived from the peak of the hydrograph (fig. 5.27). Figure 5.29 shows that the discharge resulting from the 5-year design storm alone is still not very significant. The map of the maximum water height on the surface of the same run shows the same (fig. 5.28). However, the maximum water height map of the run with slope failure enabled does show a significant water height (fig.5.30). The start of the extreme increase in water height coincides with the start of the slope failure (at t=176 min.).

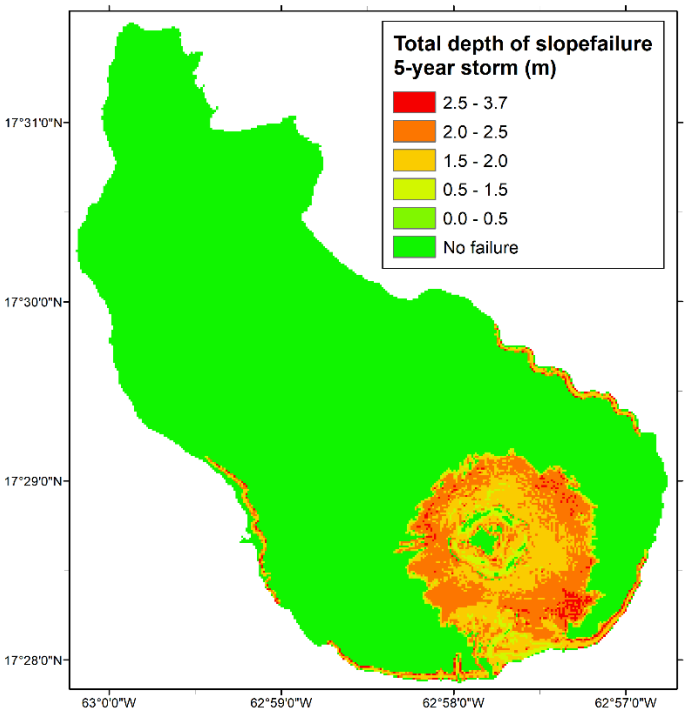

Figure 5.26: Total slope failure map result with the 5-year design storm scenario run.

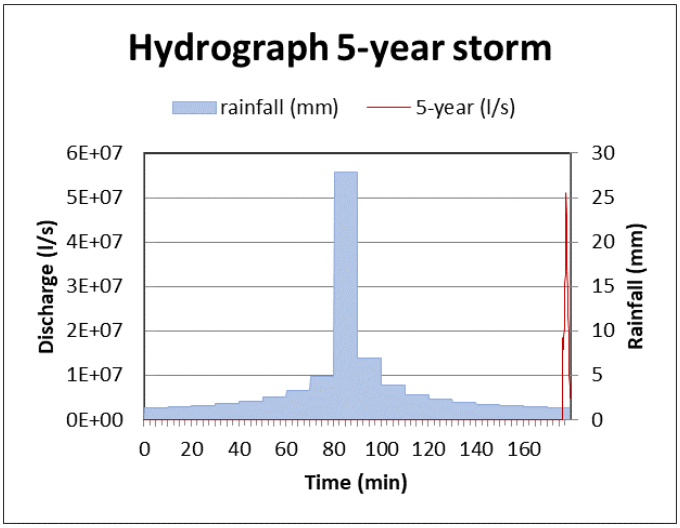

Figure 5.27: Hydrograph of the 5-year design storm scenario.

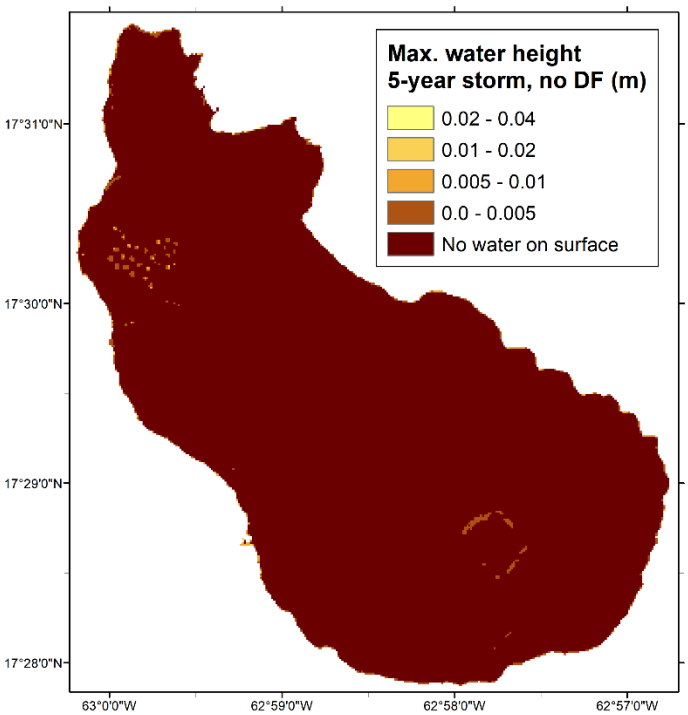

Figure 5.28: Map of the maximum water height during the 5-year design storm scenario run with slope failure disabled.

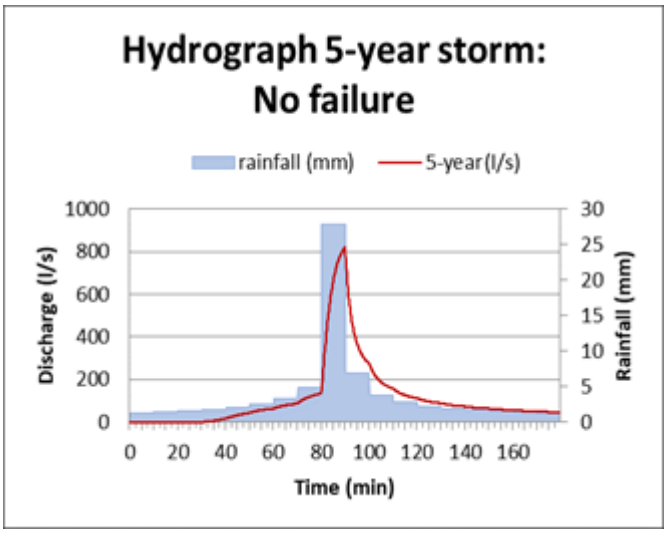

Figure 5.29: Hydrograph of the 5-year design storm scenario with slope failure disabled.

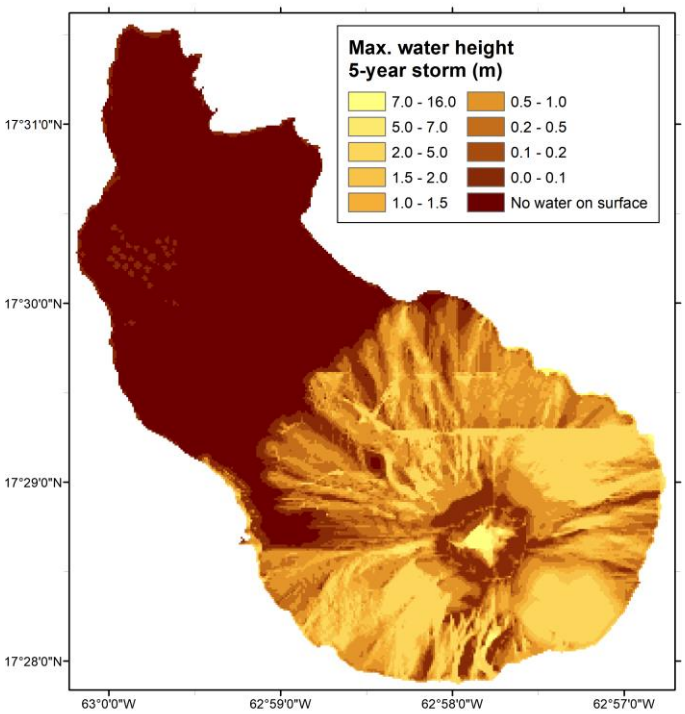

Figure 5.30: Map of the maximum water height during the 5-year design storm scenario run.

5.4.3 10-year return period

The 10-year design storm scenario shows a significant amount of slope failure (fig. 5.31). The slope failure is initiated in the southern part of the island first. The slope failure starts around the crater at t=119 (min.). The start location is the same as for the 5-year design storm run. The southern side of the volcano fails after this and then the coasts. The northern side of the island starts to fail at t=126 (min.). Here the northernmost part of the island fails first and then occurs further south. The timing of the slope failure can again also be seen in the hydrograph (fig. 5.32). The timing of the two peaks seems to coincide with the initiation of slope failure on the southern part of the island and then the northern side of the island. The discharge resulting from the design storm alone is again not enough to create significant runoff on the island (fig. 5.33). The amount of runoff from the design storm alone shows a small increase compared to the 5-year design storm run. The resulting maximum water height from the run with slope failure shows, again, an entirely different picture (fig. 5.35). The amount of runoff in this run is much larger than the run with a 5-year design storm (fig. 5.30). There are now also large water depths on the northern part of the island. The start of the extreme increase in water depth coincides again with the start of the slope failure in the south (t=119 min.).

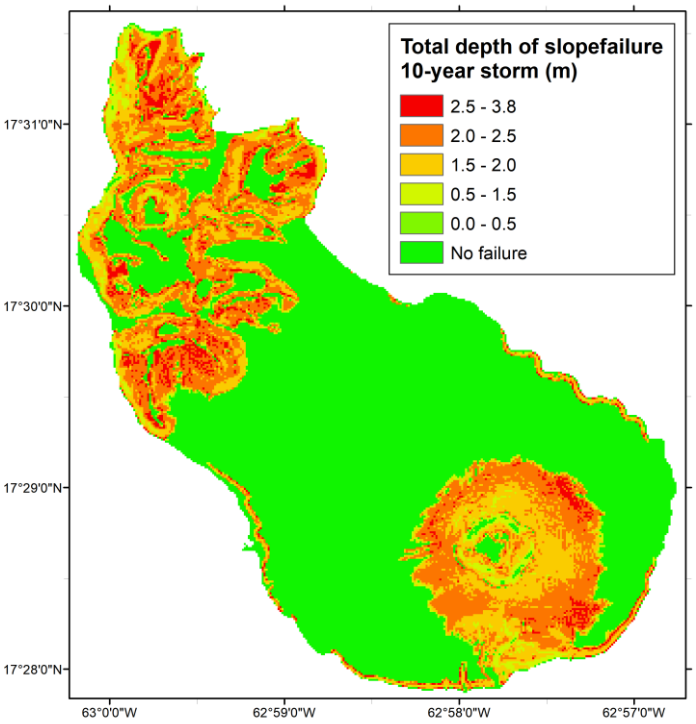

Figure 5.31: Total slope failure map result with the 10-year design storm scenario run.

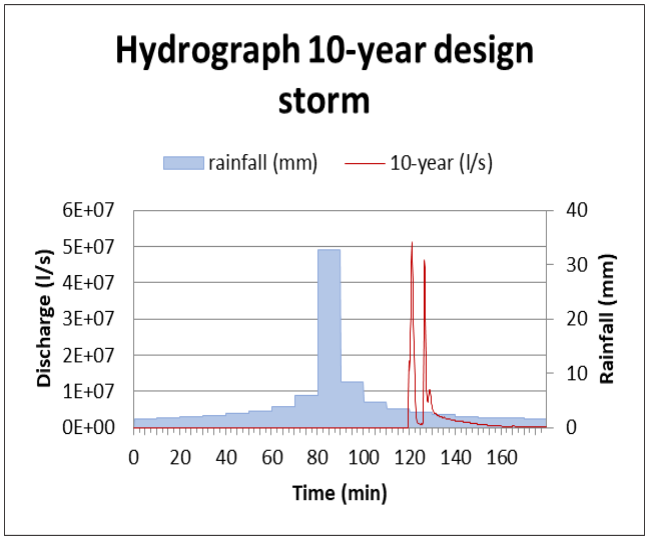

Figure 5.32: Hydrograph of the 10-year design storm scenario.

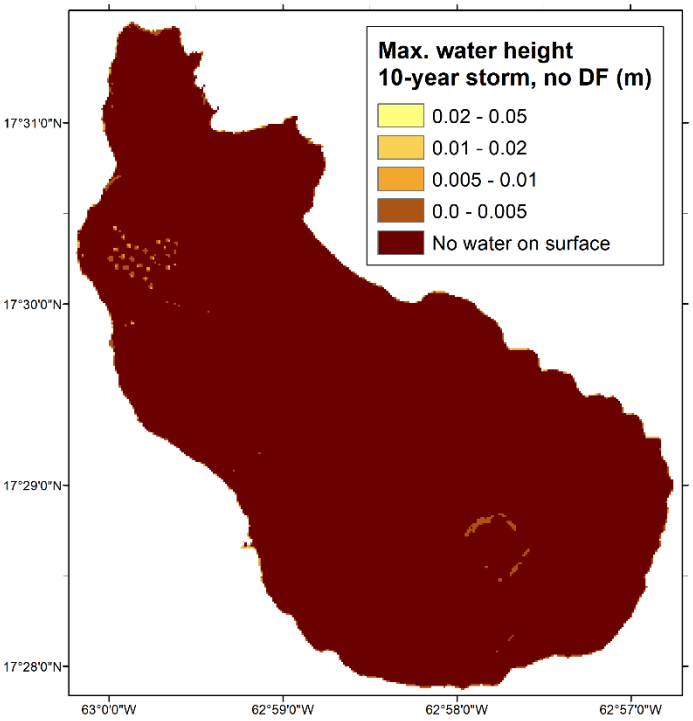

Figure 5.33: Map of the maximum water height during the 10-year design storm scenario run with slope failure disabled.

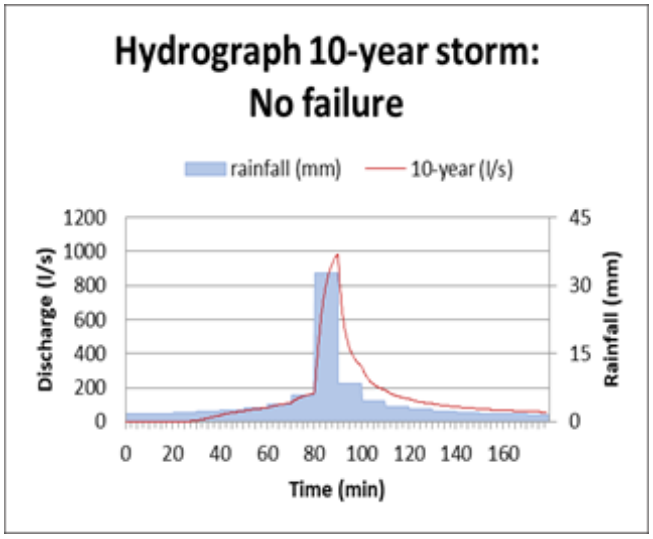

Figure 5.34: Hydrograph of the 10-year design storm scenario with slope failure disabled.

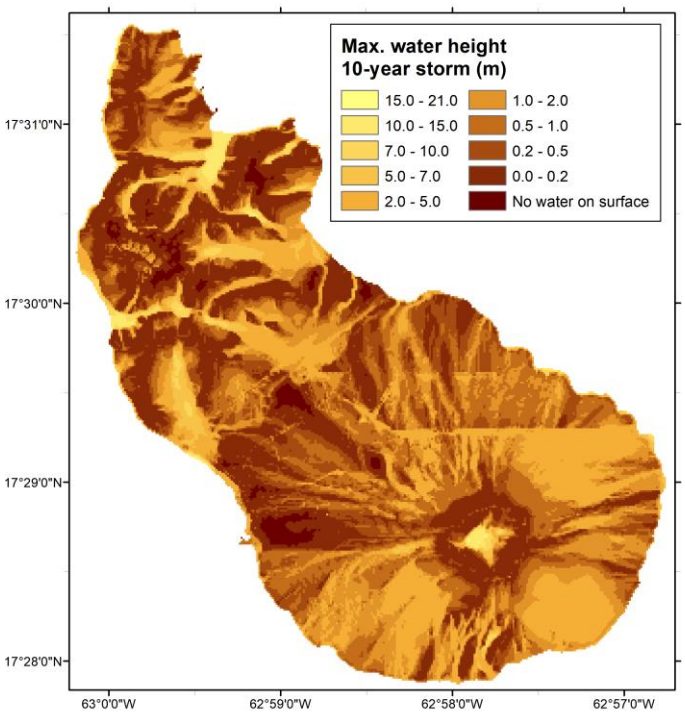

Figure 5.35: Map of the maximum water height during the 10-year design storm scenario run.

5.4.4 50-year return period

The map of the total slope failure of the 50-year design storm scenario does not show much difference from the 10-year scenario (fig. 5.36). The timing of the slope failure is however much earlier, as is also shown by the hydrograph (fig. 5.37). The slope failure occurs first on the southern side of the island at t=92 (min.). The slope failure in the north starts to fail at t=95 (min.). The delay between the initiation of failure of the two areas is thus much shorter than for the 10-year design storm. The water height resulting from the 50-year design storm alone is again not significant (figures 5.38 and 5.39). The map of the maximum water height from the run with slope failure does show extreme water depths (fig. 5.40). This map does not differ much from the map of the 10-year design storm run (fig. 5.35). The map from the 10-year design storm run shows some slightly higher values in some small areas. The extreme increase in water height coincides again with the start of failure in the south at t=92 (min.).

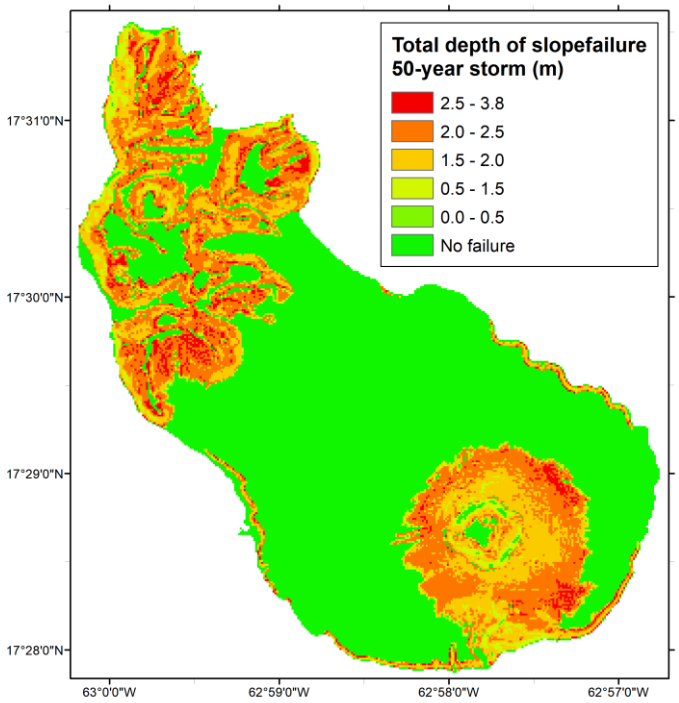

Figure 5.36: Total slope failure map result with the 50-year design storm scenario run.

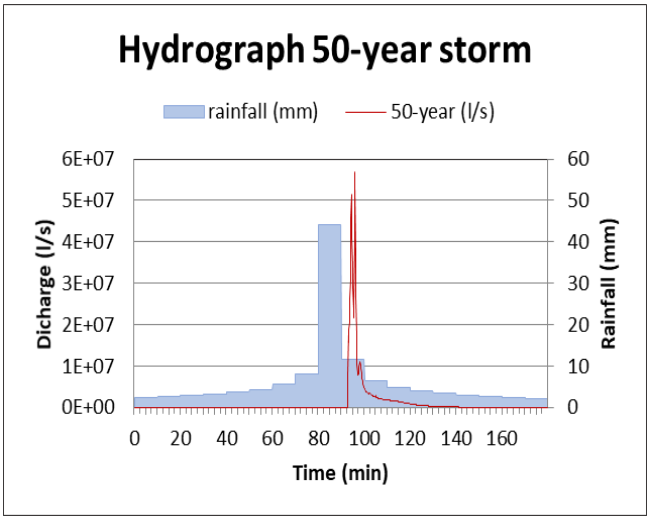

Figure 5.37: Hydrograph of the 50-year design storm scenario.

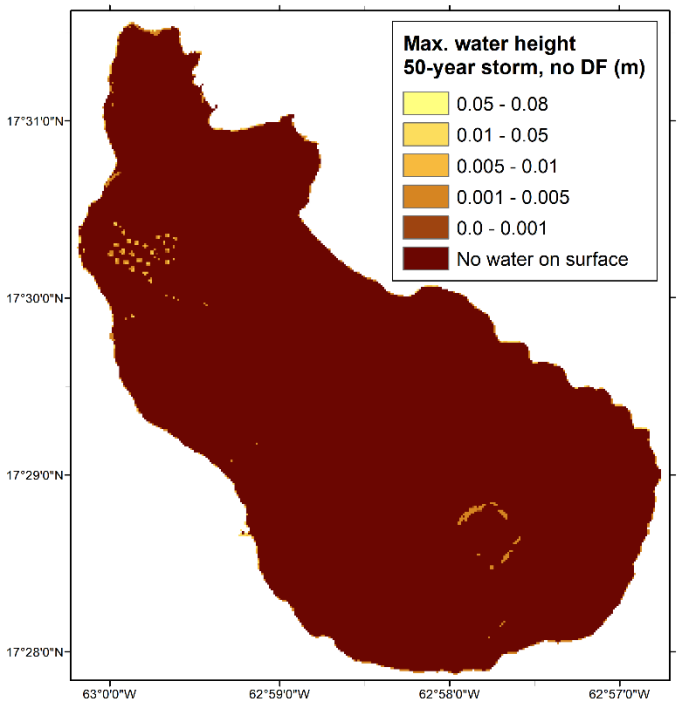

Figure 5.38: Map of the maximum water height during the 50-year design storm scenario run with slope failure disabled.

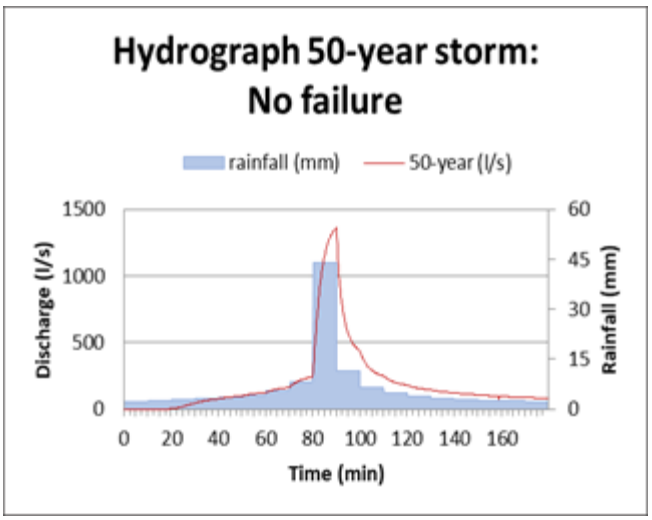

Figure 5.39: Hydrograph of the 50-year design storm scenario with slope failure disabled.

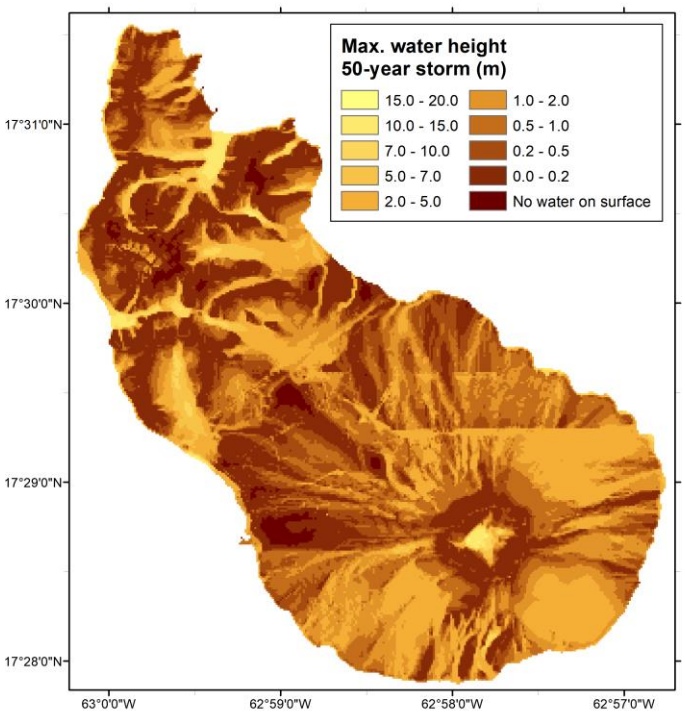

Figure 5.40: Map of the maximum water height during the 5-year design storm scenario run.

5.5 Hazard maps

The landslide and flood hazard maps are shown in figures 5.41 and 5.42. Since the simulation of overland flow is most likely overestimated in the model run with slope failure simulation enabled, only the maximum water height from the model runs with slope failure disabled were used for the creation of the flood hazard map. The thresholds for the hazard maps were set to 0.1 m for the maximum depth of flood water on the surface and 0.2 m for the maximum slope failure depth. The hazard classes were based on the return period of the hazards. The classes very high hazard, high hazard, medium hazard and low hazard corresponded respectively to a 1-year return period, a 5-year return period, a 10-year return period and a 50-year period. The no hazard class was used when the set threshold was not passed during any of the model runs.

The flood hazard map shows that there is no hazard from floods on the island (fig. 5.41) since the threshold of 0.1 m is never exceeded. The highest value of the maximum depth of flood water was 0.07 for one pixel during the 50-year design storm. This is likely an underestimation, as at least one new report shows that flooding is a problem on the island (The Daily Herald, 2017a).

The landslide hazard map shows very large areas of high or medium landslide hazard (fig. 5.42). The very high landslide hazard class was not assigned. The low hazard class was only assigned to a couple

of pixels in the Northern Hills. The extent of the areas classified as hazardous is not reflected by the field observations (fig. 5.13).

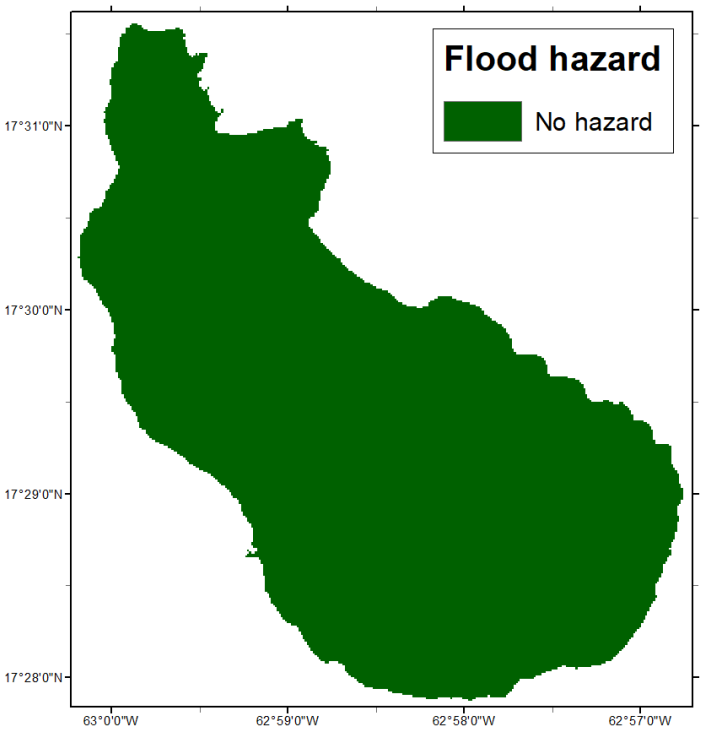

Figure 5.41: Flood hazard map according to the openLISEM model results.

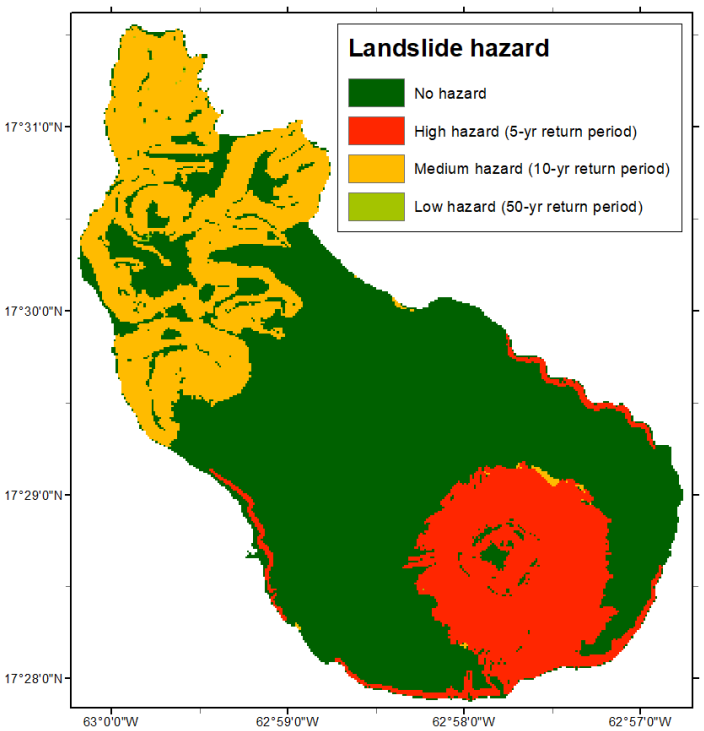

Figure 5.42: Landslide hazard map according to the openLISEM model results. This classification is not reflected by field observations (Figure 5.13).

Chapter 6 Discussion

The landslide hazard map shows that the steep slopes of the Quill volcano and the areas along the cliffs of the coasts have a high landslide hazard classification. The flood hazard map shows that there is no flood hazard on the island. The model results show that the areas around the Quill volcano and the cliffs at the coast show hazardous slope failure with a storm of a 5-year return period. After a 10-year return period, there are also landslides occurring in the Northern Hills, according to the model results. The runs with the slope stability functions disabled did not show any flood hazard for the island. This is most likely due to the high saturated conductivity of the soil. The runs with slope stability showed extreme flooding events when there was slope failure, which resulted most likely from the model including the water in the soil from the slope failure into the hydrological processes. This is supported by the fact that the initiation of these extreme water heights always coincides with the occurrence of slope failure.

However, when these results are compared to the hazard inventory and reports of hazards on the island, it is clear that the results give an overestimation of the landslide hazard and an underestimation of the flood hazard. The landslide hazard inventory shows that the coastal cliffs and the steep slopes on the southwestern side of the Quill volcano are prone to landslides. The spatial distribution of the model results reflects the spatial distribution of the events in the landslide inventory, but the extent and magnitude of the model results do not reflect the hazard inventory. It could be that the landslide inventory underestimates that landslide problem on the island, especially since only a few areas, mainly recent deposits of landslides, were visited. However, rationally it is highly likely that the that the model results overestimate the actual hazard of landslides on the island. The results of the 10-year design storm show that the island would lose large amounts of soil once every 10 years. Since there are no reports of such large-scale events, it is unlikely that these results reflect reality.

The resulting flood hazard map from the model runs with debris flow modelling disabled shows a more reasonable result. It was expected that the model would show at least some areas that experienced a flood hazard and even a high to very high flood hazard since reports have shown that most floods are caused by tropical storms and hurricanes with a respective return period of 1 year and 4-5 years (MacRae and Esteban, 2007; The Daily Herald, 2017a). It could be that this flood hazard does not show up due to the “coarse” cell size that was used. In pluvial flood modelling, it is more common to use very detailed surface data with a cell size of 5 m or less and an accuracy in the range of centimetres (Van Dijk et al., 2014; Blanc et al., 2012). Leitão et al. (2009) also showed that the use of DEMs with a resolution lower than 5 m produces inaccurate results in urban pluvial flooding. Besides the low

resolution that was used in this study, the used DEM also shows large artefacts (Figure 4.4). These artefacts also show up in the maximum water height model results of the model runs with the modelling of debris flows enabled (Figure 5.30, Figure 5.35 and Figure 5.40). A model run with the resolution of the DEM (5 m) would therefore still yield inaccurate results.

The results of the flood occurrence on the island, during the model runs with debris flow modelling enabled, highly overestimate the water height. The model predicts high flood water (more than 1m water depth) rushing down the slope of the volcano every 5-years and for a 10-year and 50-year return period the entire island is flooded. This flood water is initiated by slope failure in the model, as an analysis of the model results showed that the amount of water that contributes to the flood water is almost equal to the amount of water that is stored inside the slopes before failure. It is conceivable that the water inside these slopes is indeed released when slope failure occurs. However, it is more likely that this water stays within the debris and contributes to a debris flow. It could be that this actually happens inside the model and that the produced water height map also represents the water inside the debris flow. However, since both maps are produced separately it is unclear if this is the case.

Although the problem of slope failure overestimation would not be completely resolved, part of the problems with the results lies within the model input. Some of the most impactful input (cohesion and infiltration parameters) was provided as a uniform value. In reality, these parameters are of course more diverse, as is also evident from the soil map of the island (see appendix A). The current spatial distribution leads to several cells reaching failure together, which is enforced by the iterative slope stability calculation. A more diverse distribution of the soil parameters could solve the problem of the slope failure overestimation.

Another reason for overestimation could lie in the used design storms. Since the meteorological data from St. Eustatius was not detailed enough, the data for the design storms was taken from a meteorological station on the US Virgin Islands. This could have introduced some inaccuracy in the model results. However, a comparison with a combined meteorological dataset from St. Maarten and St. Eustatius showed that it is more likely that the IDF data from the US Virgin Island underestimates the intensity of the precipitation events occurring on St. Eustatius. It could, therefore, not explain the overestimation of the landslide hazard. It could explain the underestimation of the flood hazard. However, besides the already explained problems of the used DEM and cell-size, it is more likely that the underestimation is caused by the used storm duration. During the study, the storm duration was set to 3 hours in all the model runs since there was no information on the actual duration of precipitation events.

The sensitivity analysis of the new version of openLISEM showed that the general areas of slope failure occurrences did not change much with changes in the parameters. However, the amount of slope failure did show a high sensitivity, as did the timing of the slope failure. The cohesion, internal friction angle, soil depth and initial soil moisture content had the largest impact on the model results. In every model run, the northern part of the island failed before the southern part. However, the runs with a cohesion of 10 times the original value and the runs with a soil depth that was twice as high, showed failure in the south before the initiation of failure in the north. An explanation for this was not found.

Another interesting observation from the sensitivity analysis is the sensitivity of the delay between the two peaks in the hydrograph, in other words, the delay in slope failure initiation in the North and in the South. This is especially apparent in the sensitivity analysis with the initial soil moisture content and internal friction angle. It could be that the polynomial determination of the failure plane results in an exponential delay between the two peaks when the variables in the safety factor equation are changed.

The current version (v3.3) of the new openLISEM addition is therefore not suited for modelling landslide hazards on St. Eustatius. The sensitivity analysis showed that the overestimation would not be solved with a better calibration of the input parameters. The occurrence of slope failure in a single cell already leads to a sudden increase in modelled discharge. OpenLISEM could work for the assessment of the flood hazard on St. Eustatius when the debris flow simulation is disabled and a more detailed DEM is used.

It is highly likely that St. Eustatius does have a landslide and flood hazard problem. This is shown by both the hazard inventory and reports of hazard occurrences on the island. Besides this, research conducted on neighbouring islands also shows that the area is prone to landslide and flood hazards (Rijkers and Hack, 2000; Heinrich et al.,2001; DeGraff et al., 1989; Allemand et al., 2014; Anderson et al., 2010). Although this is not a solid argument for the occurrence of landslide and flood hazards on St. Eustatius, the similar geology and meteorological setting of these neighbouring islands indicates that some of these factors could also trigger or cause landslides and floods on St. Eustatius.

6.1 Recommendations

For future research, it is recommended to focus first on the creation of a better hazard inventory. Currently, the inventory is not sufficient enough to use as a validation tool in the hazard assessment. Since this inventory is needed for any hazard assessment method, it is better to focus on creating this dataset first. After the landslide inventory has been created, a new model should be used to model the landslide and flood processes on the island. This model would also need more detailed model input.

The landslide hazard inventory should be constructed from additional field observations of historical and future landslide events and the analysis of detailed aerial photography. The records of the field observations should include as much information about the landslides as possible, but especially information on the location, timing, extent and scarp of the landslides. This information can then later be used to determine the main causes and triggers of landslides on St. Eustatius.

The flood hazard inventory should be constructed by recording problem locations during flood events using point data. This point data should contain information on location, timing and the water height above the surface. The use of remote sensing is not suited for the survey, as the magnitude of the flood events is expected to be very minimal and most likely will not be registered (clearly) on data acquired with remote sensing.

It is recommended to use a different model for modelling of the hazards on the island in future research. If the new hazard inventory is extensive enough, a statistical approach could be used to create a landslide susceptibility map of the island. This approach would drastically lower the demand of the model input. However, the demand for the hazard inventory would be much higher than with a physically-based approach.

If the new hazard inventory is only suitable for validation purposes, a physically-based approach would be better suited. Examples of physically-based models that are commonly used in landslide modelling are TRIGRS (Baum et al., 2008), STARWARS-ProbStab (Van Beek, 2002), SHALSTAB (Dietrich and Montgomery, 1998), SINMAP 2 (Pack et al., 2005) and Scoops3D (Reid et al., 2015). The TRIGRS, STARWAR-ProbStab, SHALSTAB and SINMAP 2 models use the infinite slope method and are all coupled with a hydrological model. Due to the use of the infinite slope method, these models are only able to simulate shallow translational landslides. The Scoops3D model uses a version of the method of slices, which does not assume that the failure plane of a modelled landslide is linear. Due to this approach, the model is also able to model rotational landslides. Besides this Scoops3D uses a 3D environment, this makes it possible to estimate the depth of the failure plane as well. A disadvantage

of Scoops3D is the fact that the model is not coupled with a hydrological model and needs more detailed soil data as input.

SINMAP 2 is the only model in this list that uses a stochastic approach (Pack et al., 2005). This might be very suitable for the future modelling of landslide hazards on St. Eustatius since this reduces the demand of the model input. Instead of a single parameter value, the values for hydrological and geotechnical parameters can be given as a range (Pack et al., 2005). Since SINMAP 2 also models the overland flow, the model can also be used for the assessment of the flood hazard on St. Eustatius.

For the assessment of the flood hazard, it is mainly important that the used cell size is small enough (< 5 m). The ability to model with a very high resolution should thus be taken into consideration when choosing a new hazard model for St. Eustatius. Besides this, it is also important that the model is efficient and has a relatively short runtime while modelling with a high resolution.

During the collection of the field observations of historical landslide events, it is recommended that additional soil samples and field measurements are taken. This data can then be used to improve the model input. The sensitivity analysis showed that the cohesion, internal friction angle, soil depth and initial soil moisture content had the largest impact on the prediction of the model. This most likely also applies to other models since these parameters are important in any slope stability assessment, as they describe the shear strength and shear stress acting on the soil. Since the groundwater depth and hydraulic conductivity of the soil were not validated during the study, it is also recommended to collect information on these parameters. Depending on the chosen model, this demand for more detailed data is increased or some of the parameters can be calibrated with data from this study.

This study also showed that the meteorological dataset from St. Eustatius is not detailed enough to be used in event-based or design-storm based analyses. It is therefore recommended to install a meteorological station on St. Eustatius that not only provides daily precipitation values, but also hourly precipitation data and evaporation data. The evaporation data can then be used for analyses over longer time periods, while the hourly precipitation data can be used to simulate precipitation events.

A last improvement of the model input would be the creation of a new DEM. This DEM could be created by using aerial photography. However, as shown by the DEM used in this study, the high vegetation density makes it difficult to mosaic the taken images of the island. The use of LiDAR might solve this problem and give a more accurate result. A DEM created from LiDAR data generally has a higher resolution than DEM created with other methods (Prokop and Panholzer, 2009), which is very important for the flood hazard assessment on St. Eustatius. However, the collection of LiDAR data is very expensive and often needs more intensive post-processing (Prokop and Panholzer, 2009).

Chapter 7 Conclusion

The goal of this study was to create a multi-hazard map of the landslide and flood hazards on St. Eustatius. The study investigated the historical occurrence of the hazards and the magnitudes of these hazards for different return periods. This goal was achieved by creating a hazard inventory from field observations and modelling the hazard occurrences with openLISEM. The model was run using several model scenarios with storm events of a 1-year, 5-year, 10-year and 50-year return period.

The landslide hazard inventory showed that the coastal cliffs and the steep slopes on the south-western side of the Quill volcano are prone to landslides. The flood hazards were not mapped since it was too difficult to recognize previous flood occurrences in the field. The slope failure results of the model scenarios show that the island does not see a landslide hazard with a 1-year return period, but significant slope failure is predicted with a 5-year, 10-year and 50-year return period. The slopes of the Quill volcano and the coasts see the highest landslide hazard according to the model. The model predicts no flood hazard. The results from the model agree with the spatial occurrence of the landslide hazards. However, magnitude landslide hazard is highly overestimated by the model. The flood hazard is most likely underestimated.

The suitability of the model was investigated with a sensitivity analysis and the aforementioned validation of the model results. The sensitivity analysis showed that the model is very sensitive to changes in the values of soil cohesion, internal friction angle, soil moisture content and soil depth. Both the magnitude and timing of slope failure showed large changes. Most of the changes were easily explained. However, a reason for the changes in the location of the first slope failure occurrence and the delay between initiation of landslides in the North and the South was not found.

In conclusion, the study has shown that there are problems with landslides and floods on the island. However, the magnitude of this problem could not be defined. The new component of the openLISEM model still has some issues and is not suited, at the moment, to provide a detailed or accurate prediction of the hazards that occur on the island. The results should thus be interpreted with care. For future research, it is important that a better hazard inventory of all the occurring hazards on the island is constructed first. After this, a better DEM, more detailed data on soil characteristics of the island and a more suited model will also contribute to a better prediction of the hazards occurring on the island.

Appendix A: Soil map

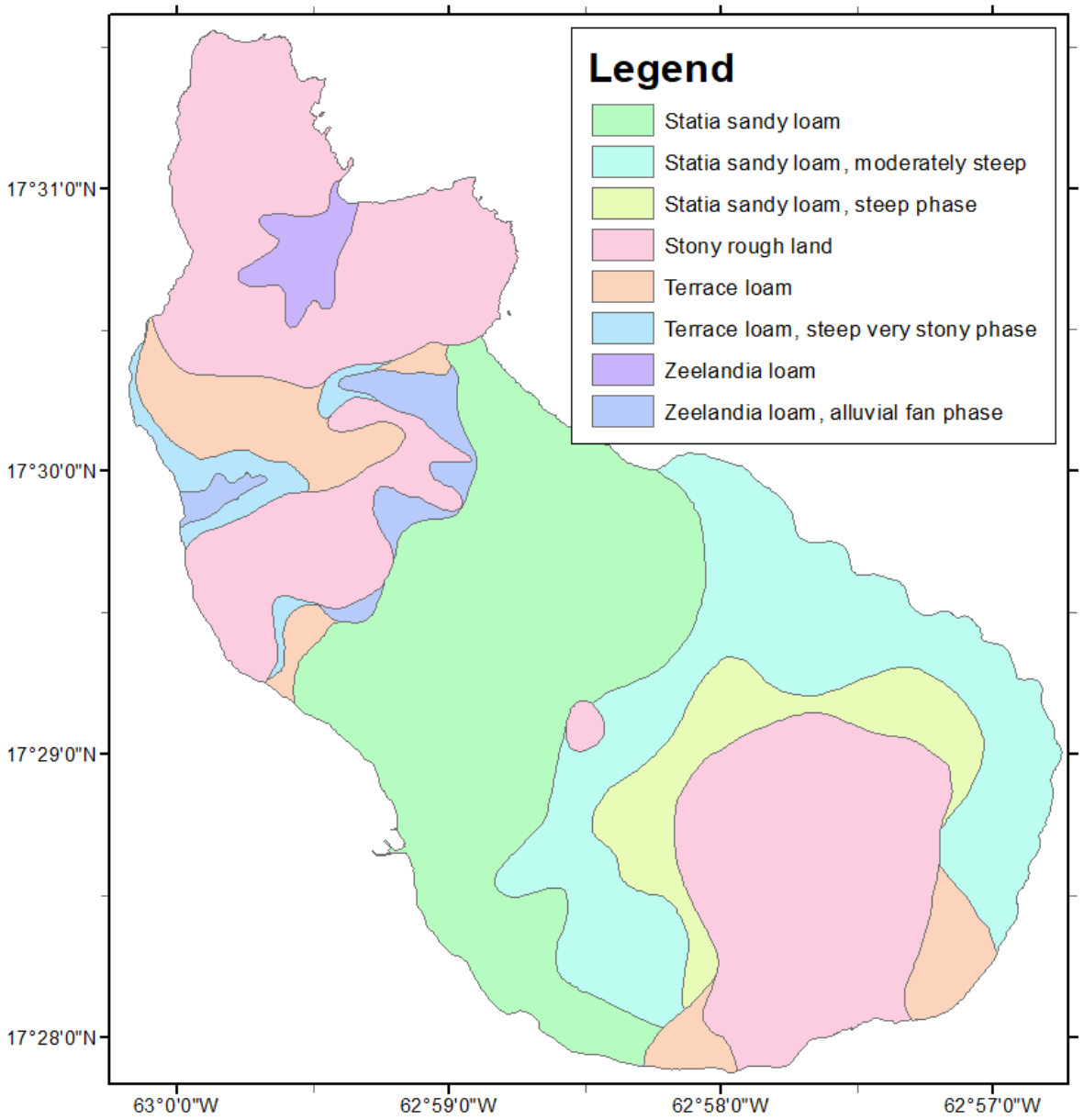

Figure A.1: Soil map of St. Eustatius (Koomen et al., 2012).

Appendix B: Smith and Parlange with Green and Ampt comparison

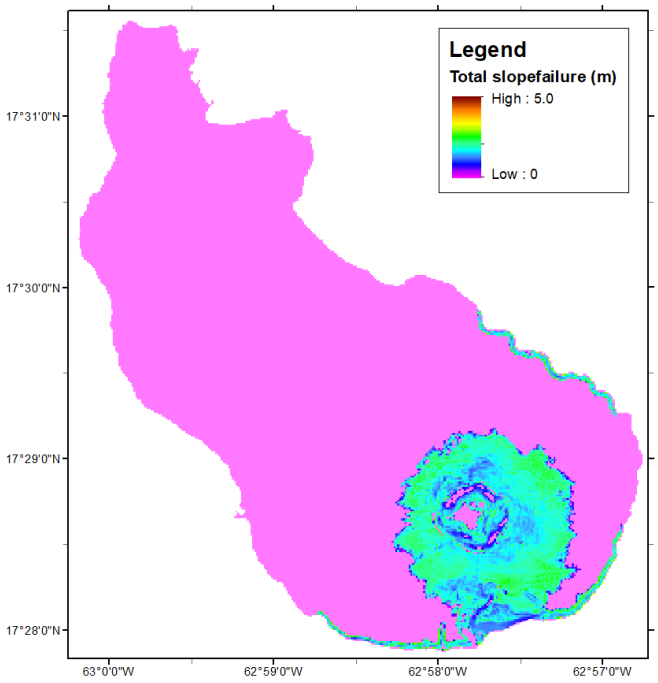

Figure B.1: Slope failure map result using the Smith & Parlange infiltration model using a 5-year design storm.

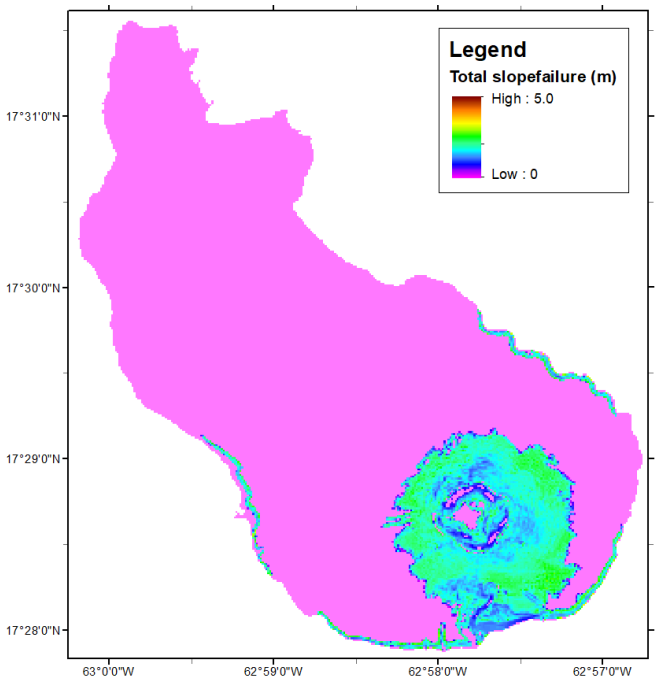

Figure B.2: Slope failure map result using the Green & Ampt infiltration method with a 5-year design storm.

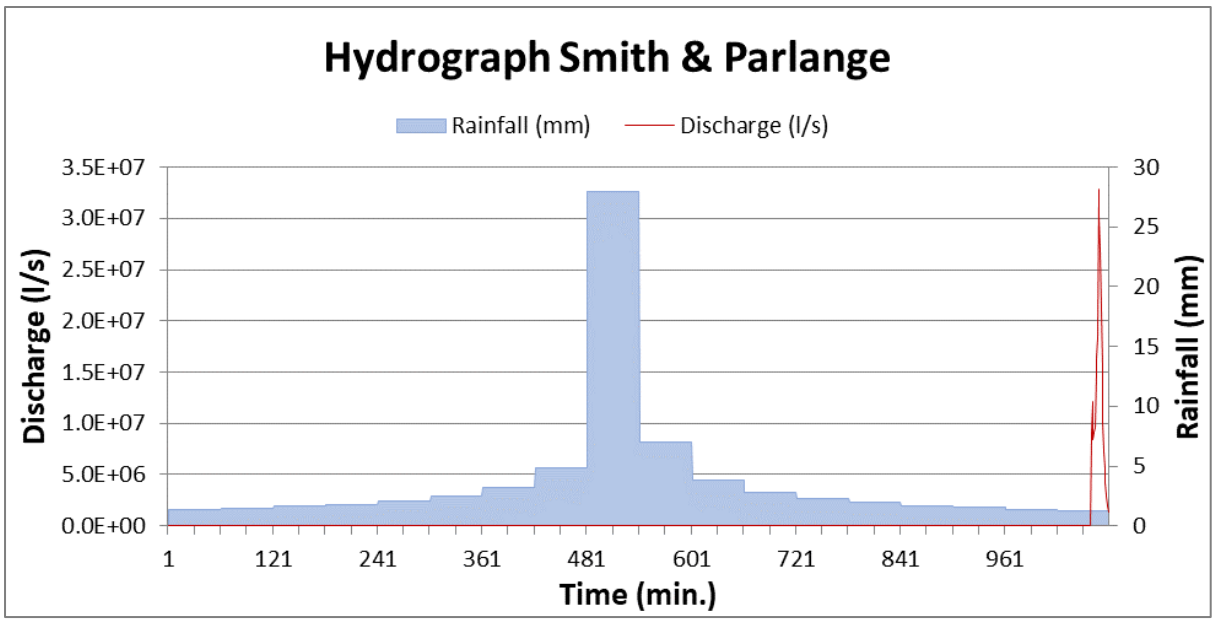

Figure B.3: Hydrograph of the model result with the Smith & Parlange infiltration method using a 5-year design storm.

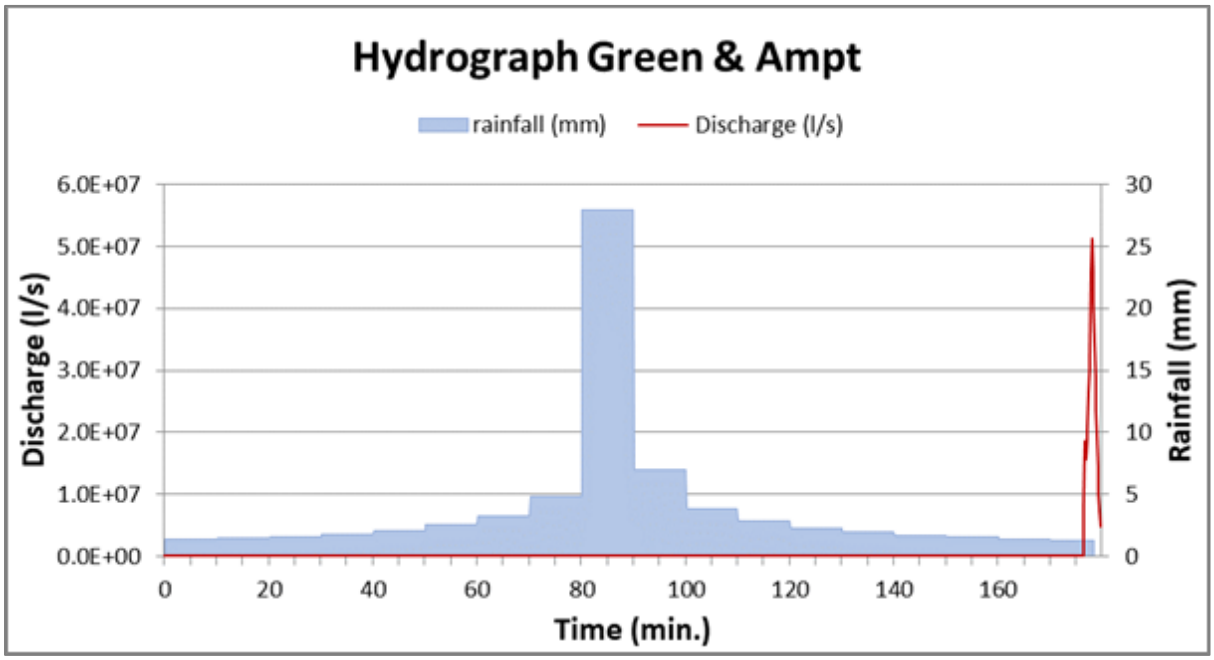

Figure B.4: Hydrograph of the model result with the Green & Ampt infiltration method using a 5-year design storm.

Appendix C: Design storms

1-year design storm:

```
#Statia IDF derived 3-hour rainfall taken with a 1yr return period
2
time  (min.)
intensity  (mm/h)
0     0
10    0.709259869
20    0.775841334
30    0.860085777
40    0.970842627
50    1.124447534
60    1.355201655
70    1.751408169
80    2.648196643
90    16.2158474
100   3.831403575
110   2.088472811
120   1.522491827
130   1.226725614
140   1.040775058
150   0.911376354
160   0.815316502
170   0.740729195
180   0.6808668
300   0
```

5-year design storm:

```
#Statia IDF derived 3-hour rainfall taken with a 5yr return period
2
time  (min.)
intensity  (mm/h)
0     0
10    1.335793686
20    1.458359096
30    1.613115252
40    1.816079828
50    2.096745201
60    2.516844845
70    3.234652837
80    4.847172144
90    27.91451904
100   6.956189993
110   3.842473445
120   2.820415827
130   2.283158095
140   1.94397059
```

```
150   1.707172696
160   1.530917577
170   1.39375315
180   1.283452295
300   0
```

10-year design storm:

```
#Statia IDF derived 3-hour rainfall taken with a 10yr return period
2
time  (min.)
intensity  (mm/h)
0     0
10    1.615323744
20    1.762397446
30    1.94796943
40    2.191151978
50    2.527105391
60    3.029350405
70    3.886124582
80    5.805999529
90    32.77563654
100   8.30970613
110   4.610491495
120   3.391887545
130   2.750052925
140   2.344280093
150   2.060691062
160   1.849421332
170   1.684884703
180   1.55248631
300   0
```

50-year design storm:

```
#Statia IDF derived 3-hour rainfall taken with a 50yr return period
2
time  (min.)
intensity  (mm/h)
0     0
10    2.329686655
20    2.537861098
30    2.800088772
40    3.143056288
50    3.615757877
60    4.32038475
70    5.517725226
80    8.184640205
90    44.08410483
100   11.63834027
110   6.526257952
120   4.827685353
130   3.928825523
```

```
140   3.358663905
150   2.959152957
160   2.660890938
170   2.428186537
180   2.240642505
300   0
```

Appendix D: Detailed list measurements fieldwork (results)

Table D.1: Table of data points indicating which data points had samples taken and which samples were used for a dry-bulk density analysis.

Sample #	Sample (y/n?)	Dry bulk (y/n?)
D10-001	YES	NO
D10-002	YES	YES
D10-003	YES	NO
D2-001	NO	NO
D2-002	NO	NO
D3-001	YES	NO
D3-002	NO	NO
D3-003	NO	NO
D4-001	NO	NO
D4-002	YES	NO
D4-003	NO	NO
D4-004	NO	NO
D4-005	NO	NO
D4-006	NO	NO
D5-001	YES	YES
D5-002	YES	YES
D5-003	NO	NO
D5-004	NO	NO
D6-001	NO	NO
D6-002	NO	NO
D6-003	YES	NO
D6-004	YES	YES
D7-001	NO	NO
D7-002	YES	YES
D7-003	NO	NO
D8-001	NO	NO
D8-002	YES	YES
D8-003	NO	NO
D8-004	YES	YES
D9-001	YES	YES
D9-002	NO	NO
D9-003	NO	NO
D9-004	YES	YES
D9-005	NO	NO

Table D.2: List of data collected in the field and from the samples.

Sample #	Soiltype	Land-use	Stoniness (-)	Rocksize (m)	Grainsize	Theta (-)	Dried theta (-)	Torvane (kg/cm2)	Penetrometer (kg/cm2)
D10-001	Rs	Shrubs	0.8	0.05	n/a	n/a	0.041945005	3.583333333	n/a
D10-002	Rs	Low trees	0.8	0.325	n/a	n/a	0.035416123	2.533333333	n/a
D10-003	Sl	Grass	0.1	0.01	n/a	n/a	0.022482014	3.2	3.708333333
D2-001	Rs	Forest	0.9	0.3	n/a	n/a	n/a	n/a	n/a
D2-002	Sl	Grass	n/a	n/a	75-150um	0.01	n/a	2.275	n/a
D3-001	Sm	Grass	0.5	0.105	105-150um	0.0592	0.034413715	1.95	2.375
D3-002	Sm	Grass	0.5	0.01	n/a	0.123	n/a	2.35	3.55
D3-003	Sm	Grass	n/a	n/a	50 - 75um	0.031333	n/a	2.416666667	3.7625
D4-001	Rs	Soil outcrop	0.4	0.085	n/a	n/a	n/a	n/a	n/a
D4-002	Ss	Forest hillside	n/a	n/a	105-150um	0.1372	0.127491352	2.133333333	1.8125
D4-003	Rs	Forest hillside	0.8	0.01	n/a	0.07325	n/a	1.928571429	1.25
D4-004	Rs	Forest hillside	n/a	n/a	n/a	0.118	n/a	2.45	2.9
D4-005	Rs	Forest, unstable slopes	n/a	n/a	105-150um	0.16675	n/a	2.8	2.3375
D4-006	Rs	Dry Forest, hill	n/a	n/a	n/a	0.0715	n/a	1.72	1.32
D5-001	Tl	Shrubs with tress, hillside	0.7	0.01	n/a	0.118749	0.14978615	3.17	2.447142857
D5-002	Sm	Shrubs (coralita)	0.4	0.1525	150-210um	0.149714	0.135750775	2.408333333	2.525
D5-003	Sm	Grass	0.5	0.02	n/a	0.5426	n/a	3.183333333	3.341666667
D5-004	Sm	Shrubs	0.5	0.21	n/a	0.2172	n/a	2.75	1.64
D6-001	Rs	Forest, hillside	0.6	0.225	50 -75 um	0.109571	n/a	2.666666667	2.741666667
D6-002	Sl	Shrubs	0.5	0.01	n/a	0.079833	n/a	2.2	n/a
D6-003	Sm	Shrubs	0.6	0.01	75 - 105um	0.080625	0.0562249	2.683333333	3.791666667
D6-004	Sm	Shrubs	0.3	0.01	150-210um	0.113	0.090640769	2.55	3.483333333
D7-001	Sm	Shrubs (small plants 1m)	0.4	0.155	210-300um	0.0718	n/a	2.392857143	3.258333333
D7-002	Sm	Shrubs	0.4	0.01	150-210um	0.074513	0.128828443	2.628571429	2.85

Table D.2: Continued.

Sample #	Soiltype	Land-use	Stoniness (-)	Rocksize (m)	Grainsize	Theta (-)	Dried theta (-)	Torvane (kg/cm2)	Penetrometer (kg/cm2)
D7-003	Ss	Shrubs	0.6	0.01	n/a	0.077	n/a	3.6	n/a
D8-001	Sl	Shrubs	0.3	0.155	75-105um	0.0865	n/a	2.941666667	2.4
D8-002	Sl	Shrubs	0.3	0.01	105-150um	0.088375	0.123312997	3.266666667	4.0875
D8-003	Tl	Shrubs/trees (4-5m)	0.5	0.01	50 - 75um	0.034429	n/a	2.98	1.8125
D8-004	Rs	Shrubs/some trees	n/a	0.305	75 - 105um	0.0665	0.073370082	1.071762119	2.333333333
D9-001	Sl	Grass, crusted soil	n/a	0.1525	Too windy	0.125	0.052444157	1.258571825	n/a
D9-002	Sl	Grass	n/a	0.25	105-150um	0.1133	n/a	n/a	n/a
D9-003	Za	Shrubs/grass	n/a	0.3	105-150um	0.104667	n/a	n/a	n/a
D9-004	Ss	Forest, hill	n/a	0.01	105-150um	0.1675	0.10607077	1.214772385	3.216666667
D9-005	Ss	Forest, hill	n/a	0.155	75 - 105um	0.1125	n/a	n/a	3.341666667
Average:	n/a	n/a	n/a	0.11	n/a	0.115	0.08	1.17392686	2.761929563

Table D.2: Continued.

Sample #	Dry bulk density (gr/cm3):	D50 (um)	D90 (um)
D10-001	n/a	508.198	3600.655
D10-002	1.561704696	838.3049	9285.617
D10-003	n/a	432.967	2883.562
D2-001	n/a	n/a	n/a
D2-002	n/a	n/a	n/a
D3-001	n/a	550.2775	3734.998
D3-002	n/a	n/a	n/a
D3-003	n/a	n/a	n/a
D4-001	n/a	n/a	n/a
D4-002	n/a	n/a	n/a

Table D.2: Continued.

Sample #	Dry bulk density (gr/cm3):	D50 (um)	D90 (um)
D4-003	n/a	n/a	n/a
D4-004	n/a	n/a	n/a
D4-005	n/a	n/a	n/a
D4-006	n/a	n/a	n/a
D5-001	1.119330349	254.4972	1273.1
D5-002	1.216300272	263.7786	1227.813
D5-003	n/a	n/a	n/a
D5-004	n/a	n/a	n/a
D6-001	n/a	n/a	n/a
D6-002	n/a	n/a	n/a
D6-003	n/a	n/a	n/a
D6-004	1.069826795	257.747	1036.389
D7-001	n/a	n/a	n/a
D7-002	0.951160869	315.9055	1298.809
D7-003	n/a	n/a	n/a
D8-001	n/a	n/a	n/a
D8-002	1.101912432	261.3654	1088.939
D8-003	n/a	n/a	n/a
D8-004	1.071762119	212.1465	765.1541
D9-001	1.258571825	452.2857	2617.76
D9-002	n/a	n/a	n/a
D9-003	n/a	n/a	n/a
D9-004	1.214772385	450.3696	2475.576
D9-005	n/a	n/a	n/a
Average:	1.17392686	399.8202	2607.364

Appendix E: Pedotransfer functions

Table D.1: Table of the used pedotransfer functions (Saxton and Rawls, 2006). For symbol definitions see table E.2.

Variable	Equation	R^2/S_e	Eq.
	Moisture Regressions		
θ_{1500}	$\theta_{1500} = \theta_{1500t} + (0.14 \times \theta_{1500t} - 0.02)$ $\theta_{1500t} = -0.024S + 0.487C + 0.006OM + 0.005(S \times OM) - 0.013(C \times OM) + 0.068(S \times C) + 0.031$	0.86/0.02	1
θ_{33}	$\theta_{33} = \theta_{33t} + [1.283(\theta_{33t})^2 - 0.374(\theta_{33t}) - 0.015]$ $\theta_{33t} = -0.251S + 0.195C + 0.011OM + 0.006(S \times OM) - 0.027(C \times OM) + 0.452(S \times C) + 0.299$	0.63/0.05	2
$\theta_{(S-33)}$	$\theta_{S-33} = \theta_{(S-33)t} + (0.636\theta_{(S-33)t} - 0.107)$ $\theta_{(S-33)t} = 0.278S + 0.034C + 0.022OM - 0.018(S \times OM) - 0.027(C \times OM) - 0.584(S \times C) + 0.078$	0.36/0.06	3
ψ_e	$\psi_e = \psi_{et} + (0.02\psi_{et}^2 - 0.113\psi_{et} - 0.70)$ $\psi_{et} = -21.67S - 27.93C - 81.97\theta_{S-33} + 71.12(S \times \theta_{S-33}) + 8.29(C \times \theta_{S-33}) + 14.05(S \times C) + 27.16$	0.78/2.9	4
θ_S	$\theta_S = \theta_{33} + \theta_{(S-33)} - 0.097S + 0.043$	0.29/0.04	5
ρ_N	$\rho_N = (1 - \theta_S)2.65$		6
	Density Effects		
ρ_{DF}	$\rho_{DF} = \rho_N \times DF$		7
θ_{S-DF}	$\theta_{S-DF} = 1 - (\rho_{DF}/2.65)$		8
θ_{33-DF}	$\theta_{33-DF} = \theta_{33} - 0.2(\theta_S - \theta_{S-DF})$		9
$\theta_{(S-33)DF}$	$\theta_{(S-33)DF} = \theta_{S-DF} - \theta_{33-DF}$		10
	Moisture-Tension		
$\psi_{(1500-33)}$	$\psi_\theta = A(\theta)^{-B}$		11
$\psi_{(33-\psi e)}$	$\psi_\theta = 33.0 - [(\theta - \theta_{33})(33.0 - \psi_e)/(\theta_S - \theta_{33})]$		12
$\theta_{(\psi e-0)}$	$\theta = \theta_S$		13
A	$A = \exp(\ln 33 + B\ln\theta_{33})$		14
B	$B = [\ln(1500) - \ln(33)]/[\ln(\theta_{33}) - \ln(\theta_{1500})]$		15
	Moisture–Conductivity		
K_S	$K_S = 1930(\theta_s - \theta_{33})^{(3-\lambda)}$		16
K_θ	$K_\theta = K_S(\theta/\theta_S)^{[3 + (2/\lambda)]}$		17
λ	$\lambda = 1/B$		18
	Gravel Effects		
R_v	$R_v = (\alpha R_w)/[1 - R_w(1 - \alpha)]$		19
ρ_B	$\rho_B = \rho_N(1 - R_v) + (R_v \times 2.65)$		20
PAW_B	$PAW_B = PAW(1 - R_v)$		21
K_b/K_s	$K_b/K_s = \dfrac{1 - R_w}{[1 - R_w(1 - 3\alpha/2)]}$		22
	Salinity Effects		
Ψ_O	$\Psi_O = 36EC$		23
$\Psi_{O\theta}$	$\Psi_{O\theta} = \dfrac{\theta_S}{\theta}(36EC)$		24

Table E.2: Symbol definitions for the pedotransfer functions in table E.1 (Saxton and Rawls, 2006).

Symbol	Definition
A, B	Coefficients of moisture-tension, Eq. [11]
C	Clay, %w
DF	Density adjustment Factor (0.9–1.3)
EC	Electrical conductance of a saturated soil extract, dS m^{-1} (dS/m = mili-mho cm^{-1})
FC	Field Capacity moisture (33 kPa), %v
OM	Organic Matter, %w
PAW	Plant Avail. moisture (33–1500 kPa, matric soil), %v
PAW_B	Plant Avail. moisture (33–1500 kPa, bulk soil), %v
S	Sand, %w
SAT	Saturation moisture (0 kPa), %v
WP	Wilting point moisture (1500 kPa), %v
θ_ψ	Moisture at tension ψ, %v
θ_{1500t}	1500 kPa moisture, first solution, %v
θ_{1500}	1500 kPa moisture, %v
θ_{33t}	33 kPa moisture, first solution, %v
θ_{33}	33 kPa moisture, normal density, %v
$\theta_{33\text{-}DF}$	33 kPa moisture, adjusted density, %v
$\theta_{(S\text{-}33)t}$	SAT-33 kPa moisture, first solution, %v
$\theta_{(S\text{-}33)}$	SAT-33 kPa moisture, normal density %v
$\theta_{(S\text{-}33)DF}$	SAT-33 kPa moisture, adjusted density, %v
θ_S	Saturated moisture (0 kPa), normal density, %v
$\theta_{S\text{-}DF}$	Saturated moisture (0 kPa), adjusted density, %v
ψ_θ	Tension at moisture θ, kPa
ψ_{et}	Tension at air entry, first solution, kPa
ψ_e	Tension at air entry (bubbling pressure), kPa
K_S	Saturated conductivity (matric soil), mm h^{-1}
K_b	Saturated conductivity (bulk soil), mm h^{-1}
K_θ	Unsaturated conductivity at moisture θ, mm h^{-1}
ρ_N	Normal density, g cm^{-3}
ρ_B	Bulk soil density (matric plus gravel), g cm^{-3}
ρ_{DF}	Adjusted density, g cm^{-3}
λ	Slope of logarithmic tension-moisture curve
α	Matric soil density/gravel density (2.65) = ρ/2.65
Rv	Volume fraction of gravel (decimal), g cm^{-3}
Rw	Weight fraction of gravel (decimal), g g^{-1}
Ψ_O	Osmotic potential at $\theta = \theta_S$, kPa
$\Psi_{O\theta}$	Osmotic potential at $\theta < \theta_S$, kPa

Appendix F: Sensitivity analysis

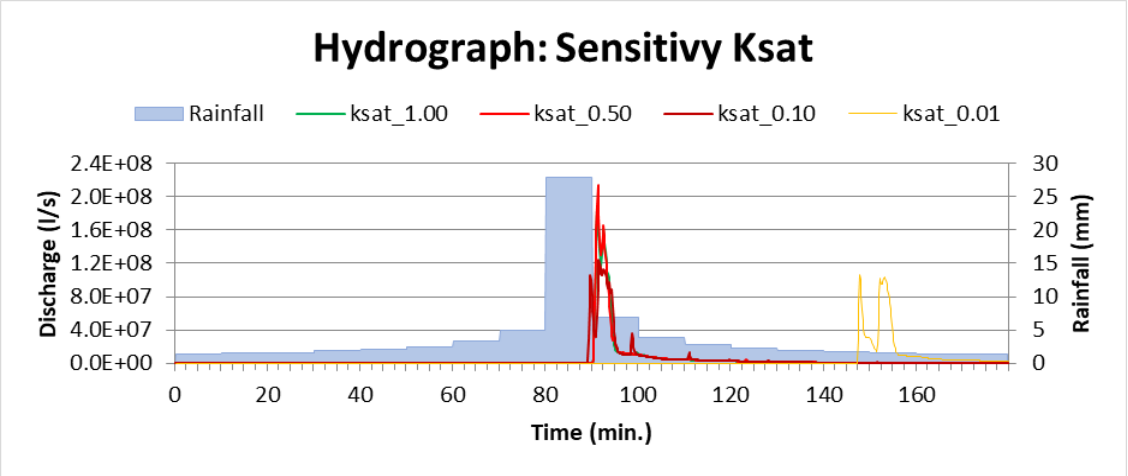

Figure F.1: Hydrograph of the sensitivity analysis with the saturated hydraulic conductivity. Multiplied by 0.01-1.00.

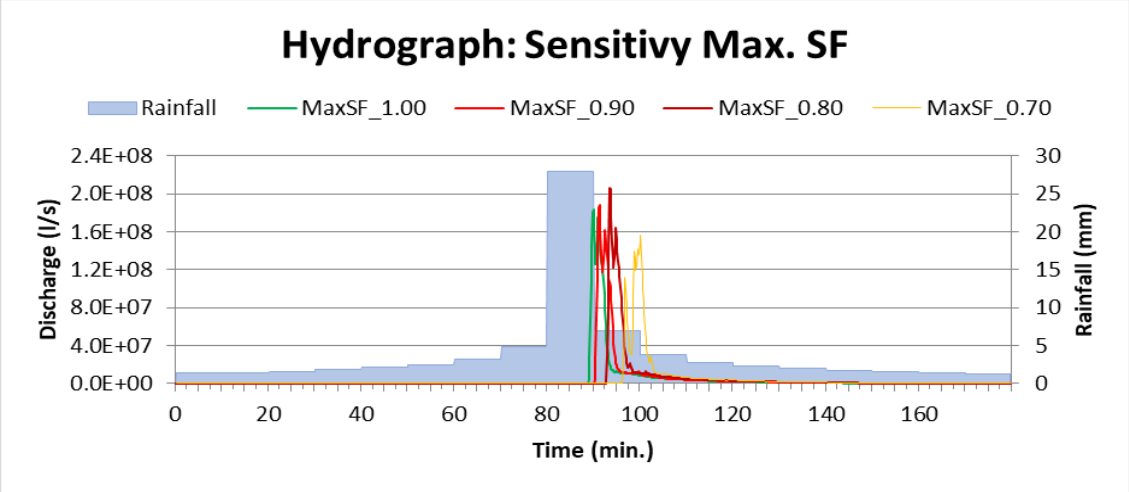

Figure F.2: Hydrograph of the sensitivity analysis with the maximum safety factor (before failure). Changed to a value of 0.70-1.00.

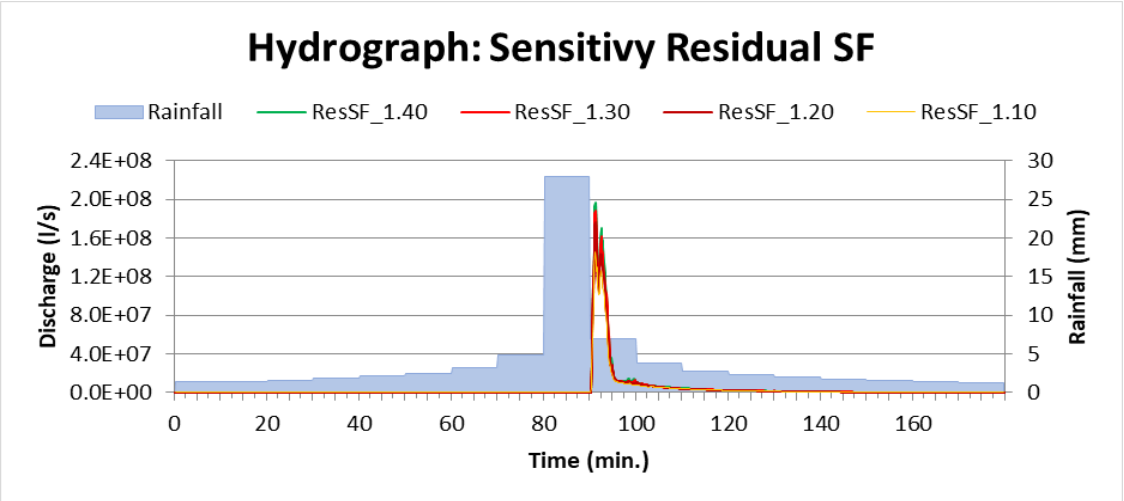

Figure F.3: Hydrograph of the sensitivity analysis with residual safety factor (after failure). Changed to a value of 1.00-1.40.

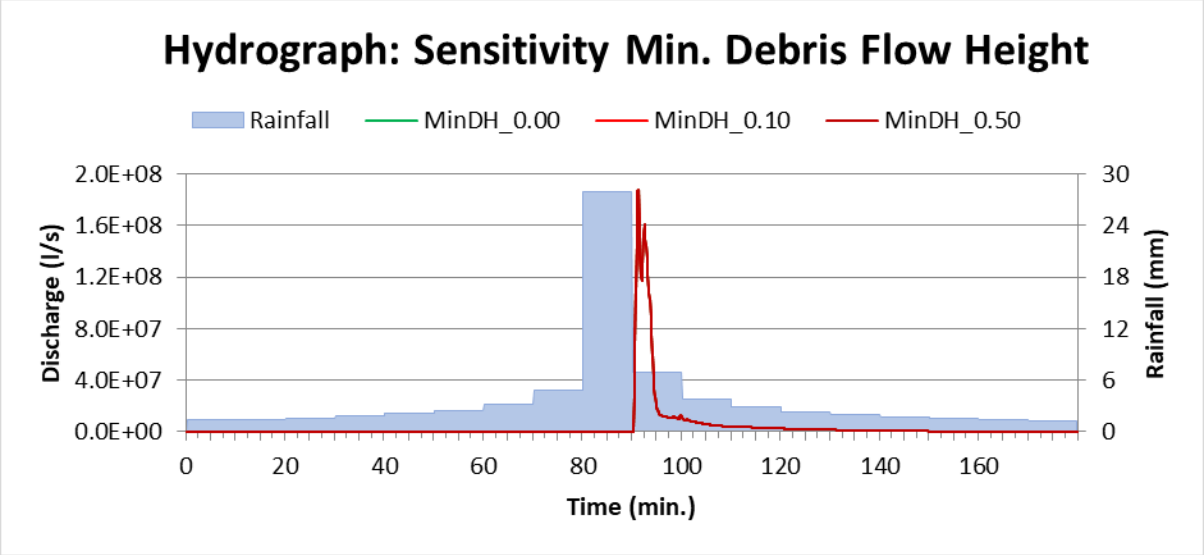

Figure F.4: Hydrograph of the sensitivity analysis with the minimum debris flow height. Changed to a value of 0.00-0.50.

References

Alcántara-Ayala, I. (2002). Geomorphology, natural hazards, vulnerability and prevention of natural disasters in developing countries. *Geomorphology*, *47*(2), 107-124.

Aleotti, P. and Chowdhury, R. (1999). Landslide hazard assessment: summary review and new perspectives. *Bulletin of Engineering Geology and the environment*, *58*(1), 21-44.

Allemand, P., Delacourt, C., Lajeunesse, E., Devauchelle, O. and Beauducel, F. (2014). Erosive effects of the storm Helena (1963) on Basse Terre Island (Guadeloupe—Lesser Antilles Arc). *Geomorphology*, *206*, 79-86.

Anderson, M. G., Holcombe, E., Esquivel, M., Toro, J. and Ghesquiere, F. (2010). The efficacy of a programme of landslide risk reduction in areas of unplanned housing in the Eastern Caribbean. *Environmental management*, *45*(4), 807-821.

Aston, A. R. (1979). Rainfall interception by eight small trees. *Journal of hydrology*, *42*(3-4), 383-396.

Augustinus, P. G., Mees, R. P. R. and Prins, M. (1985). Biotic and abiotic components of the landscapes of Saba, Netherlands Antilles.

Bates, R.L. and Jackson, J.A. (1987). *Glossary of Geology*. Falls Church, Virginia: American Geological Institute.

Baum, R. L., Savage, W. Z. and Godt, J. W. (2008). *TRIGRS – A FORTRAN program for transient rainfall infiltration and grid-based regional slope stability analysis, version 2.0*. US Geological Survey Open File Report 2008-1159, 75 pp.

Beguería, S. (2006). Validation and evaluation of predictive models in hazard assessment and risk management. *Natural Hazards*, *37*(3), 315-329.

Bender, S. (1991). *Primer on natural hazard management in integrated regional development planning*. Washington, DC: Organization of American States.

Blanc, J., Hall, J. W., Roche, N., Dawson, R. J., Cesses, Y., Burton, A. and Kilsby, C. G. (2012). Enhanced efficiency of pluvial flood risk estimation in urban areas using spatial–temporal rainfall simulations. *Journal of Flood Risk Management*, *5*(2), 143-152.

Boegh, E., Soegaard, H., Broge, N., Hasager, C. B., Jensen, N. O., Schelde, K. and Thomsen, A. (2002). Airborne multispectral data for quantifying leaf area index, nitrogen concentration, and photosynthetic efficiency in agriculture. *Remote sensing of Environment*, *81*(2), 179-193.

Bogaard, T. A. and Greco, R. (2016). Landslide hydrology: from hydrology to pore pressure. *Wiley Interdisciplinary Reviews: Water*, *3*(3), 439-459.

Bonnin, G. M., Martin, D., Lin, B., Parzybok, T., Yekta, M. and Riley, D. (2008). *NOAA Atlas 14: Precipitation-Frequency Atlas of the United States*. Silver Spring, Maryland: National Oceanic and Atmospheric Administration (NOAA). Volume 3, Version 4.0.

Bryant, E. (2005). *Natural hazards* (2nd ed. ed.). Cambridge: Cambridge University Press.

CBS – Centraal Bureau voor de Statistiek (2017). *Caribisch Nederland; bevolkingsontwikkeling, geboorte, sterfte en migratie.* Retrieved from https://opendata.cbs.nl/

Chen, Y. M., Fan, K. S. and Chen, L. C. (2010). Requirements and functional analysis of a multi-hazard disaster-risk analysis system. *Human and Ecological Risk Assessment: An International Journal*, *16*(2), 413-428.

Chow, V.T. (1959). *Open channel hydraulics*. New York: McGraw-Hill Book Company, Inc.

Chowdhury, R. N. (1984). Recent developments in landslide studies: probabilistic methods-state-of-art-report. In *Proceedings of the 4th International Symposium on Landslides* (pp. 209-228).

CRED – Centre for Research on the Epidemiology of Disasters (2017). *EM-DAT, The International Disasters Database*. Retrieved 7 April 2017 from EM-DAT http://emdat.be

Cruden, D. M. (1991). A simple definition of a landslide. *Bulletin of Engineering Geology and the Environment*, *43*(1), 27-29.

Cruden, D. M. and Varnes, D. J. (1996). Landslides investigation and mitigation, transportation research board. Landslide types and process, *National Research Council*, *National Academy Press*, *Special Report*, 247, 36-75.

Dai, F. C., Lee, C. F. and Ngai, Y. Y. (2002). Landslide risk assessment and management: an overview. *Engineering geology*, *64*(1), 65-87.

De Freitas, J. A., Rojer, A. C., Nijhof, B. S. J. and Debrot, A. O. (2012). *A landscape ecological vegetation map of Sint Eustatius (Lesser Antilles)*. (No. C053/12). IMARES.

De Jong, S. M. and Jetten, V. G. (2007). Estimating spatial patterns of rainfall interception from remotely sensed vegetation indices and spectral mixture analysis. *International Journal of Geographical Information Science*, *21*(5), 529-545.

De Palm, J. (1985). *Encyclopedie van de Nederlandse Antillen*. Zutphen: De Walburg Pers.

De Roo, A. P. J., Wesseling, C. G., Cremers, N. H. D. T., Offermans, R. J. E., Ritsema, C. J. and Van Oostindie, K. (1994). LISEM: a new physically-based hydrological and soil erosion model in a GIS-environment, theory and implementation. *IAHS Publications-Series of Proceedings and Reports-Intern Ass. Hydrological Sciences*, *224*, 439-448.

DeGraff, J. V., Bryce, R., Jibson, R. W., Mora, S. and Rogers, C. T. (1989). Landslides: their extent and significance in the Caribbean. *Landslides: Extent and economic significance*, *68*.

Delestre, O., Cordier, S., Darboux, F., Du, M., James, F., Laguerre, C. and Planchon, O. (2014). *FullSWOF: A software for overland flow simulation.* In *Advances in Hydroinformatics* (pp. 221-231). Singapore: Springer.

Dietrich, W. E. and Montgomery, D. R. (1998). *SHALSTAB: a digital terrain model for mapping shallow landslide potential*. NCASI (National Council of the Paper Industry for Air and Stream Improvement), Technical Report, 29 pp.

Di Stefano, C., Ferro, V. and Mirabile, S. (2010). Comparison between grain-size analyses using laser diffraction and sedimentation methods. *Biosystems engineering*, *106*(2), 205-215.

Dikau, R., Brundsen, D., Schrott, L. and Ibsen, M. L. (1997). *Landslide recognition*. Chichester: Wiley.

Dingman, S. (2015). *Physical hydrology*. Long Grove, Illinois: Waveland Press, Inc.

Duncan, J. M., Wright, S. G. and Brandon, T. L. (2014). *Soil strength and slope stability*. John Wiley & Sons.

Eshel, G., Levy, G. J., Mingelgrin, U. and Singer, M. J. (2004). Critical evaluation of the use of laser diffraction for particle-size distribution analysis. *Soil Science Society of America Journal*, *68*(3), 736-743.

Gee, G. W. and Bauder, J. W. (1986). *Particle-size analysis*. Madison, WI: American Society of Agronomy.

Gijsman, A. J., Jagtap, S. S. and Jones, J. W. (2002). Wading through a swamp of complete confusion: how to choose a method for estimating soil water retention parameters for crop models. *European Journal of Agronomy*, *18*(1-2), 77-106.

Gill, J. C. and Malamud, B. D. (2016). Hazard interactions and interaction networks (cascades) within multi-hazard methodologies. *Earth System Dynamics*, *7*(3), 659.

Green, W. H. and Ampt, G. A. (1911). Studies on Soil Phyics. *The Journal of Agricultural Science*, *4*(1), 1-24.

Guha-Sapir, D., Hoyois, P., Wallemacq, P. and Below., R. (2017). *Annual Disaster Statistical Review 2016: The Numbers and Trends*. Brussels: CRED.

Guzzetti, F., Carrara, A., Cardinali, M. and Reichenbach, P. (1999). Landslide hazard evaluation: a review of current techniques and their application in a multi-scale study, Central Italy. *Geomorphology*, *31*(1), 181-216.

Heinrich, P., Boudon, G., Komorowski, J. C., Sparks, R. S. J., Herd, R. and Voight, B. (2001). Numerical simulation of the December 1997 debris avalanche in Montserrat, Lesser Antilles. *Geophysical Research Letters*, *28*(13), 2529-2532.

Ho, D. Y. and Fredlund, D. G. (1982). Increase in strength due to suction for two Hong Kong soils. In *Proceedings of the Conference on Engineering and Construction in Tropical and Residual Soils, Honolulu* (pp. 263-295).

Huete, A. R. (1988). A soil-adjusted vegetation index (SAVI). *Remote sensing of environment*, *25*(3), 295-309.

Huete, A., Didan, K., Miura, T., Rodriguez, E. P., Gao, X. and Ferreira, L. G. (2002). Overview of the radiometric and biophysical performance of the MODIS vegetation indices. *Remote sensing of environment*, *83*(1), 195-213.

Hungr, O., Leroueil, S. and Picarelli, L. (2014). The Varnes classification of landslide types, an update. *Landslides*, *11*(2), 167-194.

Jakob, M. and Hungr, O. (2005). *Debris-flow hazards and related phenomena* (Vol. 739). Berlin: Springer.

Jetten, V. G. and Van den Bout, B. (2018). *LISEM Limburg Soil Erosion Model*. Documentation and User Manual: 2nd draft, *(01-01-2018)*.

Kamphorst, E. C., Jetten, V., Guérif, J., Iversen, B. V., Douglas, J. T. and Paz, A. (2000). Predicting depressional storage from soil surface roughness. *Soil Science Society of America Journal*, *64*(5), 1749-1758.

Kappes, M. S., Keiler, M., Von Elverfeldt, K. and Glade, T. (2012). Challenges of analyzing multi-hazard risk: A review. *Natural Hazards*, *64*(2), 1925-1958.

Karssen, A. J. (1973). *Historical Geomorphological map of St. Eustatius*. [map]. 1:25.000.

Koomen, A., Dorland, G. and Van Malaske, B. (2012). *Soil map of St. Eustatius (GIS) based on historical paper maps, updated from field surveys*.

Kutílek, M. and Nielsen, D. R. (1994). *Soil hydrology: texbook for students of soil science, agriculture, forestry, geoecology, hydrology, geomorphology and other related disciplines*. Catena Verlag.

Leitão, J. P., Boonya-Aroonnet, S., Prodanović, D. and Maksimović, Č. (2009). The influence of digital elevation model resolution on overland flow networks for modelling urban pluvial flooding. *Water Science and Technology*, *60*(12), 3137-3149.

MacRae, D. R. and Esteban, N. (2007). *St Eustatius Marine Park Management Plan*. Coastal Zone Management (UK) and St Eustatius National Parks Foundation (STENAPA).

Maksimović, Č., Prodanović, D., Boonya-Aroonnet, S., Leitão, J. P., Djordjević, S. and Allitt, R. (2009). Overland flow and pathway analysis for modelling of urban pluvial flooding. *Journal of Hydraulic Research*, *47*(4), 512-523.

Marani, M. and Zanetti, S. (2007). Downscaling rainfall temporal variability. *Water resources research*, *43*(9).

Marzocchi, W., Garcia-Aristizabal, A., Gasparini, P., Mastellone, M. L. and Di Ruocco, A. (2012). Basic principles of multi-risk assessment: a case study in Italy. *Natural Hazards*, *62*(2), 551-573. DOI: 10.1007/s11069-012-0092-x

MDC – Meteorological Department Curaçao (2014). *Hurricanes and Tropical Storms in the Dutch Caribbean*.

MDC – Meteorological Department of Curaçao (2017). *Dataset for station R06TNCE*. Retrieved from http://www.meteo.cw/

Menne, M.J., Durre, I., Korzeniewski, I., McNeal, S., Thomas, K., Yin, Y., Anthony, S., Ray, R., Vose, R.S., Gleason, B.E. and Houston, T.G. (2015). *Global Historical Climatology Network - Daily (GHCN-Daily)*, Version 3.

Merkman, A. (n.d.) *De STUCO waterfabriek op St. Eustatius*. The Daily Herald. Retrieved from https://www.thedailyherald.sx/

Mücher, C. A., Jonker, D., Stuiver, H. J., Kramer, H. and Meesters, H. W. G. (2014). *Production of digital terrain models for the Dutch Caribbean: implication for Saba & St. Eustatius (No. 2569)*. Wageningen UR Alterra.

Nguyen, V. U. and Chowdhury, R. N. (1985). Simulation for risk analysis with correlated variables. *Geotechnique*, *35*(1), 47-58.

OSM – OpenStreetMap contributors (2017). Retrieved from https://planet.openstreetmap.org.

Pack, R. T., Tarboton, D. G., Goodwin, C. N. and Prasad, A. (2005). *SINMAP 2: A Stability Index Approach to Terrain Stability Hazard Mapping, technical description and users guide for version 2.0*. Utah State University.

Pardeshi, S. D., Autade, S. E. and Pardeshi, S. S. (2013). *Landslide hazard assessment: recent trends and techniques*. *SpringerPlus*, *2*(1), 523.

Prokop, A. and Panholzer, H. (2009). Assessing the capability of terrestrial laser scanning for monitoring slow moving landslides. *Natural Hazards and Earth System Sciences*, *9*(6), 1921-1928.

Pudasaini, S. P. (2012). A general two-phase debris flow model. *Journal of Geophysical Research: Earth Surface*, *117*(F3).

Reid, M. E., Christian, S. B., Brien, D. L. and Henderson, S. T. (2015). *Scoops3D: software to analyze 3D slope stability throughout a digital landscape*. U.S. Geological Survey Techniques and Methods, book 14, chap. A1, 218 pp. https://doi.org/10.3133/tm14A1

Rijkers, R. and Hack, R. (2000). Geomechanical Analysis Of Volcanic Rock On The Island Of Saba (Netherlands Antilles). In: Littletidd, J.W., Drinan, J., Bucher, L.R., Hill, H.Z., Parker, T.S., Quincey, R.V. (Eds). GeoEng 2000: International Conference On Geotechnical and Geological Engineering, Melbourne, Australia, 19-24 November 2000. Lancaster: Taylor & Francis/Technomic Publishing Co.

Roobol, M. J. and Smith, A. L. (2004). *Volcanology of Saba and St. Eustatius, Northern Lesser Antilles*. Royal Netherlands Academy of Arts and Sciences, Amsterdam.

Ruiz-Villanueva, V., Allen, S., Arora, M., Goel, N. K. and Stoffel, M. (2017). Recent catastrophic landslide lake outburst floods in the Himalayan mountain range. *Progress in Physical Geography*, *41*(1), 3-28.

Salciarini, D., Godt, J. W., Savage, W. Z., Conversini, P., Baum, R. L. and Michael, J. A. (2006). Modeling regional initiation of rainfall-induced shallow landslides in the eastern Umbria Region of central Italy. *Landslides*, *3*(3), 181.

Saulnier, G. M., Beven, K. and Obled, C. (1997). Including spatially variable effective soil depths in TOPMODEL. *Journal of hydrology*, *202*(1), 158-172.

Saxton, K. E., Rawls, W., Romberger, J. S. and Papendick, R. I. (1986). Estimating generalized soil-water characteristics from texture 1. *Soil Science Society of America Journal*, *50*(4), 1031-1036.

Saxton, K. E. and Rawls, W. J. (2006). Soil water characteristic estimates by texture and organic matter for hydrologic solutions. *Soil science society of America Journal*, *70*(5), 1569-1578.

Schilirò, L., Esposito, C. and Mugnozza, G. S. (2015). Evaluation of shallow landslide-triggering scenarios through a physically based approach: an example of application in the southern Messina area (northeastern Sicily, Italy). *Natural Hazards & Earth System Sciences*, *15*(9).

Smith, K. (2001). *Environmental hazards: assessing risk and reducing disaster*. Routledge.

Smith, S. R., Mücher, C. A., Debrot, A. O., Roupioz, L. F. S., Meesters, H. W. G., Hazeu, G. W., and Davaasuren, N. (2013). *Use of satellite data for the monitoring of species on Saba and St. Eustatius* (No. C124/13). IMARES.

Soeters, R. and Van Westen, C. J. (1996). Chapter 8-Slope instability recognition, analysis, and zonation. In Landslides: Investigation and mitigation. *Transportation research board special report*, (247).

STENAPA – St. Eustatius National Parks (2018). Retrieved from http://www.statiapark.org/

Stoltman, J. P., Lidstone, J. and Dechano, L. M. (Eds.). (2007). *International perspectives on natural disasters: Occurrence, mitigation, and consequences*. Dordrecht: Springer.

Takahashi, T. (2014). *Debris flow: mechanics, prediction and countermeasures*. CRC press.

Teng, J., Jakeman, A. J., Vaze, J., Croke, B. F., Dutta, D. and Kim, S. (2017). Flood inundation modelling: A review of methods, recent advances and uncertainty analysis. *Environmental Modelling & Software*, *90*, 201-216.

Tesfa, T. K., Tarboton, D. G., Chandler, D. G. and McNamara, J. P. (2009). Modeling soil depth from topographic and land cover attributes. *Water Resources Research*, *45*(10).

The Daily Herald (2017a, May 11). Heavy rains cause flooding on Statia. Retrieved from https://www.thedailyherald.sx/

The Daily Herald (2017b, September 8). St. Eustatius cleans up after passing of Irma. Retrieved from https://www.thedailyherald.sx/

Van Beek, L. P. H. (2002). *Assessment of the Influence of Changes in Landuse and Climate on Landslide Activity in a Mediterranean Environment*. PhD Thesis, Utrecht University, Utrecht, 363 pp.

Van den Bout, B., Lombardo, L., Van Westen, C. J. and Jetten, V. G. (2017). Intergration of two-phase solid fluid equations in a catchment model for flashfloods, debris flows and shallow slope failures. Manuscript in preparation.

Van Dijk, E., Van der Meulen, J., Kluck, J. and Straatman, J. H. M. (2014). Comparing modelling techniques for analysing urban pluvial flooding. *Water science and technology*, *69*(2), 305.

Van Westen, C. J. (2000). The modelling of landslide hazards using GIS. *Surveys in Geophysics*, *21*(2-3), 241-255.

Van Westen, C. J., Van Asch, T. W. and Soeters, R. (2006). Landslide hazard and risk zonation—why is it still so difficult?. *Bulletin of Engineering geology and the Environment*, *65*(2), 167-184.

Van Westen, C. J., Castellanos, E. and Kuriakose, S. L. (2008). Spatial data for landslide susceptibility, hazard, and vulnerability assessment: an overview. *Engineering geology*, *102*(3-4), 112-131.

Varnes, D. J. (1978). Slope movement types and processes. *Special report*, *176*, 11-33.

Von Hoyningen-Huene, J. (1981). *Die Interzeption des Niederschlags in landwirtschaftlichen Pflanzenbeständen*. Arbeitsbericht Deutscher Verband für Wasserwirtschaft und Kulturbau, DVWK.

Weerasinghe, K. M., Gehrels, H., Arambepola, N. M. S. I., Vajja, H. P., Herath, J. M. K. and Atapattu, K. B. (2018). Qualitative Flood Risk assessment for the Western Province of Sri Lanka. *Procedia engineering*, *212*, 503-510.

Westerink, J. (2017). Een week na Irma: de gebeurtenissen op Sint-Maarten tot nu toe. *NOS*. Retrieved from https://nos.nl/

Westermann, J. H. (1956). De geologische geschiedenis der drie bovenwindse eilanden St. Martin, Saba en St. Eustatius. *De West-Indische Gids*, 127-168.

Worldview-2. (2014). *DigitalGlobe*, Acquisition date: 08-24-2014.

Zimbone, S. M., Vickers, A., Morgan, R. P. C. and Vella, P. (1996). Field investigations of different techniques for measuring surface soil shear strength. *Soil Technology*, *9*(1-2), 101-111.